HETG Ground Calibration: Preliminary Results

HETG Science Team
Prof. C. Canizares
Instrument Principal Investigator

and the
AXAF Science Center

Version 1.0

September 30, 1997

MIT Center for Space Research
70 Vassar St.
Building 37
Cambridge, MA 02139–4307
USA

Contents

Preface **xiii**

1 Introduction **1**

1.1 The HETG on AXAF 1

1.2 The HETG Itself 2

1.3 HETGS Calibration Definition and Goals 3

1.3.1 Effective Area and Efficiency Definitions 3

1.3.2 Effective Area Calibration Goals 5

1.3.3 LRF Definition 7

1.3.4 LRF Calibration Goals 8

1.4 Ground Calibration Overview 8

1.5 HETG Documentation 9

I Physics, Models, and Laboratory Measurements **11**

2 LRF Physics and Model **13**

2.1 Rowland Geometry and Astigmatism 13

2.2 LRF Approximation: Resolving Power Error Budget 16

2.2.1 HRMA PSF 19

2.2.2 Rowland Astigmatism 21

2.2.3 Grating Period and Roll Variations 21

2.2.4 Aspect and Dither Blurs 21

2.2.5 Detector Blur 22

2.3 Ray-trace Model: **MARX** 23

3 Efficiency Physics and Model 25

3.1 Diffraction Theory and Models 25

3.1.1 Scalar Diffraction Theory 25

3.1.2 Rectangular Models 26

3.1.3 Vertex Model 27

3.1.4 Tilted Grating Model 28

3.1.5 Trapezoidal Model 28

3.2 Synchrotron Measurements 30

3.2.1 Synchrotron Measurements Summary 30

3.2.2 Synchrotron Data Analysis Techniques 30

3.2.3 Gold Optical Constants and Edge Structure 30

3.2.4 Polyimide Optical Constants and Edge Structure 34

3.2.5 Reference Grating Measurements 37

3.2.6 Error Estimates for X-GEF Predictions of Grating Efficiency 41

3.2.7 Synchrotron Analysis Status 43

3.3 Scattering Model 44

3.3.1 General Scattering Theory 44

3.3.2 Scattering Example: Grating Bar Shifts 46

4 Laboratory Measurements and Predictions 49

4.1 LR Measurements 50

4.1.1 LR Period and Roll Variations 50

4.1.2 LR Calibration using NIST Samples 55

4.2 X-GEF Measurements 56

4.2.1 Order Assymmetry and Tilt 61

4.2.2 Laboratory Efficiency Predictions 61

4.3 Alignment Measurements 64

4.4 Long-term: Vacuum Storage Gratings 66

II X-Ray Calibration Facility Measurements and Analysis 67

5 XRCF and the HETG 69

5.1 XRCF Introduction 69

5.1.1 XSS 70

5.1.2 BNDs 70

5.1.3 HRMA, Gratings, and Shutters 70

5.1.4 HXDS Focal Plane System 71

5.1.4.1 HXDS translations 71

5.1.4.2 HSI in the Focal Plane 71

5.1.5 FPC and SSD in the Focal Plane 71

5.1.6 ACIS-2C 71

5.1.7 ACIS 72

5.1.8 HRC 72

5.2 Differences between XRCF and Flight 73

5.2.1 HETG Location at XRCF 73

5.2.2 HETG Orientation at XRCF 74

5.3 Summary of HETG XRCF Measurements 75

5.3.1 Efficiency Measurements 75

5.3.2 LRF Measurements 75

5.4 Examples of XRCF Data 77

5.5 Status of the HETG XRCF Analysis 81

6 XRCF LRF Measurements **83**

6.1 Overview 83

6.2 Periods and Angles 84

6.2.1 Analysis Method 84

6.2.2 Results 84

6.3 LRF Core: Period and Roll Variations 90

6.3.1 Focus tests 90

6.3.2 1D Scans of LRF 90

6.3.3 Results 90

6.4 MEG Mis-Aligned Gratings 94

6.5 Between Core and Scatter 97

6.6 Scatter 98

6.6.1 Phase I HSI Data 98

6.6.2 HETG Scatter Tests with ACIS-2C 99

6.6.2.1 Setup 99

6.6.2.2 Reduction Details 100

6.6.2.3 Analysis Results 103

6.6.3 Interpretation of scattering profile results 106

6.7 Offaxis and Defocus Tests 107

6.8 ACIS-S Rowland Conformance 108

7 XRCF Efficiency and Effective Area Measurements **109**

7.1 Overview 109

7.2 Alignment Tests 110

7.3 XRCF Source Characteristics 112

7.3.1 Source Spectra and Efficiency Measurements 112

7.3.2 Beam Uniformity Effects on Efficiency Measurements 112

7.4 Efficiency: Phase 1, Fixed Energies . . . 113
7.4.1 System Effective Area . . . 113
7.4.2 Optic Effective Area . . . 114
7.4.3 Optic Effective Area Results . . . 114
7.4.4 Grating Efficiency . . . 118
7.4.5 Grating Efficiency Results . . . 118
7.4.6 Effective Area / Efficiency Analysis Software . . . 118
7.5 Efficiency: ACIS-2C Data . . . 121
7.6 Efficiency: Phase 1, Monochromator Scans . . . 122
7.7 Efficiency: Phase 2, Order Ratios . . . 123
7.7.1 DCM-HETG-HRC-I Efficiency Ratio . . . 123
7.8 Relative Effective Area: Molecular Contamination . . . 125
7.8.1 HETGS Molecular Contamination Result . . . 125
7.9 Effective Area with ACIS-S . . . 132
7.10 Effective Area with HRC-I . . . 133

III Calibration Data and Products 135

8 Calibration Data 137

8.1 Synchrotron Data . . . 137
8.2 HETG Facet Data . . . 137
8.3 LR Data . . . 137
8.4 X-GEF Data . . . 137
8.5 HESS Design and Metrology Data . . . 137
8.6 Alignment Data . . . 137
8.7 XRCF Data . . . 137

9 Calibration Products 139

9.1 Overview of Products 139

9.2 Fundamental Calibration Products for HETG 141

9.3 HETG Calibration Interface Products 142

9.3.1 Basic Parameters 142

9.3.2 Periods, Angles, and Spacing 144

9.3.3 Period and Roll Variation Parameters 145

9.3.4 Efficiency Products 146

9.3.5 **MARX** Parameters 149

9.3.5.1 **MARX** HETG LRF Parameters 149

9.3.5.2 **MARX** Rectangular Efficiency Parameters 150

9.3.5.3 **MARX** Efficiency Files 153

9.4 HETGS Calibration Interface Products 154

9.4.1 Resolving Power 154

9.4.2 Effective Area 154

9.4.3 XSPEC Response Matrices 155

Acronyms **157**

Mathematical Symbols **159**

Bibliography **161**

List of Figures

1.1 Schematic of the HETGS Configuration 2

1.2 Cross-section schematic of the HETG gratings 3

1.3 HETG drawing with facet IDs 4

1.4 PSF and LRF Example 6

2.1 Rowland torus ray geometry 14

2.2 HETGS Resolving Power vs. Energy Curves 17

2.3 Fitting the **MARX** MEG HRMA Effective Blur 20

2.4 Fitting the **MARX** HEG HRMA Effective Blur 20

3.1 Asymetry parameter for a trapezoidal grating 29

3.2 Trapezoidal bar shape 29

3.3 Comparison of synchrotron-derived optical constants to Henke tables. 31

3.4 First order synchrotron data of HEG grating HA2021, with best fit model. 32

3.5 Residuals from the first order fit of grating HA2021. 32

3.6 First order synchrotron data of MEG grating MA1047, with best fit model. . . . 33

3.7 Residuals from the first order fit of grating MA1047. 33

3.8 Data and best-fit model for HEG grating over full energy range 35

3.9 Residuals for HEG grating over full energy range 35

3.10 Data and best-fit model of HEG grating at polyimide edges 36

3.11 Residuals for HEG grating at polyimide edges 36

3.12 Data and best-fit model of reference grating HX220 38

3.13 Residuals for reference grating HX220 38

3.14 Data and best-fit model of reference grating MX078 39

3.15 Residuals for reference grating MX078 39

3.16 Tilt data for reference grating MX078 40

3.17 Tilt data for reference grating HX220 40
3.18 Residuals between first order X-GEF predictions and synchroton data 41
3.19 Residuals between 0th order X-GEF predictions and synchroton data 42

4.1 LR Period Contour Plot 51
4.2 Period-dp/p scatter plot for the HETG flight gratings 52
4.3 Period Histogram of the MEG Flight Gratings 53
4.4 Period Histogram of the HEG Flight Gratings 54
4.5 X-GEF Schematic 56
4.6 X-GEF Example Measurements and Derived Model: MEG 58
4.7 X-GEF Example Measurements and Derived Model: HEG 59
4.8 X-GEF Vertex Model Example: MEG 60
4.9 X-GEF Vertex Model Example: HEG 60
4.10 X-GEF Tilt Plots for an MEG 62
4.11 X-GEF Tilt Plots for an HEG 63
4.12 Measured roll errors for the 336 flight gratings 65

5.1 XRCF hardware schematic 70
5.2 HSI image of 3rd-order MEG Al-K line 78
5.3 Example Phase 1 PHA spectra 79
5.4 ACIS-2C defocussed image of Al-K line 80
5.5 ACIS-S defocussed image of Al-K line 80

6.1 Beam center example plot 85
6.2 Period and angle analysis output 86
6.3 Beam center results file 87
6.4 Measured Grating Periods 88
6.5 Measured Dispersion Angles 89

6.6 FPC 1D slit scans: HEG, Mg-K, first and second orders 91

6.7 FPC 1D slit scans: MEG, Mg-K, first and third orders 91

6.8 XRCF E/dE Measurements 93

6.9 Mis-aligned MEGs: HSI defocused image 94

6.10 Shell 3 sector FF Events 96

6.11 HSI cusp HEG scatter at 1.775 keV 98

6.12 ACIS-2C image showing HEG scatter at 1.775 keV. 100

6.13 Pulse Height Distribution for '2C HEG Scatter Data 101

6.14 Exposure time "map"for the '2C HEG scattering tests. 102

6.15 Fitting Gaussians to the HEG scattered light cross-dispersion profiles. 104

6.16 Estimated "Background" and the Count Spectra in the Source Region 105

6.17 Net Scattered Light After Dividing by the Exposure Time "Map" 105

6.18 Normalized HEG Response to a Monochromatic Light Source at 1.775 keV . . . 106

7.1 "Alignment" test results, shells 1 and 6 111

7.2 Preliminary XRCF HRMA-MEG and HRMA-HEG Areas: 1st order 116

7.3 Preliminary XRCF HRMA-MEG and HRMA-HEG Areas: 0-order 117

7.4 Preliminary XRCF MEG and HEG Efficiencies: 1st order 119

7.5 Preliminary XRCF MEG and HEG Efficiencies: 0 order 120

7.6 DCM-HETG-HRC-I 1st to 0 order ratio vs. E 124

7.7 Molecular contamination spectrum with HEG-ACIS-S 126

7.8 Molecular contamination spectrum, HEG-ACIS-S, 1-1.4 keV 127

7.9 Molecular contamination spectrum, HEG-ACIS-S, 1.4-2 keV 128

7.10 Molecular contamination spectrum, HEG-ACIS-S, 2-3 keV 129

7.11 Molecular contamination spectrum, HEG-ACIS-S, 3-5 keV 130

7.12 Molecular contamination spectrum, HEG-ACIS-S, 5-10 keV 131

9.1 Schematic Diagram of the Types of Calibration Products 140

9.2 Basic Geometry for HETG Facet Location 142

9.3 Effective Efficiency for First-order MEG and HEG 147

9.4 Effective Efficiency for HETG 1st and 0 orders 148

9.5 Comparing MEG Rectangular and CIP Efficiencies (orders 1, 0). 151

9.6 Comparing MEG Rectangular and CIP Efficiencies (orders 2, 3). 151

9.7 Comparing HEG Rectangular and CIP Efficiencies (orders 1, 0). 152

9.8 Comparing HEG Rectangular and CIP Efficiencies (orders 2, 3). 152

List of Tables

1.1 HETG Documentation 9

2.1 Simplified Resolving Power Error Budget Equations 18

3.1 Summary of HETG synchrotron radiation tests 30

4.1 HETG laboratory setups and the parameters measured 49

4.2 NIST samples for LR calibration 55

4.3 Correction of the LR Period Measurements 55

5.1 XRCF Documents and References 69

5.2 XRCF Phases and Detectors 69

5.3 Table of useful XRCF HETG parameters 71

5.4 Summary of HETG XRCF Measurements in Phase I 76

5.5 Summary of HETG XRCF Measurements in Phase II 76

5.6 Status Code 81

5.7 Status of HETG XRCF analyses 81

6.1 Beam Center Measurements of Diffracted Order Locations 84

6.2 Results of some XRCF LRF core measurements 92

6.3 Mis-aligned MEGs 95

9.1 Basic HETG Design Parameters 143

9.2 HETG Period, Angle, and Spacing Parameters 144

9.3 Parameters Effecting the HETG LRF Core 145

9.4 CIP Efficiency Files for the HETG 146

9.5 Flight HETG LRF parameters for **MARX**. 149

9.6 **MARX** Parameters for Rectangular approximation to HETG efficiency. 150

9.7 **MARX** Parameters for Table-lookup HETG Efficiencies 153

Preface

This document is a preliminary version of the HETG Ground Calibration Report. The purpose of this preliminary release is to document the status of the HETG performance and calibration based on an initial sampling of XRCF data. For this reason many sections and analyses are neccessarily incomplete, see Table 5.7.

The preliminary results reported here demonstrate that the HETG is performing largely as designed and expected, *e.g.*, see Figures 6.8, 7.4, and 7.5. This is a significant conclusion that could only come from the full system (HRMA-HETG-ACIS-S) testing carried out at XRCF.

The XRCF testing also proved valuable in identifying two minor effects, due to fabrication non-idealities, that were not predicted and would have been confusing to impossible to diagnose in flight; these are the MEG misaligned gratings (Section 6.4) and the HEG scattering (Section 6.6). Finally, there remains a small ("5mm") discrepancy between the XRCF data and the relative periods and locations of the HETG and LETG (Section 6.2).

The information and results presented here are the work of both the HETG Science Team and the ASC.

A next revision is planned for February 1, 1998 (to support the ASC's April release of the "Calibration Data Guide") and a complete report will be issued June 1, 1998. Please address comments and corrections to the Editor, `dd@space.mit.edu`.

- Dan Dewey, September 30, 1997

These analyses are in process; further up-to-date "notebook"-style information is available at:

`http://space.mit.edu/HETG/xrcf.html` .

Section 1

Introduction

This document details the ground calibration of the HETG, including the basic models, subassembly ("laboratory") data, XRCF measurements, and the resulting calibration products. This section provides an overview of the HETG and its calibration.

Part I of this document presents the basic operating principles and models of the HETG (Sections 2 and 3) and the laboratory measurements made on the component facets of the flight HETG (section 4.)

Part II consists of an introduction to the XRCF calibration activities (Section 5) followed by XRCF analyses broken down into a set of projects (Sections 6.2 through 7.10). The status of these analysis efforts is given in Table 5.7.

Lastly, in Part III the complete set of ground calibration results are sythesized to produce "Calibration Products" for use in flight analysis software. Methods of accessing the calibration data are described in Section 8. The current best estimates of the parameters describing the HETG and HETGS are available in Section 9.

1.1 The HETG on AXAF

The High Energy Transmission Grating (HETG) is one of four Scientific Instruments (SIs) that will operate with the High Resolution Mirror Assembly (HRMA) in NASA's Advanced X-ray Astrophysics Facility (AXAF). Two of the AXAF SIs are imaging detectors at the HRMA focal plane: the AXAF CCD Imaging Spectrometer (ACIS) and the High Resolution Camera (HRC). These detectors each consist of two sub-imagers: an "-I" imager (ACIS-I, HRC-I) of large area and square aspect ratio for imaging applications and an "-S" imager (ACIS-S, HRC-S) with a more rectangular aspect ratio designed for grating readout.

Either of the two grating SIs, HETG or LETG[8, 40], can be inserted into the optical path just behind the HRMA and, through diffraction, deflect the converging rays by angles roughly proportional to their wavelength, Figure 1.1. By combining the HRMA's high angular resolution (of order 1 arc second) and the grating's large diffraction angles (as high as 100 arc seconds/Å), the HRMA-grating-detector systems are capable of spectral resolving powers up to $E/dE \approx 1000$

in the AXAF energy band.

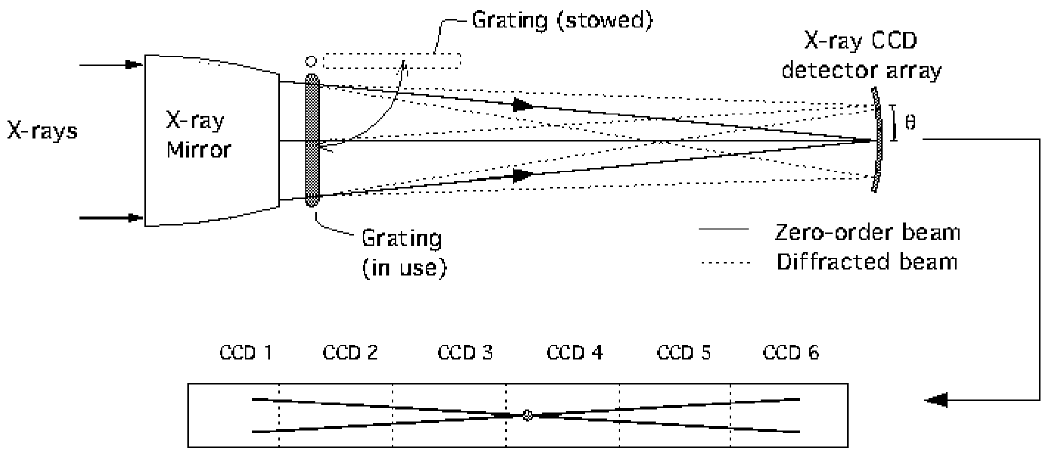

Figure 1.1: Schematic of the HETGS Configuration. The HETG can be inserted into the optical path behind the AXAF mirror (HRMA) to intercept and diffract the converging X-rays. The X-rays are diffracted by an angle β given in Equation 1.1 and are detected by the six chips of the ACIS-S CCD array. The HEG and MEG gratings have their dispersion axes oriented ± 5 degrees to the ACIS-S long axis.

1.2 The HETG Itself

Details of the HETG have been presented previously in SPIE conferences[9, 30]. The HETG is a faceted Rowland torus design[3] that has been engineered to place each facet at its prescribed location and orientation on a Rowland torus with Rowland Diameter of 8634 mm. Specifically, in Figure 1.3 the precision, lightweight HETG Element Support Structure[39] (HESS) is populated with 336 individual grating facets. This design combined with the period and period variation properties of the facets allows high resolving powers.

The 336 grating facets of the flight HETG were fabricated in-house at M.I.T. in the Space Microstructures Laboratory (SML) using state-of-the-art holographic lithography techniques[42] to create a fine period, high aspect ratio grating structures supported on a thin polyimide membranes, Figure 1.2. Each facet was then tested in-house for period and diffraction efficiency characteristics[12].

The four rings of facets on the HETG are designed to intercept and diffract X-rays from the corresponding four HRMA mirror shells. Because most of the high energy area of the HRMA is due to the inner two shells, very fine period (2000 Å) "High Energy Grating" (HEG) facets are used here. The outer two shells have "Medium Energy Grating" facets ("MEG", 4000 Å period) that are efficiency-optimized below 2 keV. These two grating sets have their dispersion axes offset by 10 degrees from each other so that their spectra are spatially separated on the detector. In this way the HETG enables high-resolution spectroscopy ($E/dE > 100$) in the 0.4 keV to 9 keV band.

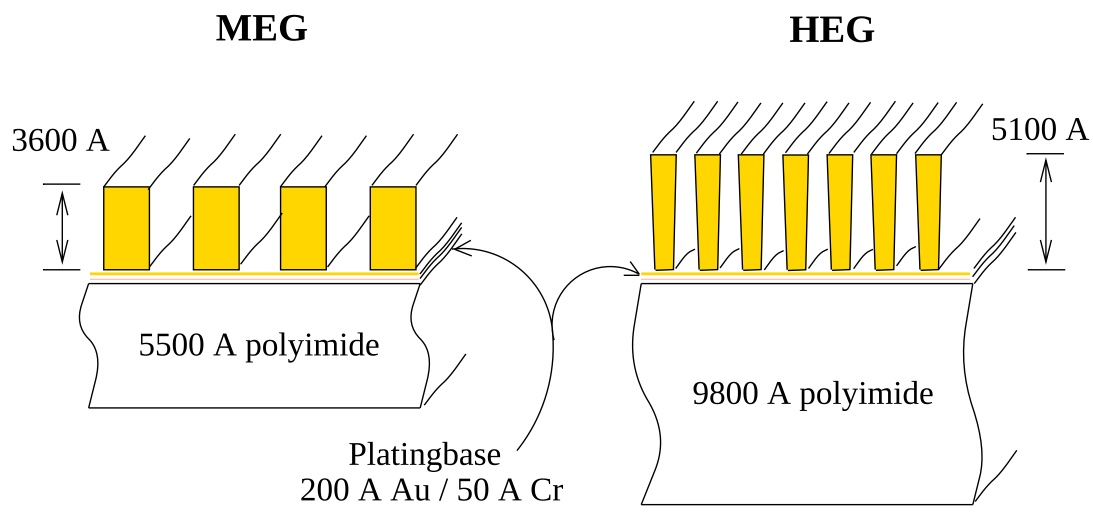

Figure 1.2: Cross-section schematic of the HETG gratings. The fine-period gold grating bars are supported on a polyimide membrane. A uniform "platingbase" layer provides adhesion of the bars to the polyimide.

1.3 HETGS Calibration Definition and Goals

The complete flight instrument that will be utilized and must be calibrated is the combination of the HRMA, HETG, and the ACIS-S—the *HETG Spectrometer (HETGS)*. The HETGS calibration requirements generally fall into two categories: calibration of the *Effective Area* and calibration of the *Line Response Function (LRF)*. Scientific goals set calibration requirements on the HETGS in these areas which are then flowed-down to requirements on the individual HEG and MEG elements themselves.

1.3.1 Effective Area and Efficiency Definitions

The HETGS response to an on-axis monochromatic point source consists of images in the various *diffracted orders* produced at locations given by the grating equation[5]:

$$sin(\beta) = \frac{m\lambda}{p} \tag{1.1}$$

where m is the order of diffraction (an integer $0, \pm1, \pm2, ...$), p is the grating period and β is the dispersion angle. Knowledge of the dispersion axis and the grating-to-detector distance (the Rowland spacing) allows a conversion of the angle β to a physical location on the detector.

These diffracted images are, for the most part, spatially localized and so it is possible and convenient to express the system response to a monochromatic source with incident flux of 1 photon/cm^{2}s as the sum of weighted spatial functions:

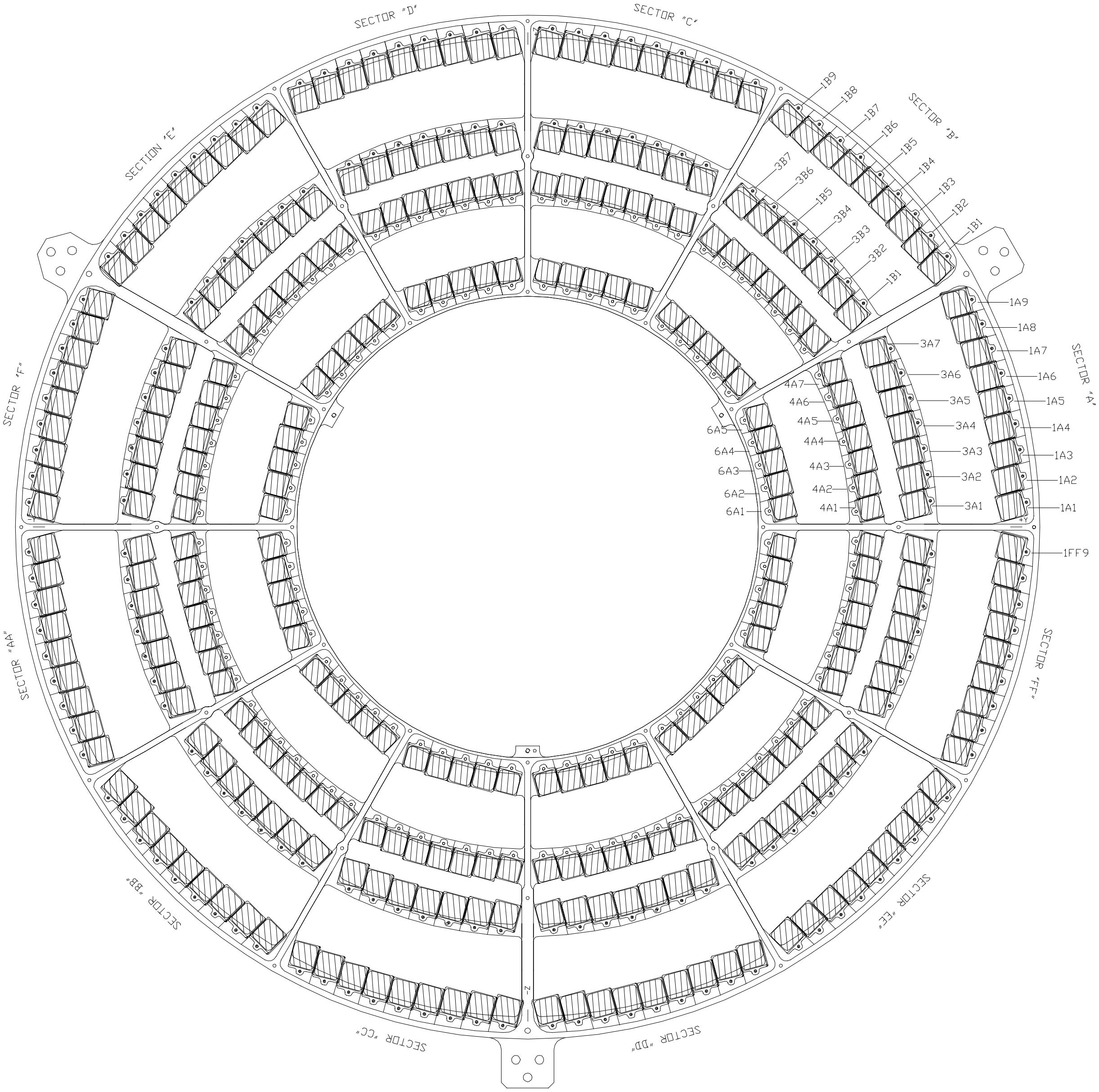

Figure 1.3: The HETG. A lightweight (≈ 10 kg) aluminum structure supports 336 individual grating facets in a Rowland geometry. This view of the HETG is from the HRMA side and the facet-location identification scheme is indicated. The HETG, as installed for ground calibration at XRCF, was rotated 180 degrees about the optical axis from this view.

$$\text{HETGS response}(E,\ldots) = \sum_m SEA(E,m,\ldots) \times PSF(E,m,\ldots) \tag{1.2}$$

where $SEA(E,m,\ldots)$ is the *system effective area*, described further below, and $PSF(E,m,\ldots)$ is a unit-normalized 2-dimensional point spread function which describes the spatial distribution of the m-th order detected events, see Section 1.3.3 below. The dots $(\ldots)$ in the arguments indicate that there are other dependancies, *e.g.*, off-axis angles, defocus, detector modes, etc.

The system effective area for the HETGS, in cm^{2}counts/photon, can be calculated from the following terms:

$$SEA(E,m,\ldots) = \sum_{s=1,3,4,6} A_s(E,\ldots)\ G_s(E,m)\ QE(E,\ldots) \tag{1.3}$$

Here the sum is over the HRMA mirror shells, A_s is the *optic effective area* for HRMA shell s in cm^2, and $QE(E,\ldots)$ is the detector quantum efficiency including effects of detector spatial uniformity (*e.g.*, BI/FI chips, gaps) and detection mode (*e.g.*, event grading) in counts per photon.

$G_s(E,m)$ is the average diffraction efficiency for the gratings on shell s and is calculated from the individual facet efficiencies $g_f(E,m)$:

$$G_s(E,m) = \ \nu_s\ \frac{1}{N_s} \sum_{f \in \{s\}}\ g_f(E,m) \tag{1.4}$$

where N_s is the number of facets on shell s and ν_s is a unitless shell-by-shell vignetting factor to account for the inter-grating gaps. Thus, the physics of $g_f(E,m)$ governs the HETG contribution to the HETGS effective area.

Finally, it is useful to define the grating "effective efficiency" for combinations of more than a single HRMA shell:

$$G_{\text{config}}(E,m) = \frac{\sum_{s \in \{\text{config}\}} A_s(E)\ G_s(E,m)}{\sum_{s \in \{\text{config}\}} A_s(E)} \tag{1.5}$$

where "config" may usefully be the HEG (shells 4,6), MEG (shells 1,3), or HETG (shells 1,3,4,6). In practice, it is the effective efficiencies of these configurations that are measured and used.

1.3.2 Effective Area Calibration Goals

Calibration of the effective area of the HETGS is driven by the desire to extract information about the physical parameters of an emitting region (e.g., temperature, ionization age, elemental abundances) from the observed intensity of spectral lines through plasma diagnostics[11].

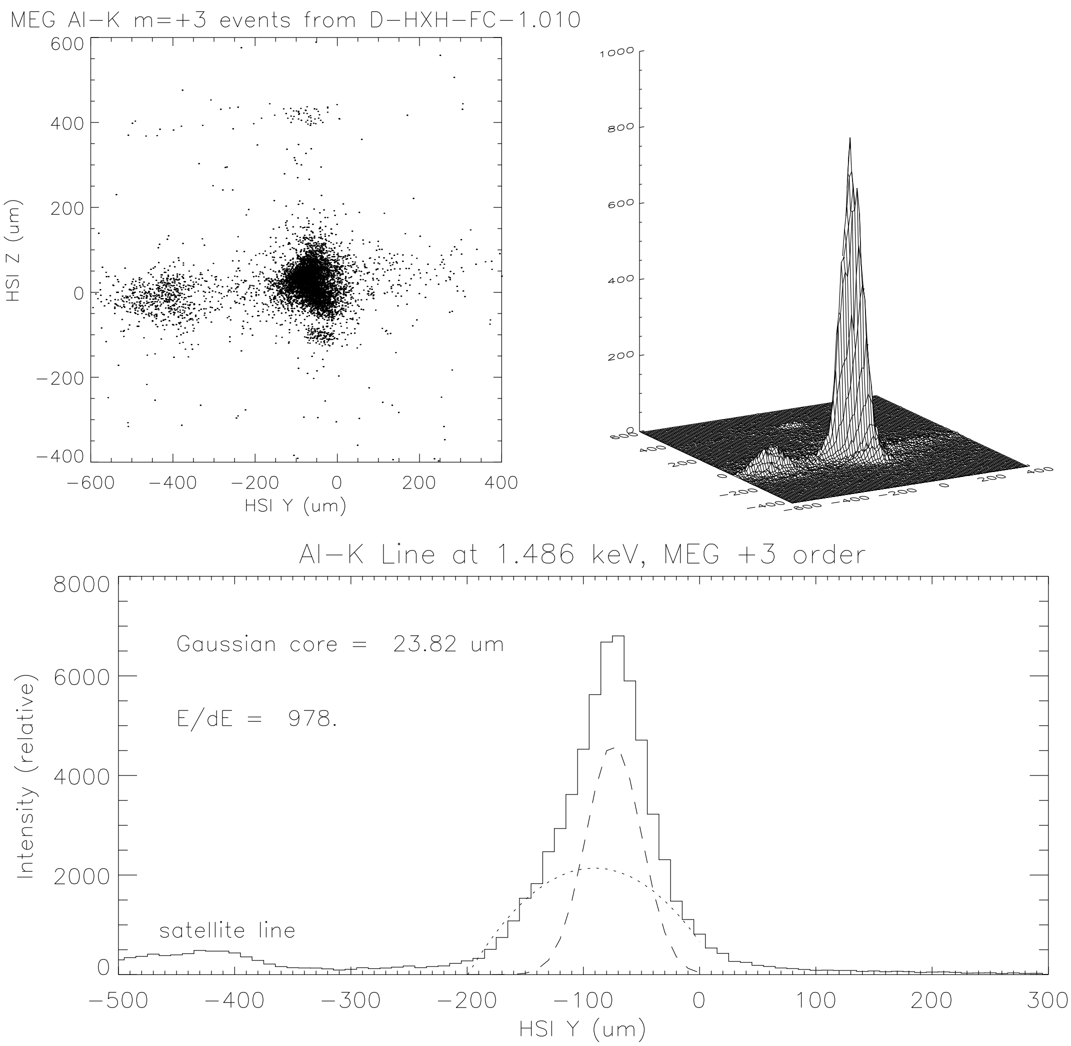

Figure 1.4: PSF and LFR example. The event distribution (top left) may be described by a 2-D point spread function PSF, $\rho(y,z)$ (top right). The resulting 1-D line response function $l(y')$ (lower plot) is shown with a Gaussian plus quadratic fit to its core.

The events are from an XRCF HSI image of the 3rd-order MEG Al-K line; the HSI is centered at $\mathrm{HSI}_Y = 54.76$ mm, $\mathrm{HSI}_Z = 4.496$ mm. Visible in addition to the main peak is the "satellite line" at HSI_Y = -400. PSF outliers at HSI_Z = +400 and -100 represent mis-aligned grating facets.

Analysis of the sensitivity of scientific conclusions on the calibration accuracy has led to the requirements that the HETGS effective area be known with an absolute accuracy of order 10% (1σ) at all energies, and that the relative effective area at two different energies be known to of order 3% (1σ). Note that the effective area needs to be known at least on an energy grid comparable to the coarser of the astrophysical spectrum feature scale and the instrumental response variation scale.

These requirements for HETGS calibration have implications for the calibration of the HRMA and focal plane detectors as well as the HEG/MEG elements. Ideally the effective area and/or efficiency of all components would be know accurately enough so that the composite system would be calibrated to the 3% (1σ) level on an energy scale of $\Delta E \approx E/1000$, especially around instrumental edges.

For our laboratory calibration of the HEG/MEG elements we have set a goal of 1% (1σ). This allocates most of the error to the HRMA and focal plane detector calibrations where the calibration process is inherently more difficult (i.e., measuring an effective area or an absolute detection efficiency as opposed to a transmission efficiency.)

Though not as central as the (first-order) diffraction efficiency measurements, it is important that the zero-order and higher orders be calibrated as well.

1.3.3 LRF Definition

As described above the focal plane image that results from a monochromatic near-axis point source can be considered as a set of images, one for each grating-order. The distribution of each of these images can be described by a *2-dimensional Point Spread Function (PSF)* which gives the normalized density of detected photons in the detector plane:

$$\rho(y,z) \Leftarrow PSF(E, m, \ldots) \tag{1.6}$$

where y, z are the detector coordinates, E, m are the energy and grating-order, and "$\ldots$" is again a placeholder for other dependancies, *e.g.*, the telescope defocus, location of the source with respect to the optical axis, etc. As an example, an X-ray event plot and the corresponding $\rho(y,z)$ PSF is shown in the upper plots of Figure 1.4 (these are data from XRCF and are used here for illustration purposes; they are discussed in Section 6.3.)

Because the spectroscopic information of a grating dispersive instrument is along the dispersion direction, it is useful to define the *one-dimensional Line Response Function (LRF)* to be the PSF integrated over the cross-dispersion direction:

$$l(y') = \int dz' \rho(y', z') \tag{1.7}$$

where the y', z' indicate axes aligned with the dispersion and cross-dispersion directions in the detector plane. The lower plot in Figure 1.4 gives the LRF corresponding to the example PSF. Because of the image properties of the mirror, it is generally useful to (conceptually) break the LRF into at least two regions: a core or inner LRF and the wings or outer portion of the LRF.

The *Resolving Power* of the spectrometer at energy E is defined as

$$R(E,m) \;=\; E/dE \;=\; y'_{\rm centroid}/dy'_{\rm FWHM} \tag{1.8}$$

where dE is the full-width at half-maximum (FWHM) of the LRF. Typically the LRF core can be well fit by a Gaussian profile and in this case $dE \approx 2.35\sigma$ approximates the FWHM.

1.3.4 LRF Calibration Goals

The goal of HETGS LRF calibration is to produce LRF models which are accurate (have low χ^2) when fitting a line containing of order 1000 counts. Additionaly, it is important that any "wings" or "ghosts" in the dispersed spectrum be identified and quantified. Specifically, the contribution of wings at all scales should be known or limited to 1% of the peak line flux in a resolution element.

1.4 Ground Calibration Overview

The HETG ground calibration program consists of 4 main activities:

- Creating and validating models for the HETGS LRF performance, Section 2.
- Synchrotron testing of sample and reference gratings to understand and validate the diffraction model $g_f(E,m)$, Section 3.
- Laboratory testing and assembly of all flight gratings, Section 4.
- XRCF tests of the flight hardware, Part II, Sections 5-7.

1.5 HETG Documentation

It is assumed that the reader is familiar with AXAF, the HETG, and XRCF calibration and has access to the documents below.

Table 1.1: HETG Documentation

Printed documents:		
AXAF Observatory Guide	ASC/User Support	October 1997
AXAF Proposers Guide	ASC/User Support	October 1997
MARX Manual	ASC/SDS	October 1997
HETG Ground Calibration Report	HETG and ASC	October 1997
HETGS Flight Performance and Calibration Report	ASC/Cal	TBD 1997
Electronic documents:		
`http://asc.harvard.edu`	ASC	dynamic
`http://space.mit.edu/HETG/xrcf.html`	HETG	dynamic

Part I

Physics, Models, and Laboratory Measurements

Section 2

LRF Physics and Model

2.1 Rowland Geometry and Astigmatism

The HETG is a faceted Rowland torus design and has been engineered and built to accurately place each facet at its prescribed location and orientation. Although physical-optics analysis of the image produced by this Rowland design can be quite complex[3], the basic features can be understood through simple ray geometry.

In the "Top View" of Figure 2.1 we are looking along the cross-dispersion direction, z'. The diffraction angle is β, Equation 1.1, which through the geometric properties of the circle, causes rays diffracted from gratings located on the Rowland circle to converge at another point on the Rowland circle. The dotted lines represent zero-order ($m = 0, \beta = 0$) rays and the solid lines a diffracted order ($m > 0, \beta > 0$). The bottom panel, "Side View", looks along the dispersion direction, y', at rays from a set of gratings arranged perpendicularly to those above.

Together, these constructions show the astigmatic nature of the spectrally focussed image: the rays come to a focus in the dispersion direction, the *Rowland focus*, at a different location from their focus in the cross-dispersion direction, the *Imaging focus*. The offset to be on the Rowland circle is given by:

$$\Delta X_{\mathrm{Rowland}} = \beta^2 X_{\mathrm{RS}} \tag{2.1}$$

where X_{RS} is the Rowland spacing. In order to maintain the best spectroscopic focus the detector surface must conform to or approximate this Rowland curvature.

At the Rowland focus the image is elongated (blurred) in the cross-dispersion direction by a peak-to-peak value given by similar triangles as:

$$\Delta z' = \frac{2R_0}{X_{\mathrm{RS}}} \Delta X_{\mathrm{Rowland}} \tag{2.2}$$

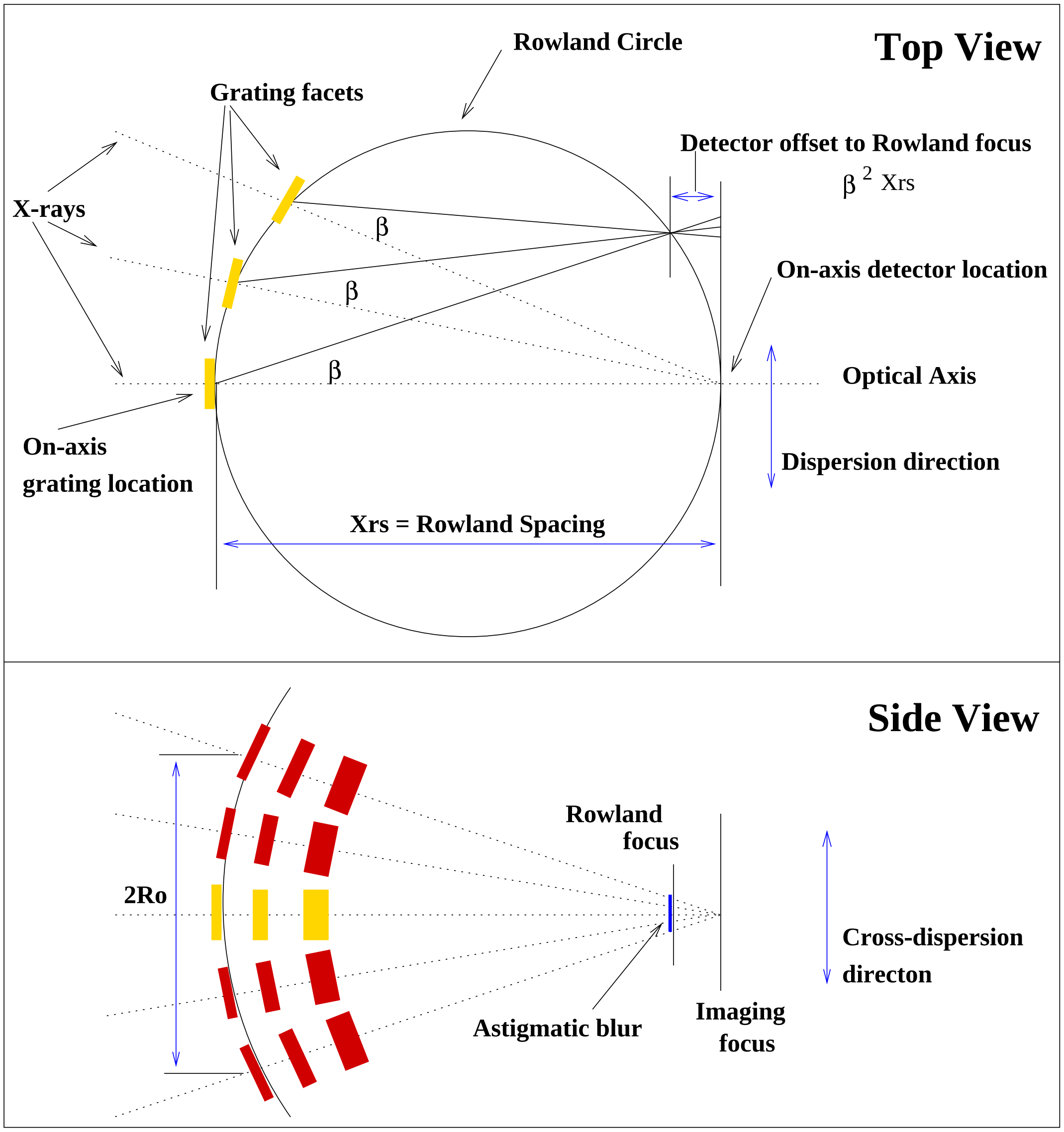

Figure 2.1: Simplified ray geometry for the Rowland torus design. The two views are orthogonal to each other and show the gratings on the surface of a torus. Please see the text for a detailed explanation.

where R_0 is the perpendicular distance of the ring of gratings from the optical axis.

It is important to note that in the ideal case the grating provides primarily a deflection to the rays being focussed by the HRMA. Because of this, the focus quality is not dramatically effected by perturbations of the grating geometry from the ideal Rowland Torus design. In particular, the flight HETG is built to a Rowland diameter of 8633.69 mm, yet at XRCF because of the finite source distance changes to the HRMA focal length and other considerations, the HETG Rowland spacing (on-axis grating to detector distance) was of order 8800 mm. This difference adds an insignificant additional spectral blur (of order 1 μm rms.)

To-do:
Add ray-trace examples of image formation.
Describe and add ray-trace examples of finite facet blur (small).
Add ray-trace of effect of XRCF mis-positioning.
Check as-installed HETG tilts – need to include in error-budget or **MARX** ?

2.2 LRF Approximation: Resolving Power Error Budget

The LRF of the HETGS can be crudely yet usefully characterized by the location and FWHM of the LRF core in both the dispersion and cross-dispersion directions. The "resolving power" of the spectrometer is defined by:

$$\mathrm{ResolvingPower} = \frac{E}{dE_{\mathrm{FWHM}}} = \frac{y'}{dy'_{\mathrm{FWHM}}} \tag{2.3}$$

The design of the HETG involved the use of an error budget to sum the various contributions to the resolving power. This error budget was useful for studying the dependence of the resolving power on the variation of individual error terms. The error budget results were verified by performing simplified ray-traces of single and multiple facets. The dotted curve of Figure 2.2 is based on conservative assumptions and demonstrates the expectation that the HETG would meet its specifications (triangles).

The error budget presented in Table 2.1 includes all of the important error terms for the flight HETGS resolving power; a resulting range of "realistic" curves for the flight HETGS resolving power is plotted as the solid and dashed curves in Figure 2.2.

The error budget terms, their equations, and the current flight value estimates are discussed in the sections below.

To-do:
Describe the "error budget ray-trace" software.

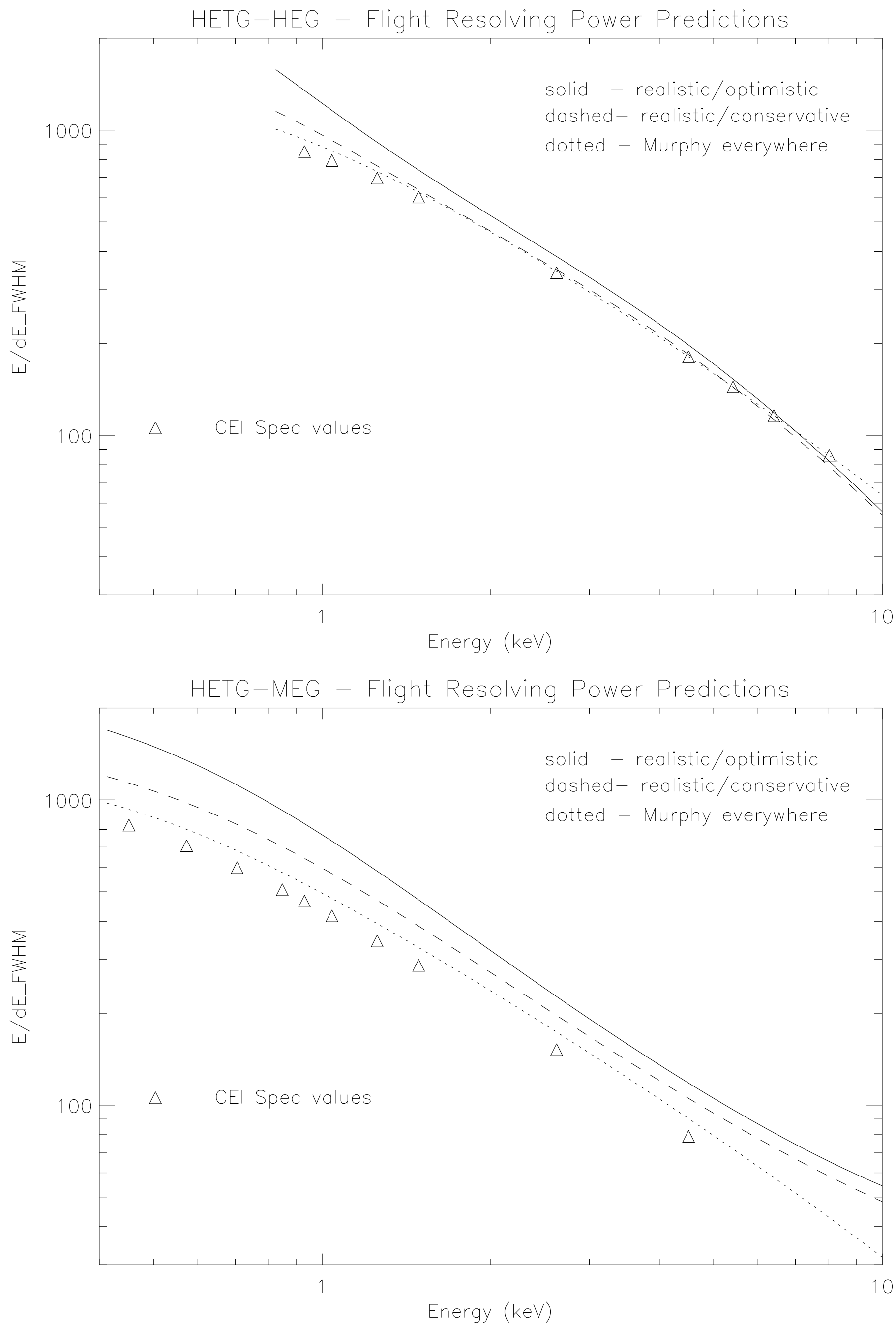

Figure 2.2: Resolving Power for the HEG and MEG spectra of the HETGS plotted vs. energy. The triangles are CEI specifications to be met, the dotted lines are the pre-fabrication worst-case (Murphy) detailed error budget used to ensure meeting specifications. The resolving power at high energies is dominated by the HRMA blur; at low energies the grating's effects become important.
The solid and dashed curves are the current range of realistic flight HETGS estimates. The "optimistic" solid curve is calculated from the parameters shown in Table 2.1 and related equations. The dashed curve is the same except for a (plausible) degradation in aspect, focus, and grating dp/p to: $a = 0.6, dx = 0.2, dp/p = 250 \times 10^{-6}$.

Error Term	*Error Parameter* symbol	value	units	Blur Equations (rms μm) dy',dispersion	dz',cross-disp.
HRMA PSF	σ_{H}	Equ. 2.6[2.7]	rms mm	σ_{H}	σ_{H}
Astigmatism	–			Equ. 2.8	Equ. 2.9
Period var.	dp/p	162[146]	$\times 10^{-6}$ rms	Equ. 2.10	–
Roll var.	γ	1.5	arc min. rms	–	Equ. 2.11
Aspect	a	0.34	arc sec rms	Equ. 2.12	Equ. 2.12
Dither rate	R_{dither}	0.1	arc sec./s	Equ. 2.13	Equ. 2.13
Detector	σ_D	0.29×0.024	mm rms	σ_D	σ_D
	Input Parameters				
Energy	E	as desired	keV		
Defocus	dx	0.1	mm		
Readout time	t_{D}	3.3	s		
Period	p	4001.[2001.]	Å		
equiv Radius	R_0	470.[330.]	mm		
Rowland spacing	X_{RS}	8634.	mm		
Focal length	F	10065.5	mm		
Rowland offset	$\Delta X_{\mathrm{Rowland}}$	$\beta^2 X_{\mathrm{RS}}$	mm		
Diffr. angle	β	$\arcsin(\lambda/p)$	radians		
Wavelength	λ	hc/E	Å		
hc	hc	12.3985	ÅkeV		

Table 2.1: Simplified Resolving Power Error Budget Equations. The major terms which add blur to the HETG PSF are listed here. The effective rms contributions to the dispersion and cross-dispersion blur are rss'ed together to arrive at a Gaussian approximation to the PSF core in each direction. Note that the equations include unusual factors which convert the values to 1-sigma equivalents, *e.g.*, the rms blur added due to CCD-like pixelization is 0.29 times the pixel size. The parameter values listed here and in the equations are the current best estimates for the flight HETGS. Entries that are different for MEG and HEG are shown as "MEG_value[HEG_value]".

2.2.1 HRMA PSF

The HRMA on-axis, in focus, 1-dimensional projected PSF has a central cusp and extended wings. The result is that the FWHM of this 1-D profile is not a good indicator of the FWHM that will result when convolved with other (generally closer to Gaussian) error terms. In order to parameterize the HRMA for inclusion in this error budget is is useful to measure the "effective HRMA rms blur", σ_H. Define σ_T as the total Gaussian sigma that results from convolving the HRMA 1-D PSF with a Gaussian of width σ_o :

$$\sigma_T = \text{sigma}\{ \text{ HRMA PSF } \otimes \text{ Gaussian}(\sigma_o) \ \} \tag{2.4}$$

then the effective HRMA rms blur is defined as:

$$\sigma_H \ \equiv \ \sqrt{\sigma_T^2 - \sigma_o^2} \tag{2.5}$$

The effective HRMA blur thus depends on the scale at which it is used, σ_o, which is set by the other, non-HRMA, error terms in the error budget.

This procedure was carried out using the approximation to the flight HRMA embodied in the **MARX** software, Version 2.0. The following equations give good approximations to the value of σ_H when $\sigma_o \approx 0.0107\ mm$.

$$\sigma_{H,MEG} = 0.0090 \ + \ 0.0142 \log_{10} E \ + \ 0.0103 \log_{10}^2 E \ + \ -0.0157 \log_{10}^3 E \tag{2.6}$$

$$\sigma_{H,HEG} = 0.0131 \ + \ 0.0308 \log_{10} E \ + \ -0.0589 \log_{10}^2 E \ + \ 0.0540 \log_{10}^3 E \tag{2.7}$$

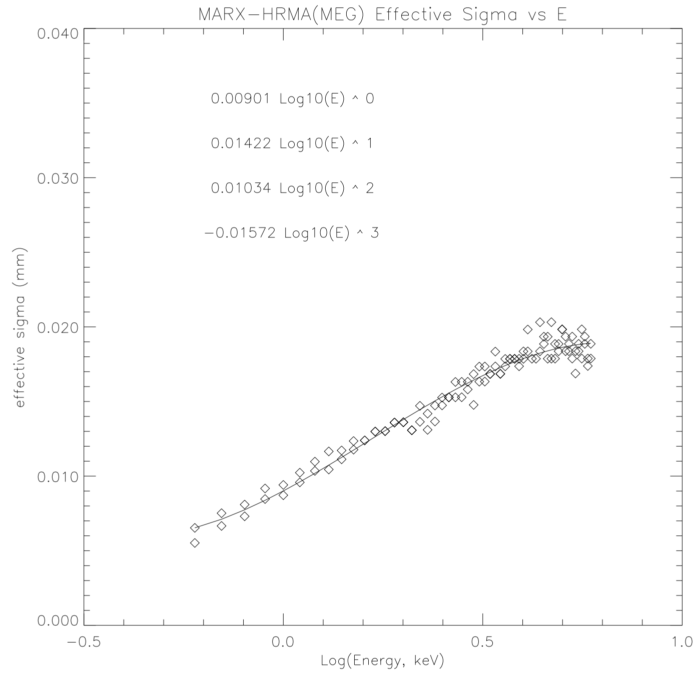

Figure 2.3: Fitting the **MARX** MEG HRMA Effective Blur

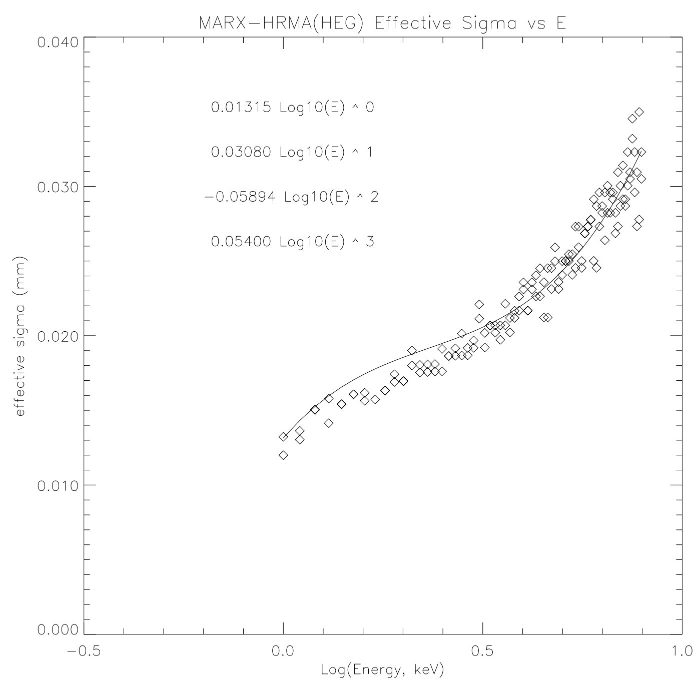

Figure 2.4: Fitting the **MARX** HEG HRMA Effective Blur

2.2.2 Rowland Astigmatism

Including the effect of a defocus, dx, and a factor converting the peak-to-peak blur into an rms equivalent, we get the following equations for the Rowland astigmatism contribution to the error budget:

$$dy' = 0.354 \, \frac{2R_0}{X_{\mathrm{RS}}} \, dx \tag{2.8}$$

$$dz' = 0.354 \, \frac{2R_0}{X_{\mathrm{RS}}} \, (\Delta X_{\mathrm{Rowland}} + dx) \tag{2.9}$$

These equations assume that the detector conforms to the Rowland circle except for an overall translation by dx (positive towards the HRMA). The values of R_0 used in the error budget are effective values – weighted combinations of the relevant mirror shells.

2.2.3 Grating Period and Roll Variations

There are two main error terms which depend on how well the HETG is built: i) period variations within and between facets ("dp/p") and ii) alignment ("roll") variations about the normal to the facet surface within and between facets. The period variations lead to an additional blur in the dispersion direction:

$$dy' \approx \beta X_{\mathrm{RS}} \frac{dp}{p} \tag{2.10}$$

where dy' and dp/p are rms quantities. The roll errors lead to additional blur in the cross-dispersion direction through the equation:

$$dz' \approx \beta X_{\mathrm{RS}} \; \gamma \; (\frac{1}{57.3})(\frac{1}{60}) \tag{2.11}$$

where dz' and γ are rms values in units of mm and arc minutes respectively.

2.2.4 Aspect and Dither Blurs

Aspect reconstruction adds a blur that is currently expected to be $a = 0.34$ arc seconds rms diameter (Aldcroft memo 6/18/97). The resulting one-dimensional rms sigma is thus:

$$dy', dz' = \frac{1}{2} \frac{\sqrt{2}}{2} \;\; F \;\; a \;\; (\frac{1}{57.3})(\frac{1}{3600}) \tag{2.12}$$

where F is the HRMA focal length in mm.

An additional blur is added because the arrival time of a photon at the detector is only known to an accuracy of the detector readout time, t_D. The product of this readout time and the aspect slew rate (basically the dither rate) is the size of the aspect error interval. The rms blur effect is 0.29 times this interval:

$$dy', dz' = 0.29 \quad F \quad R_{\text{dither}} \quad t_D \quad (\frac{1}{57.3})(\frac{1}{3600}) \tag{2.13}$$

2.2.5 Detector Blur

This error term is the spatial error introduced by the detector readout scheme.

For a pixelated detector like ACIS we assume that the PSF drifts with respect to the detector pixels and there is a uniform distribution of the centroid location in pixel phase. In this case the reported location of an event is the center of the pixel when in fact the event may have actually arrived ± 0.5 pixel from the center. The rms value of such a uniform distribution is 0.29 times the pixel width:

$$\sigma_D = 0.29 \times \text{pixel size} \tag{2.14}$$

For a detector like the HRC, the value σ_D is simply the sigma of the gaussian blur added by the detector.

2.3 Ray-trace Model: MARX

The design of the HETG has required ray-trace software in addition to simple error budgeting. Tom Markert initiated these efforts by using Webster Cash's IRT (interactive Ray-Trace) IDL package. This IRT framework was also used for the "error-budget-ray-trace" work (to be) described in the previous section. In addition, IDL lookup table software (`axaf1.pro`) was developed by the HETG team for effective area studies and simulations. With the addition of ASC personel at MIT these HETG modeling efforts evolved into a pseudo ray-trace IDL code, `sim`, which was then ported to C (`csim`). Because of in-house physics/software expertise (John Davis), `csim` evolved from an error-budget-efficiency combination into a full up ray-trace code. Finally, for release as an ASC product `csim` was renamed **MARX** .

MARX , therefore, is the main HETG ray-trace code and is a joint ASC/HETG effort. It is planned that **MARX** embody all relevant effects for HETGS modeling and simulation.

Please see `http://space.mit.edu/ASC/software/software.html` for more information on **MARX** .

`To-do:`
Cross-check **MARX** with SAOSAC simulations for XRCF and flight conditions
Compare **MARX** output with XRCF data
Include MEG mis-aligned gratings into **MARX** .
Evaluate the need and method to include HEG scattering in **MARX** .
Generate LRFs for LRF parametrization and RMF creation

Section 3

Efficiency Physics and Model

The key physics to model the HETGS effective area comes in at the level of the single-grating diffraction efficiency $g_f(E,m)$ appearing in Equation 1.4. In order to achieve high diffraction efficiencies, we are operating outside the range of the simple diffraction theory[5] of opaque bars and instead in a region where the grating bars transmit and phase-shift the X-rays. Guided and assisted by Dale Graessle and his AXAF witness mirror work at NSLS[22], Tom Markert and Christie Nelson initiated grating synchrotron measurements of diffraction efficiency, reported in Nelson *et al.*[36] and Markert *et al.*[31]. These studies have allowed us to verify the phased non-rectangular model, provided reference standards for laboratory tests, and provided more accurate optical constant data for the materials in our gratings. The state of our synchrotron measurements and modelling efforts was most recently detailed by Flanagan *et al.*[18]. Although this work is ongoing, the fundamental result was a detailed physical model of grating diffraction that applies to individual gratings $g_f(E,m)$ and has been measured at many finely spaced energies. Cross-testing of several gratings in the X-GEF lab and at synchrotron facilities allows us to put constraints on the efficiency models produced from X-GEF tests.

3.1 Diffraction Theory and Models

3.1.1 Scalar Diffraction Theory

The model we use is the simple scalar (Kirchoff) diffraction theory [5]; rigorous diffraction theory, using the vector properties of the electromagnetic field and appropriate boundary conditions for the grating bars, is not required so long as the wavelength of the light being considered is much less than the period of the grating. Since we are dealing with, at most, wavelengths of 30 Å, and the grating period is no less than 2000 Å(for the HEG gratings) this condition is fulfilled fairly well. We note that the scalar model will begin to err at the lowest energies of interest, and that we will have to consider the more rigorous method (at least at the lower energies) as we continue to refine the model.

The general formula for the efficiency of a periodic grating, using the Kirchoff diffraction theory with the Fraunhofer approximation is ([5, 24]):

$$\eta_{(m)}(k) = 1/p^2 \times [\int_0^p e^{ik(\nu-1)z(\xi)-2\pi mi\xi/p} d\xi]^2 \tag{3.1}$$

where $\eta_{(m)}$ is the efficiency in the mth order, k is the wavenumber ($= 2\pi/\lambda$), ν ($= \nu(k)$) is the complex index of refraction, p is the grating period, and, $z(\xi)$ is the grating bar shape function. The bar shape function $z(\xi)$ may be thought of as the shape of the cross-section of the grating bar for X-rays normally incident on the grating surface.

In addition to the parameters indicated in equation 3.1, there are other factors which effect the measured diffraction efficiencies. These are the absorptions of the support film (see Figure 1.2) and the plating base. The grating is built up onto a thin (0.98 μm for the HEGs, 0.55 μm for the MEGs) polyimide film which provides mechanical support. In addition, there are very thin metallic films ($\simeq$ 200 Å of gold and 50 Å of chromium) which are used for the electroplating process. These films are essentially uniform over the grating and serve only to absorb (and not diffract) X-rays. However, their absorption introduces edge structure which has been investigated through testing at synchrotrons (described below).

Thus, the parameters for the scalar model (with absorption) of the HETG gratings are:

$\beta(k)$ and $\delta(k)$, the components of the index of refraction for gold

$z(\xi)$, the bar shape function (note that the grating period is not an explicit parameter, but only scales the bar shape)

t_{au}, the thickness of the gold plating base

t_{cr}, the thickness of the chromium plating base

t_{poly}, the thickness of the polyimide support film

$\beta_{polyimide}(k)$ and $\beta_{cr}(k)$, the imaginary parts of the index of refraction, which give the transmission of the support film and the plating base.

3.1.2 Rectangular Models

Consider the grating model without regard to the aborbing support layers. For a rectangular wire profile[43], i.e, where

$z(\xi) = h$ for $0 < \xi \leq p - a$, and

$z(\xi) = 0$ for $p - a < \xi \leq p$,

equation 3.1 becomes

$$\eta_{(m)}(k) = [\frac{sin(\frac{m\pi a}{p})}{m\pi}]^2 \times [1 + e^{-2k\beta h} - 2e^{-k\beta h} cos(k\delta h)] \qquad m \neq 0 \tag{3.2}$$

and

$$\eta_{(0)}(k) = (a/p)^2 + (1-a/p)^2 e^{-2k\beta h} + 2(a/p)(1-a/p)e^{-k\beta h} cos(k\delta h) \qquad m = 0. \tag{3.3}$$

Here a is the width of the space between grating lines and p is the period. As before, δ and β are the complex components of the index of refraction ν. Note that ν, δ, and β are all functions of the X-ray wavelength, i.e., $\nu(k) = 1 - \delta(k) + i\beta(k)$. If βh is very large (i.e., the grating bars are opaque) then there is no wavelength dependence of the diffraction efficiency. The HETG gratings are designed such that the grating bars are partially *transparent* at higher energies, and so the phase shift of the X-rays through the bars (the δ term) actually enhances the efficiency at some energies. Gratings with this property are call *phased* transmission gratings.

For a quantitative look at the higher efficiency of phased gratings as compared to opaque gratings, equations 3.4 and 3.5 below show the grating efficiencies (where η is now the sum of the grating efficiencies of the +1 and −1 orders):

$$\eta_{opaque} = 2 \times \frac{sin^2(\frac{\pi a}{p})}{\pi^2} \tag{3.4}$$

$$\eta_{phased} = \eta_{opaque} \times [1 + e^{-2kh\beta} - 2e^{-kh\beta} cos(kh\delta)] \tag{3.5}$$

When absorption is ignored (the fully-phased case), equation 3.5 reduces to the following[43]:

$$\eta_{fully-phased} = 8 \times sin^2(\frac{kh\delta}{2}) \times \frac{sin^2(\frac{\pi a}{p})}{\pi^2} \tag{3.6}$$

From equation 3.6, it can be seen that at an optimal wavelength ($\lambda = 2h\delta$), the fully-phased grating efficiency is four times the opaque grating efficiency for this simple scalar diffraction theory. (A complete vector treatment of Maxwell's equations gives slightly different results at some energies.) At efficiencies near this one particular wavelength, partial destructive interference of the zeroth grating diffraction order occurs and the first grating diffraction orders are enhanced. The result is a range of wavelengths for which the grating efficiency is maximized.

The scalar model fits our data fairly well, even if a simple rectangular grating bar shape is assumed[36]. However, in order to match the data at the 1 per cent level, we find in general that more complex bar shape functions must be invoked. In addition, we have independent evidence, from electron microscope photographs that the bar shapes for the HETG gratings are not simple rectangles.

3.1.3 Vertex Model

The bar shape function function $z(\xi)$ can be reduced to a finite number of parameters. For example, if a rectangular bar shape is assumed, then z can be computed with two parameters, a bar width and a bar height. A more complex bar shape can be parameterized with arbitrary precision by dividing the bar into small rectangular sections.

For our modeling, the grating bar shape is parameterized as piece-wise linear, defined by the location of vertices, *e.g.*, Figures 4.8 and 4.9. The number of line segments is selectable, but there is little improvement in the quality of the fit after about 4 to 6 segments.

3.1.4 Tilted Grating Model

Another factor which makes a difference in the computed efficiencies in the various orders is the effect of tilting the grating, *i.e.*, changing the orientation of the grating surface normal with respect to the incoming X-rays. Given a grating bar cross-section, and a tilt angle (orientation of the incoming X-rays with respect to the grating plane), one can determine the grating bar shape function $z(\xi)$ from simple geometry. Since tilt and bar shape are complementary, we don't include tilt angle as a model parameter. (It is always possible to find an untilted grating with the same response as a tilted grating of an arbitrary shape. This equivalence only holds true at a given tilt angle, however. If one studies gratings over a range of angles, then one must generally use the actual bar cross-section.)

3.1.5 Trapezoidal Model

As an example of the complementarity between tilt and bar shape, consider a rectangular cross-section: When viewed at an angle, it has a trapezoidal $z(\xi)$. Moreover, the efficiency vanishes in all orders when the the grating is tilted by an angle $\theta = tan^{-1}(h/p)$, where h is the grating bar height and p is the period. (This relationship is clear because at that angle all of the X-rays incident on the grating see the same path length through the bars, hence there can be no diffraction.) Fischbach *et al.* [16] have reported on the theory and measurements of tilted rectangular gratings.

Except for a few bar cross-sections showing great symmetry, the efficiency in the positive and negative orders will be different at all but a few tilt angles. For example, Figure 3.1 shows the efficiency asymmetry in the plus and minus first orders for a trapezoidal grating at $E = 2.290$ keV, the energy of the Mo L α line. The asymmetry at a given tilt angle is defined as $100(I_{+1}/I_{-1} - 1)$. There is order symmetry at *normal* orientation (zero degrees tilt means that the incoming X-rays are normal to the grating plane), but at very few other angles.

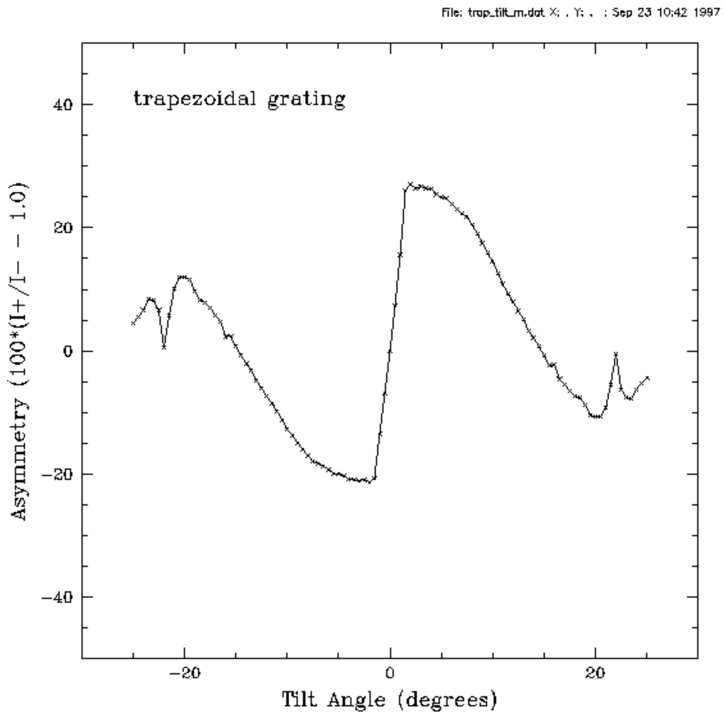

Figure 3.1: Asymetry parameter for a trapezoidal grating

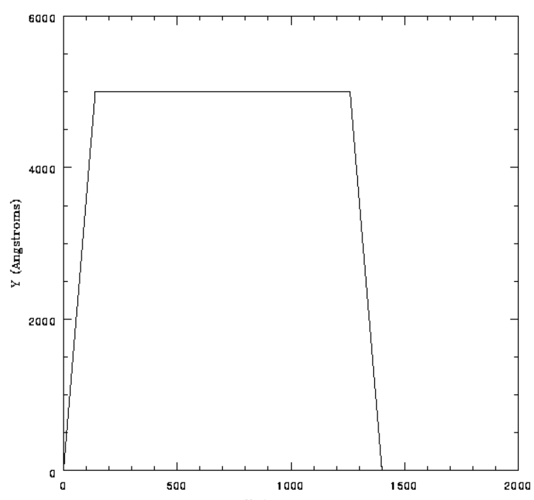

Figure 3.2: Trapezoidal bar shape assumed for the model above.

3.2 Synchrotron Measurements

3.2.1 Synchrotron Measurements Summary

The table below summarizes all the synchrotron tests which have been performed to date on HETG gratings or their prototypes.

Table 3.1: Summary of HETG synchrotron radiation tests

Date	Facility	Grating	Energy	Comments	Ref.
July '93	NSLS	HX101	2.03 - 4	preliminary tests	[35]
Nov '93	Daresbury	HX101	8.442	period variations (UL)	[35]
Jan. '94	NSLS	HX101	0.7 - 6	first tests	[36]
Jun. '94	NSLS	HA04	2.03 - 6		"
"	"	HX101	2 - 3.5	new gold optical constants	"
"	"	MA12	0.7 - 5	± 1 order assymetry	"
Feb. '95	NSLS	HX220	0.5 - 6.4	X-GEF reference grating	[31]
"	"	MX078	0.5 - 3.5	X-GEF reference grating	"
Oct. '95	NSLS	HA2021	2.03 - 6.5	flight lot 2, dense 0&1 orders	[18]
"	"	MA1047	2.1 - 5.0	flight lot 3, dense 0&1 orders	"
Oct. '95	PTB	HA2021	0.4 - 1.9	flight lot 2	"
"	"	MA1047	0.4 - 1.5	flight lot 3	"
"	"	HA2049	0.2 - 1.5	polyimide sample, flight lot 2	"
"	"	MA1066	0.2 - 1.5	polyimide sample, flight lot 3	"
Mar. '96	NSLS	HD2338	2.0 - 6.4	flight lot 4, ± 1 and higher orders	in prep
"	"	MB1148	2.1 - 4.9	flight lot 9, ± 1 and higher orders	in prep

3.2.2 Synchrotron Data Analysis Techniques

A complete description of the techniques employed in extracting diffraction efficiencies from synchrotron data is given in Flanagan *et al.*[18].

3.2.3 Gold Optical Constants and Edge Structure

When fitting the scalar model to the data we use the simplex technique to minimize the chi-square function. We allow all parameters to vary, except for the optical constants. There are too many optical constants (2 at each energy for gold alone), so fitting them isn't appropriate. On the other hand, the values of the β and δ are not well-enough known to allow us to use the published values uncritically.

Our initial tests (January 1994) at the National Synchrotron Light Source (NSLS) at Brookhaven National Laboratory (BNL) indicated a significant disagreement between the Henke values for the gold optical constants[23], and those required by our tests (our results were in basic agreement with those obtained earlier by Blake *et al.*[4] from reflection studies of gold mirrors). The most noticeable feature of the disagreement was that the energies of the prominent gold M absorption edges were shifted from the tabulated amounts by as much as 40 eV.

In an effort to determine more relevant optical constants, we measured the transmission of a gold foil with well-determined thickness and density in the energy range 2.03–6 keV at the NSLS using the X8A beam line. The transmission measurements yielded the complex part of the index of refraction (β) directly. We used the Kramers-Kronig relation (i.e., the dispersion relation linking δ and β) to compute the real part of the index of refraction, δ. The optical constants we required outside of this range were obtained by connecting the synchrotron-derived constants with those of Henke (at other energies) in a smooth way.

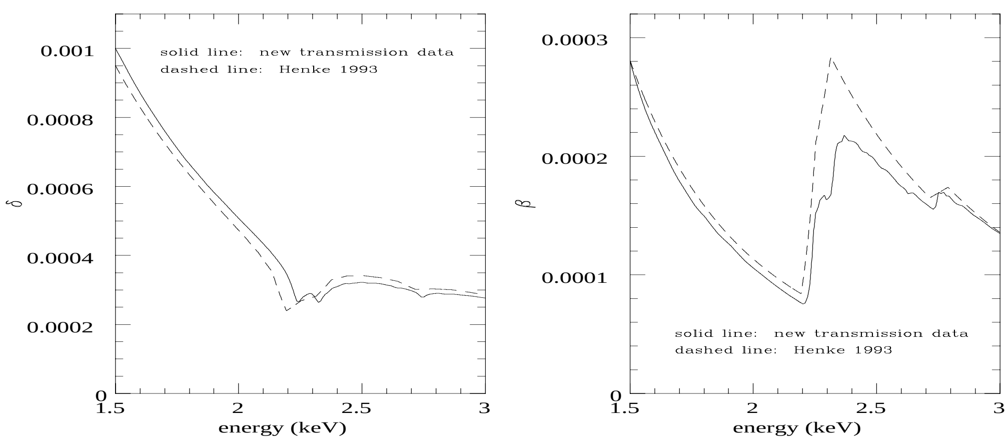

Figure 3.3: Comparison of optical constants from newly measured transmission data (solid lines) to those from the Henke tables (dashed lines). The plot on the left shows the values of the real part of the index of refraction, δ, and the plot on the right shows the values of the imaginary part of the index of refraction, β.

The optical constants we determined are shown in Figure 3.3, along with the Henke *et al.*[23] values. The constants are displayed near the gold MIII, MIV, and MV edges only (1.5 keV $<$ E $<$ 3 keV). Outside this energy range, the constants we derive are in good agreement with the Henke values.

The validity of the phased, non-rectangular model and the effectiveness of updated gold optical constants for energies above 2 keV are demonstrated in Figure 3.4 , where the synchrotron-measured diffraction efficiencies, sampled over many closely-spaced energies, agree well with the modeled efficiency for a flight-batch HEG grating. The residuals are shown in Figure 3.5 (only the first order data were used in the fit). The excellent agreement of the model with the data at the gold M edges is seen in better detail in Figures 3.6 and 3.7 for a flight-batch MEG grating. Note that the residuals at the gold edges are generally within 1%.

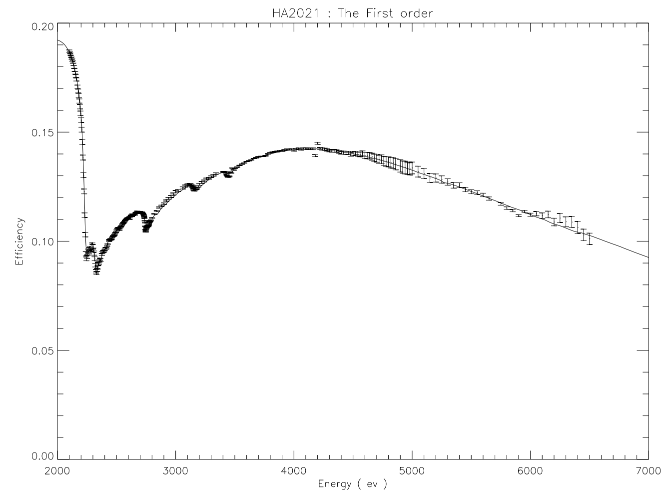

Figure 3.4: First order synchrotron data of HEG grating HA2021, overlaid with best fit model.

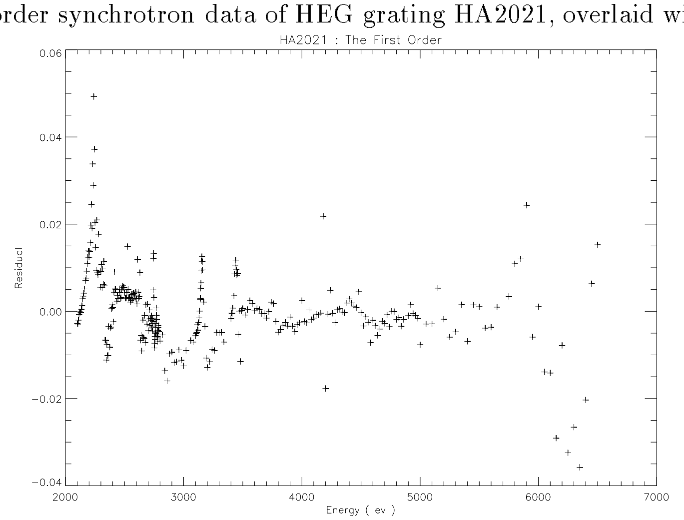

Figure 3.5: Residuals from the first order fit of grating HA2021.

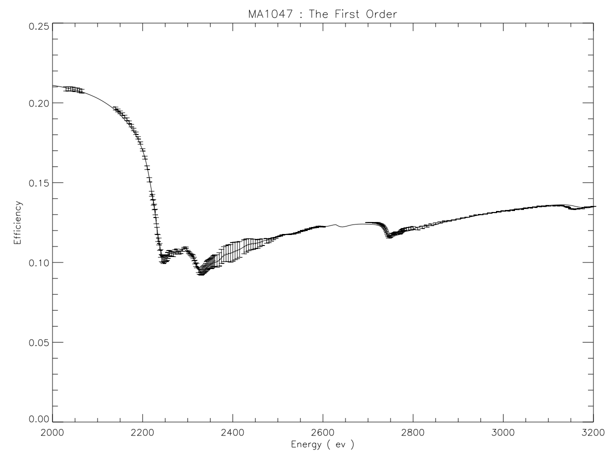

Figure 3.6: First order synchrotron data of MEG grating MA1047, overlaid with best fit model.

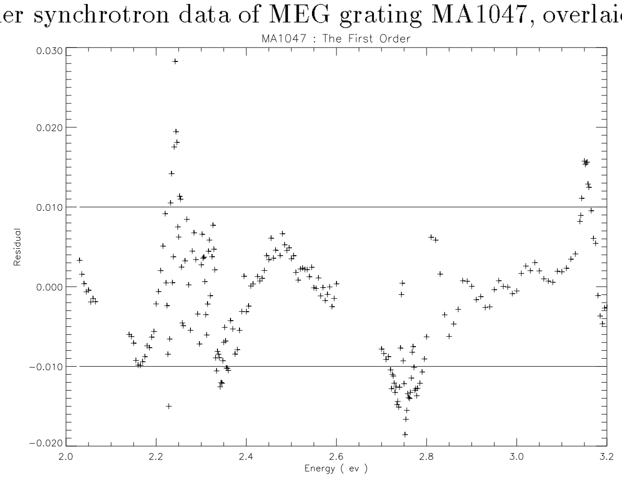

Figure 3.7: Residuals from the first order fit of grating MA1047. The horizontal lines are at $\pm 1\%$.

3.2.4 Polyimide Optical Constants and Edge Structure

Measurements of the gold optical constants have enabled the detailed gold edge structure to be well represented. A similar approach has been taken toward modeling the C, N and O edges of the polyimide. We have tested samples of polyimide from MEG and HEG flight batches at the radiometry laboratory of the PTB at BESSY[18]. The goal of these tests was to obtain the optical constants specific to our polyimide, but the results have not yet been incorporated into the modeling. Instead, the optical constants for the polyimide support film and the chromium plating base are taken from Henke, Gullikson and Davis[23]. The polyimide constants are determined by using the tabulated atomic constants for C,H,O, and N, and the chemical formula and nominal density for the polyimide formulation we use (Dupont 2610).

The data and best-fit model for an HEG grating are shown in Figure 3.8 for the whole energy range tested. Figure 3.9 shows the residuals over this range, but excludes the polyimide edges. Figure 3.10 details the data and model at these edges. The model is clearly inadequate at the N and O edges: The residuals are given in Figure 3.11. Similar results have been found for the MEG grating MA1047. Thus, taking the model as a whole, the highest residuals are at the polyimide edges. Inclusion of the polyimide optical constants in the model is imminent, and the best-fit models for the individual gratings will be revised accordingly.

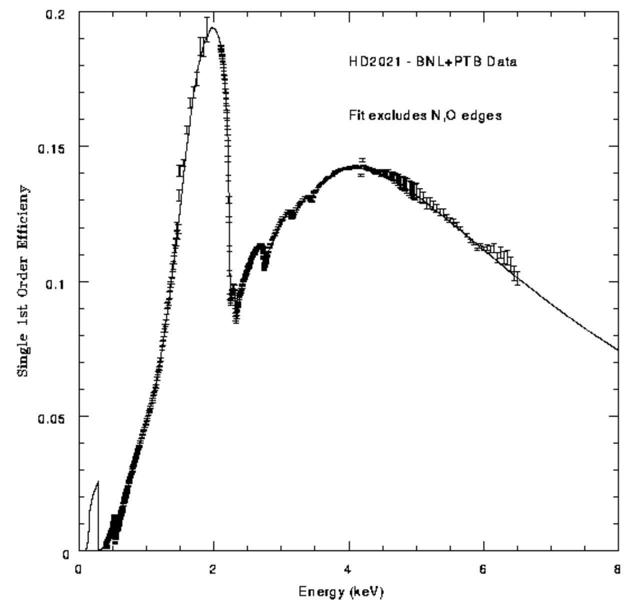

Figure 3.8: Data and best-fit model for grating HA2021 over full energy range of BESSY and Brookhaven tests.

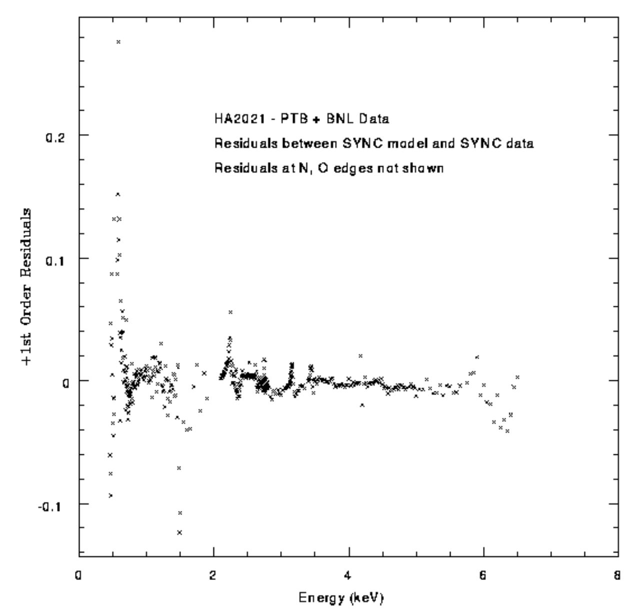

Figure 3.9: Residuals for grating HA2021 model when fit over full energy range; the fit excluded the polyimide edges. Currently, the highest residuals are at the polyimide edges, where Henke constants have been used.

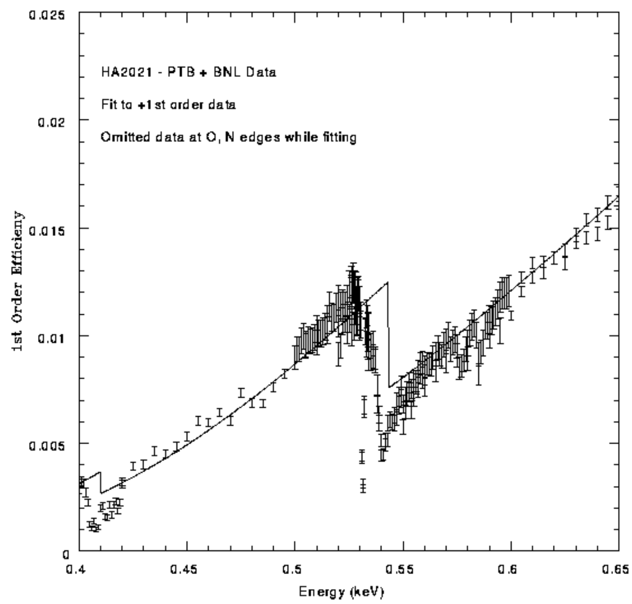

Figure 3.10: Data and best-fit model of grating HA2021 at polyimide edges.

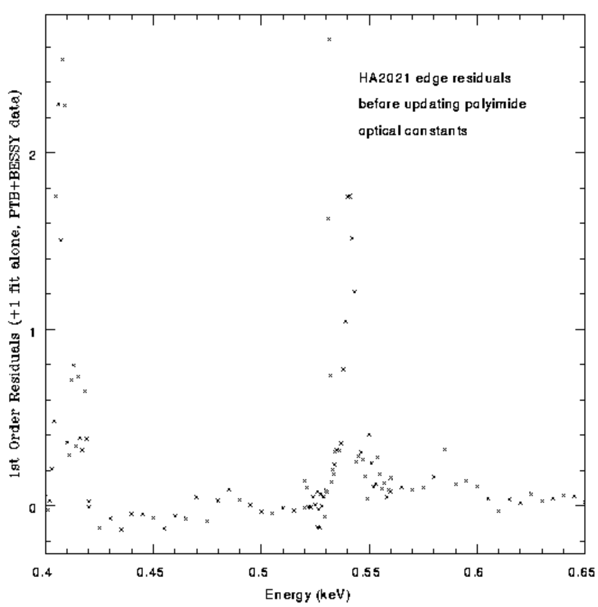

Figure 3.11: Residuals for grating HA2021 at polyimide edges, where Henke constants have been used.

3.2.5 Reference Grating Measurements

Although these data provide estimates as to the validity of our grating model, synchrotron tests are impractical to use for more than a few gratings. For the full set of flight gratings, the model parameters are determined from laboratory measurements on each grating element, using a standard (electron impact) type X-ray source and a few X-ray lines in MIT's X-Ray Grating Evaluation Facility (X-GEF). Gratings that have been tested at the synchrotron are used as transfer standards in each X-GEF test, to minimize systematic errors and allow normalization against a known efficiency. (Note, therefore, that the residuals of Figure 3.9 are *not* representative of the calibration of the individual gratings constituting the HETG.)

Two gratings, HX220 and MX078, were tested early in the program at a synchrotron (Markert *et al.*[31]). These are used as transfer standards in X-GEF testing; each X-GEF efficiency measurement is performed with an analogous measurement on the reference grating. Based on the assumption that the diffraction efficiency of the reference grating is correctly known at that energy, we obtain the efficiency of the test grating at the measurement energy. From measurements made at 5 or 6 energies in the laboratory, we then estimate the best-fit parameters (bar shape, gold thickness, space-to-period ratio) for the test grating and generate a model for its diffraction efficiency at all appropriate AXAF energies.

Figures 3.12 and 3.13 illustrate the quality of the model fit to the synchrotron data for the HX220 reference grating. Figures 3.14 and 3.15 show the data and fit for the reference grating MX078. These fits used both the first order and zeroth order data.

Tilt tests were performed in X-GEF on the two reference gratings. Figure 3.16 plots the asymmetry of MX078 versus angle at the Mo L line. MX078 exhibits no substantial asymmetry (confirming results found at Brookhaven). Figure 3.17 shows the asymmetry parameter found for HX220, the HEG reference grating. For reference, we have overlaid the results found in a tilt test performed at Brookhaven, which shows substantial agreement. The modeling for HX220 is discussed in Markert, *et al.*[31]

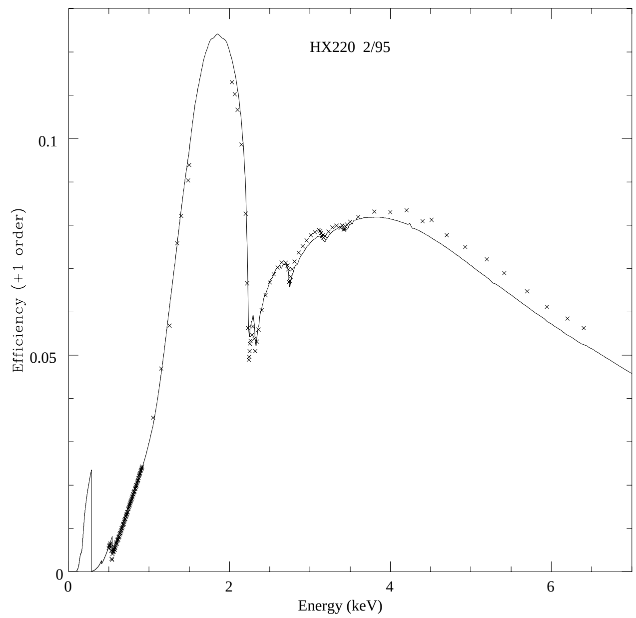

Figure 3.12: Data and best-fit model of reference grating HX220.

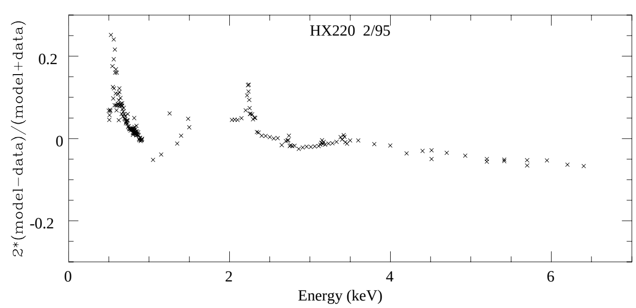

Figure 3.13: Residuals for reference grating HX220.

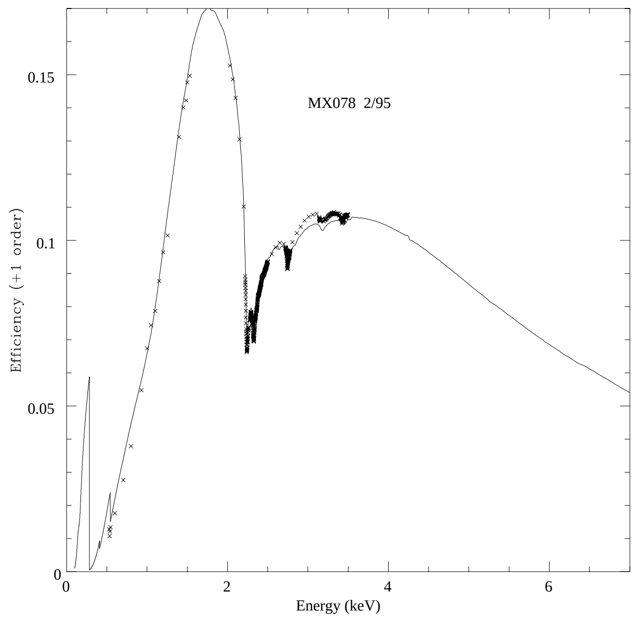

Figure 3.14: Data and best-fit model of reference grating MX078.

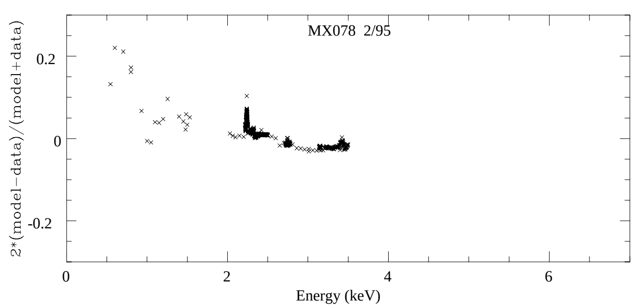

Figure 3.15: Residuals for reference grating MX078.

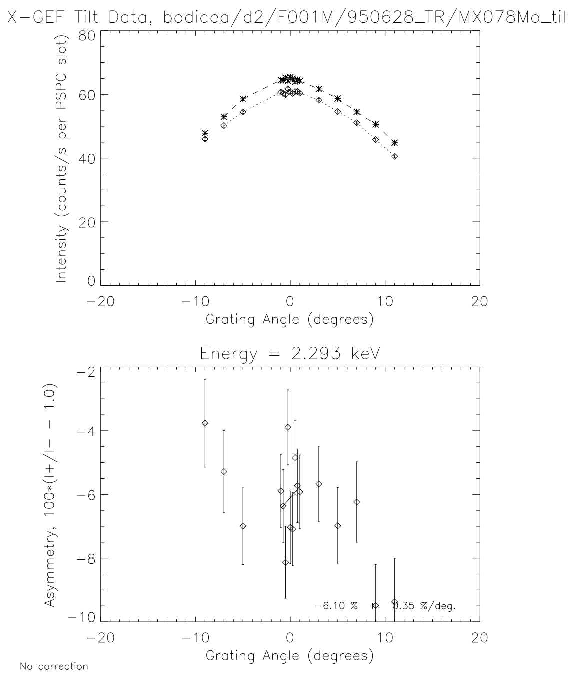

Figure 3.16: The X-GEF tilt test data for MX078 confirms the synchrtron result of a minimal tilt-induced asymetry.

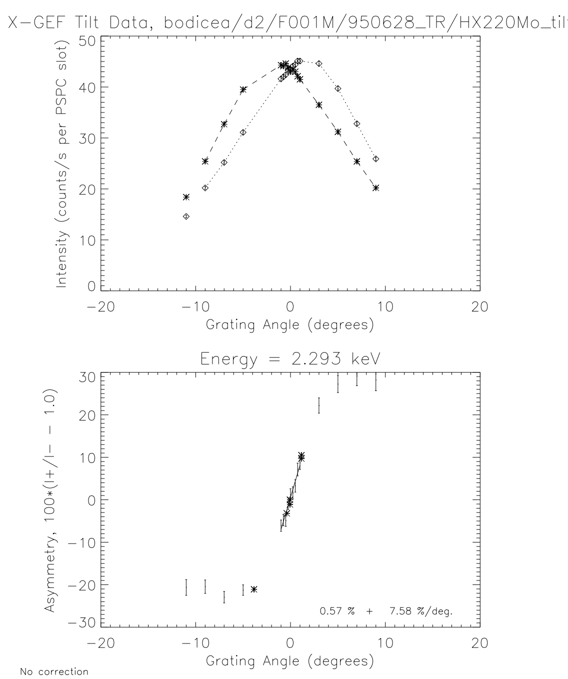

Figure 3.17: The X-GEF tilt depencance for HX220 agrees with measurements made in a tilt test at NSLS, overlaid(*). An angular offset if 1.15 degrees has been added to the NSLS measurements.

3.2.6 Error Estimates for X-GEF Predictions of Grating Efficiency

Four gratings have been cross-tested both at X-GEF (using standard flight testing and analysis prodecures including the reference gratings to normalize their efficiencies) and at the synchrotron. By comparing the X-GEF derived efficiency model with the synchrotron measurements, we have an estimate of the errors implicit in using X-GEF to predict the efficiencies for each grating facet. The residuals between the X-GEF generated model and the synchrotron data are shown in Figure 3.18 and 3.19. In effect, this provides an *upper limit to the errors of our subassemby efficiency predictions*, because a large strip of the reference grating is in fact illuminated in each X-GEF test, and the diffraction efficiency of this strip is (incorrectly) assumed to have the synchrotron reference efficiency. Only a small portion of the reference grating was actually tested at the synchrotron and it is only this small portion which should actually be assigned the reference efficiency. Therefore, the assignment of this fixed efficiency to a much larger area of the reference grating is incorrect. Tests have been done to cross-normalize the strip efficiency in comparison to the confined area for each grating, but the results have not been included yet.

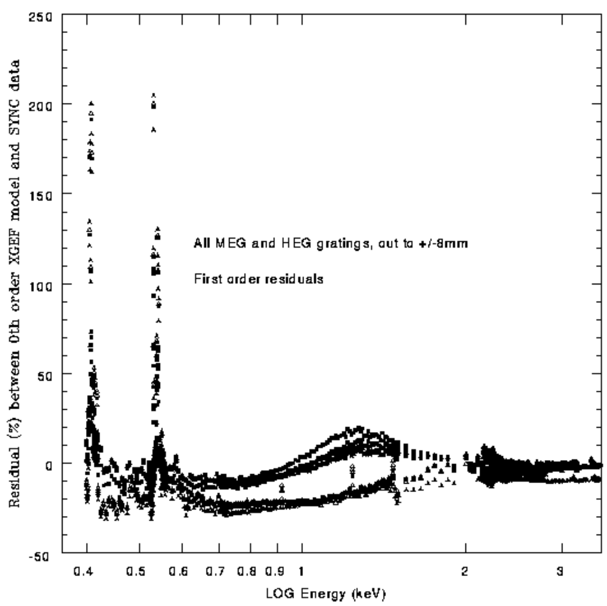

Figure 3.18: Residuals between first order X-GEF predictions and synchrotron data.

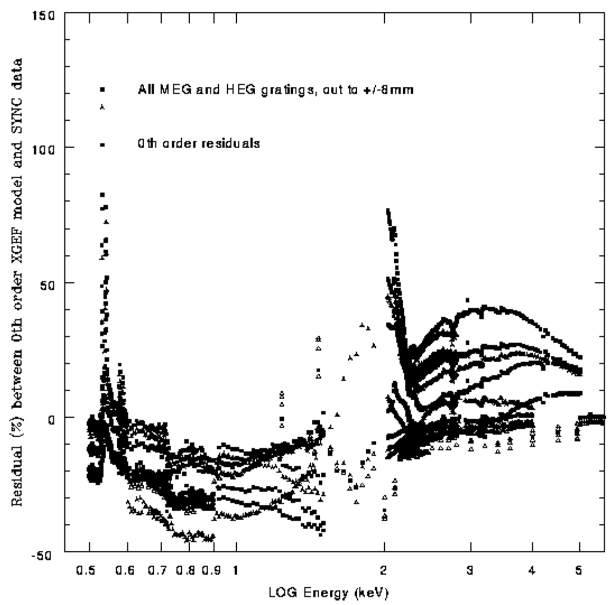

Figure 3.19: Residuals between 0th order X-GEF predictions and synchrotron data.

3.2.7 Synchrotron Analysis Status

1. The non-rectangular phased model is used in the X-GEF-modeling technique, its errors estimated and it has been documented in the literature.

2. Updated gold optical constants are also employed in this modeling.

3. Reference gratings have been assigned efficiencies based on early synchrotron tests. These values need to be examined and errors attached, reflecting increased knowledge of the synchrotron beamline systematics obtained in subsequent tests. The biggest considerations are:

    - Reconsideration of the cross-calibration techniques (high priority)
    - Careful examination of the multilayer data (below 2.03keV) which may contain low-energy contamination. (high priority)
    - Applying wing corrections and error bars.

4. Reference grating efficiencies are applicable to a small spatial region of each reference grating, but have been assumed for large regions in X-GEF tests. Cross-normalization tests have been performed in X-GEF (in a test procedure labeled BRLONG), so that efficiencies over a large strip can be normalized to the central section, and a proper reference efficiency can be assigned for the large test strip. This needs to be completed.

5. The results of projects (3) and (4) will provide new efficiencies and errors for the reference gratings as used in X-GEF tests. These improved reference efficiencies can then be transferred to the flight grating measured efficiencies. Finally, new model fits can be calculated for each tested region of each flight grating.

6. Data are in hand for examining C, N and O edge structure. The procedure will be:

    Model the edge structure by extracting effective optical constants for HETG polyimide as obtained from PTB-tested flight samples. This may involve first fitting the polyimide with a variable ratio of C,N and O as publish literature has suggested.

    Use these "new" optical constants and find the best-fit model for PTB-tested flight gratings. The residuals between the data and our model represent the expected errors for the model in general. In addition, the residuals between the data and the corresponding X-GEF model give us an estimate of the errors of the X-GEF-generated model. (high priority)

    Synchrotron data for C, N and O edges for flight batch MEG and HEG polyimide have been supplied for use in MARX as of 8/11/97.

7. Finish analysis of NSLS tests of gratings HD2338 and MB1148, to examine ratios of higher orders to first order.

8. Look into modeling with vector theory.

9. Look for evidence of scattering in synchrotron data.

3.3 Scattering Model

Recent tests of the HEG gratings indicate that there is scattering along the dispersion direction near first order, Section 6.6. The scattering observations are consistent with small ($\approx 2\%$) deviations of grating bar shapes from their ideal shapes. The theory to support this model is detailed below.

3.3.1 General Scattering Theory

Consider a diffraction grating composed of N lines with period d and a photon with wave number $k = 2\pi/\lambda$ incident upon the grating. It follows from Huygens principle that the *amplitude* for scattering by an angle θ with respect to the normal of the grating is given by[1]

$$I_N(k,s) = \frac{1}{N}\sum_{j=0}^{N-1} e^{ijksd} F_j(k,s), \tag{3.7}$$

where $s = \sin\theta$ and the *structure factor* $F_j(k,s)$ is defined by

$$F_j(k,s) = \frac{1}{d}\int_0^d \mathrm{d}x\; e^{iksx + i\phi_j(x)}. \tag{3.8}$$

The shape and composition of an individual grating element determines the phase shift $\phi_j(x)$. In general, $\phi_j(x)$ is a function that depends upon energy and, possibly, the polarization of the photon. Assuming the validity of scalar diffraction theory, the phase shift can be written in the form

$$\phi_j(x) = -k(\delta - i\beta) z_j(x), \tag{3.9}$$

where δ and β are energy dependent functions related to the dielectric constant of the grating bars. The function $z_j(x)$ represents the path length of the photon as it passes though the *jth* grating bar; it is sometimes called, rather loosely, the "grating bar shape", and more rigorously, the "path-length function".

In general, the structure factor $F_j(k,s)$ will vary with the grating bars because the "bar shape" will vary from bar to bar. Denote the average structure factor by

$$\bar{F}(k,s) = \langle F_j(k,s)\rangle \tag{3.10}$$

and define $f_j(k,s)$ to be the deviation of the *jth* bar from the mean via

$$F_j(k,s) = \bar{F}(k,s) + f_j(k,s). \tag{3.11}$$

Substituting the above definitions into (3.7) and taking the complex square to compute the intensity yields

$$|I_N|^2 = |\bar{F}|^2 \frac{\sin^2(\frac{Nksd}{2})}{N^2\sin^2(\frac{ksd}{2})} + \frac{1}{N^2}\sum_{j,l} e^{iksd(j-l)}\langle f_j f_l^*\rangle. \tag{3.12}$$

[1]The factor $1/N$ has been introduced to make $|I_N(s,k)|^2$ evaluated at the points $s = n\lambda/d$ numerically equivalent to the grating efficiency. $|I_N(s,k)|^2$ can also be thought of as the average intensity per grating element.

For very large N, the first term goes to zero like $1/N^2$ except when ksd is a multiple of 2π where it becomes independent of N. For such values, one obtains the familiar grating equation

$$n\lambda = d \sin\theta. \tag{3.13}$$

Thus, the first term represents the familiar interference pattern that consists of a $1/N^2$ background with a series of sharp peaks whose height is $|\bar{F}(k,s)|^2$ and whose width vanishes as $1/N$. The second term is more complicated and appears to go to zero as $1/N^2$. However, as will be seen, this is not necessarily true.

The quantites $\langle f_j f_l^* \rangle$ represent correlations between the various grating elements. If the shape of each grating element were independent of the others, then $\langle f_j f_l^* \rangle$ would vanish except when $j = l$. More explicitly, if no correlations are present,

$$\langle f_j f_l^* \rangle = \langle |f_j|^2 \rangle \delta_{jl}. \tag{3.14}$$

Assuming the absence of correlations and the reasonable assumption that $\langle |f_j|^2 \rangle$ is independent of j, the second term of (3.12) reduces to

$$\frac{1}{N} c_0^2(k,s) \tag{3.15}$$

where $\langle |f_j|^2 \rangle$ has been denoted by c_0^2.

In general $F_j(k,s)$, and hence $c_0(k,s)$, is a slowly varying function of s. This means that the intensity as a function of s will consist of sharp spikes at values of s satisfying the grating equation on top of an extended, very weak but non-zero scattering background.

If there are correlations between the various grating bars, (3.14) is not correct. In general, we expect any correlations that may be present to have a short range. That is, it is reasonable to assume that $\langle f_j f_l^* \rangle$ is zero for $|j - l|$ greater than some number M. For example, if $M = 1$, then only nearest neighbor correlations may be present. If $M \ll N$, then one may neglect edge effects and write the scattering term in (3.12) as

$$\frac{1}{N^2} \sum_{j=0}^{N-1} \sum_{m=-M}^{M} e^{imksd} \langle f_j f_{j+m}^* \rangle. \tag{3.16}$$

With the assumption that the grating is homogeneous on the scale set by the correlation length M, $\langle f_j f_{j+m}^* \rangle$ cannot depend on j and the scattering term reduces to

$$\frac{1}{N} \sum_{m=-M}^{M} e^{imksd} c_m(k,s) \tag{3.17}$$

where c_m has been defined by

$$c_m(k,s) = \langle f_j(k,s) f_{j+m}^*(k,s) \rangle. \tag{3.18}$$

Using the property that $c_{-m} = c_m^*$, which follows from the definition of c_m, and separating out real and imaginary parts, it follows that (3.12) may be written

$$|I_N|^2 = |\bar{F}|^2 \frac{\sin^2(\frac{Nksd}{2})}{N^2 \sin^2(\frac{ksd}{2})} + \frac{c_0^2}{N} + \frac{2}{N} \sum_{m=1}^{M} \left\{ \Re c_m \cos(mksd) + \Im c_m \sin(mksd) \right\} \tag{3.19}$$

The previous equation shows that the intensity pattern will consist of sharp diffraction peaks on top of a very weak but diffuse scattering background. The actual angular dependence of the diffuse scattering will depend upon the precise nature of the correlations and upon the correlation length given by M. Because of energy conservation, the scattering will reduce the height of the diffraction peaks. That is, the effectiveness of a grating whose bar shapes fluctuate will be lower than one that is perfect.

The fact that the scattering produced by the fluctuations in the grating bar shapes goes like $1/N$, whereas the sharp peaks of the diffraction pattern are on the order of unity, is somewhat misleading. In actual practice, the detector will have a finite angular acceptance and one ends up measuring the intensity integrated over some small angular region defined by the resolution of the detector (e.g., a pixel). Since the diffraction peaks have a width that scales like $1/N$, the integrated intensity will also go like[2] $1/N$. The end result is that the $1/N$ power of a diffraction peak is confined to a very tiny spatial region whereas the $1/N$ power of the scattering is smeared across a large region.

One can make these comments more precise as follows. It is well known that the sequence of functions

$$2\pi\delta_N(x-a) = \frac{\sin\frac{1}{2}N(x-a)}{\frac{1}{2}(x-a)} \tag{3.20}$$

approaches the delta distribution as N goes to infinity. For very large N, $\delta_N(x-a)$ is very sharply peaked about the point $x = a$ with the height of the peak given by N. Using this function, the first term in (3.19) may be approximated by[3]

$$|\bar{F}(k,s)|^2 \cdot \frac{2\pi}{N}\delta_N(ksd - 2\pi n) \tag{3.21}$$

where n is an integer that denotes the diffraction order. Let Δs denote the angular resolution of the detector and define $s_n = 2\pi n/kd$. The probability that a photon will be detected at the position s with $s_n - \Delta s/2 <= s < s_n + \Delta s/2$ is proportional to

$$\int_{s_n-\Delta s/2}^{s_n+\Delta s/2} \mathrm{d}s\ |I_N(k,s)^2| \approx \frac{2\pi}{N}\frac{1}{kd}|\bar{F}(k,s_n)|^2 \tag{3.22}$$

where the contribution from the scattering terms in (3.19) has been neglected.

Outside this angular range away from a diffraction peak, $\delta_N(ksd-2\pi n)$ is effectively zero and the scatter terms cannot be neglected. With the assumption that the correlation functions $c_m(k,s)$ do not vary much with s from pixel to pixel, the probability that a photon will scatter into an adjacent pixel is approximately proportional to

$$\frac{\Delta s}{N}\left\{c_0^2(k,s_n) + 2\sum_{m=1}^{M}\Re c_m(k,s_n).\right\}. \tag{3.23}$$

3.3.2 Scattering Example: Grating Bar Shifts

As an example, suppose that the N grating bar shapes differ from one another only by a shift. That is, grating for the jth bar is assumed to be given by $z_j(x) = z(x + a_j)$ where a_j denotes

[2] One must not be alarmed by this result. The normalization employed here means that the intensity is for a *single* grating element.

[3] Note that care has been taken to avoid the square of δ_N since it is well known that the square of a delta function is meaningless.

the shift of the jth bar. Furthermore, assume that $z(x)$ is non-zero only for values of x such that $|a_j| <= x <= d - |a_j|$ for all j. Physically, this means that the center of the grating bar whose shape is described by $z(x)$ lies near middle of the grating element. Then, the structure constant F_j for the jth grating element can be written

$$\begin{aligned} F_j(k,s) &= \frac{1}{d}\int_0^d \mathrm{d}x\ e^{iksx+i\phi(x+a_j)} \\ &= \frac{1}{d}e^{-iksa_j}\int_{a_j}^{d+a_j} \mathrm{d}x\ e^{iksx+i\phi(x)} \\ &= \frac{1}{d}e^{-iksa_j}\left(\int_0^d + \int_d^{d+a_j} - \int_0^{a_j}\right)\mathrm{d}x\ e^{iksx+i\phi(x)} \end{aligned} \tag{3.24}$$

With the assumption that $z(x)$, and hence $\phi(x)$, vanishes for $x < |a_j|$ or for $x >= d - |a_j|$, the latter two integrations can be performed with the result

$$F_j(k,s) = e^{-iksa_j}F(k,s) + \frac{1}{iksd}(1 - e^{-iksa_j})(e^{iksd} - 1) \tag{3.25}$$

Here, $F(k,s)$ has been defined

$$F(k,s) = \frac{1}{d}\int_0^d \mathrm{d}x\ e^{iksx+i\phi(x)}. \tag{3.26}$$

From this, it trivally follows from (3.10), that

$$\bar{F}(k,s) = \langle e^{-iksa_j}\rangle F(k,s) + \frac{1}{iksd}(e^{iksd} - 1)(1 - \langle e^{-iksa_j}\rangle) \tag{3.27}$$

and we also deduce from (3.11) that

$$f_j(k,s) = \left[e^{-iksa_j} - \langle e^{-iksa_j}\rangle\right]\left[F(k,s) - \frac{1}{iksd}(e^{iksd} - 1)\right] \tag{3.28}$$

For values of $s = s_n$, these expressions reduce to

$$\bar{F}(k,s_n) = \langle e^{-i2\pi n a_j/d}\rangle F(k,s) \tag{3.29}$$

and

$$f_j(k,s_n) = (e^{-i2\pi n a_j/d} - \langle e^{-i2\pi n a_j/d}\rangle)F(k,s) \tag{3.30}$$

Thus this particular model of grating bar fluctuations produces no scattering in the immediate vicinity of zeroth order. The correlation function at $s = s_n$ reduces to

$$\langle f_j(k,s_n) f_l(k,s_n)\rangle = (\langle e^{-i2\pi n(a_j - a_l)/d}\rangle - \langle e^{-i2\pi n a_j/d}\rangle\langle e^{i2\pi n a_j/d}\rangle)|F(k,s_n)|^2. \tag{3.31}$$

Assume that the shift parameters a_j are independently gaussian distributed with a mean of 0 and a variance of σ^2. For such a distribution, one can show that

$$\langle e^{-i2\pi n a_j/d}\rangle = e^{-\frac{1}{2}(2\pi n\sigma/d)^2} \tag{3.32}$$

from which it follows

$$|\bar{F}(k,s_n)|^2 = |F(k,s)|^2 e^{-(2\pi n\sigma/d)^2} \tag{3.33}$$

and

$$c_m(k,s_n) = \delta_{m,0}|F(k,s)|^2(1 - e^{-(2\pi n\sigma/d)^2}). \tag{3.34}$$

Using these results together with (3.22) and (3.23) yields that the ratio of photons scattering in a region of size Δs around the nth order to those scattering into the nth order is roughly

$$\frac{kd\Delta s}{2\pi}[e^{(2\pi n\sigma/d)^2} - 1] \approx 4\pi^2 n^3 \frac{\Delta s}{s_n}(\frac{\sigma}{d})^2. \tag{3.35}$$

We see that, for this particular model, the scattering becomes much more important for higher orders. Taking $\sigma/d \approx 0.025$ and Δs as one tenth of the dispersion distance s produces the estimate that the background in the vicinity of first order will consist of roughly 0.25 percent of first order photons. This result is consistent in order of magnitude with the XRCF observation of first order photons at 1.775 KeV, Section 6.6.

Section 4

Laboratory Measurements and Predictions

The basic equipment for HETG laboratory testing, a Laser Reflection setup and the X-Ray Grating Evaluation Facility (X-GEF), are described in Dewey *et al.*[12] with more details of the X-GEF facility and its operation for flight testing presented in Flanagan *et al.*[17].

The gratings were mounted to the HESS at the HETG Alignment Facility where the average facet roll angle was set and measured based on the polarization alignment technique of Anderson *et al.*[2].

We have used these "sub-assembly" data (along with similar predictions for the HRMA and ACIS-S) to produce predicted curves as a baseline for comparison with the XRCF measurement results and an initial flight prediction.

Table 4.1: HETG laboratory setups and the parameters measured

Parameter	Lab Setup
Period	LR
Period variation	LR
Roll	Alignment
Roll variation	LR
Efficiency	X-GEF

4.1 LR Measurements

4.1.1 LR Period and Roll Variations

The key facet-level parameters that effect the HETGS LRF are the grating period variations (both within and between facets) and the grating alignment, or "roll", variations (again within and between facets). The facet period, period variations, and roll variations were measured using the Laser Reflection setup[12].

In the Laser Reflection test a laser beam (HeNe 632.8 nm for MEGs and HeCd 325.0 nm for HEGs) is directed sequentially at an array of locations on each grating facet (10x11 or 11x12 locations). At each location the angle of the reflected and diffracted beams from the grating are measured and a local period is computed. The test setup includes MEG and HEG period references which are measured along with the sample and ensure the stability of the measurements. Each execution of the LR test creates an ASCII data file (13Kb or 16Kb) which can be analyzed to create a period contour map, Figure 4.1, and estimates of the grating average period, P, and period variations, "dp/p". The data can be re-analyzed limited to the "active" region that is expected to be illuminated by the HRMA to get a more accurate estimate of the grating's effect on performace.

The expected HETG equivalent dp/p is expected to be less than 130 ppm rms for both HEG and MEG gratings based on the data summarized in Figures 4.2-4.4.

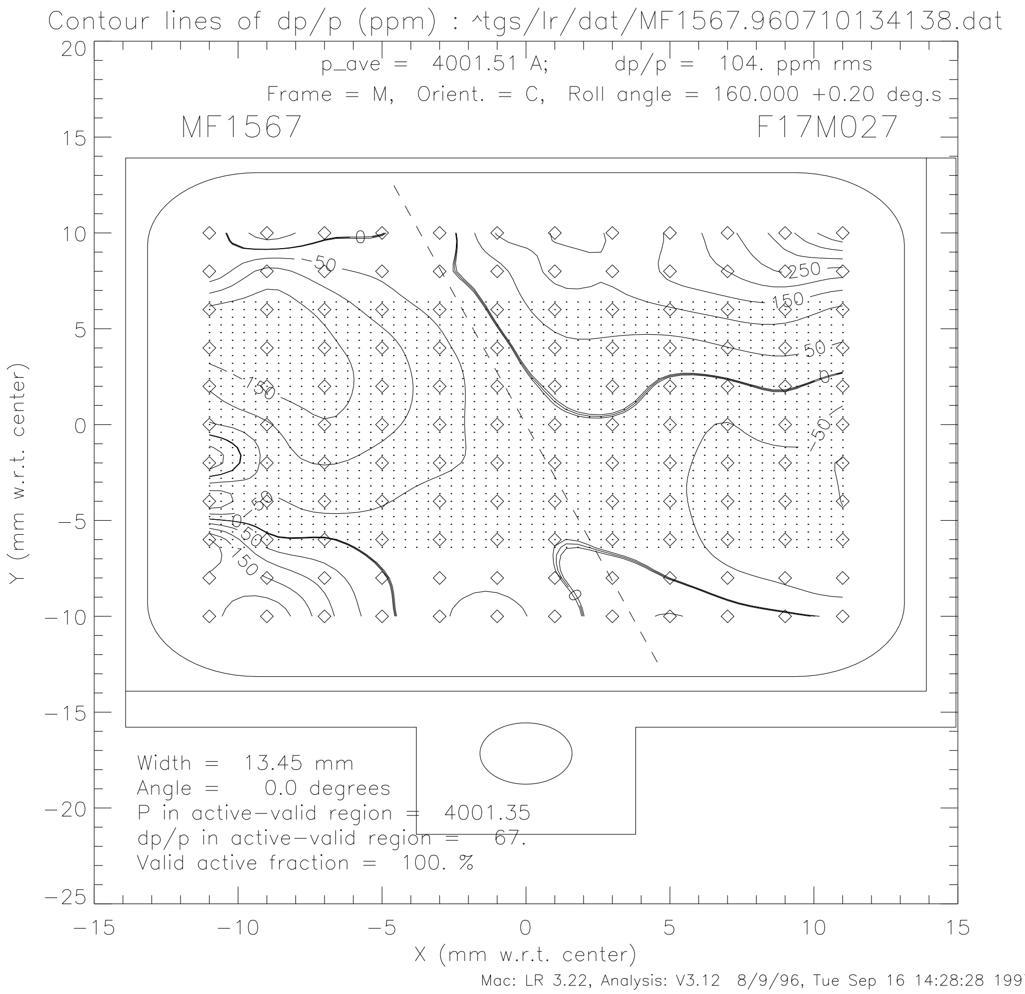

Figure 4.1: Period contour plot of MEG grating MF1567 from LR test data. Each diamond represents a measurement point. The dotted region is the "active" region that will be illuminated by X-rays from the HRMA. The period variation in the active region, dp/p = 67 ppm, is well below the required instrument variation of 250 ppm.

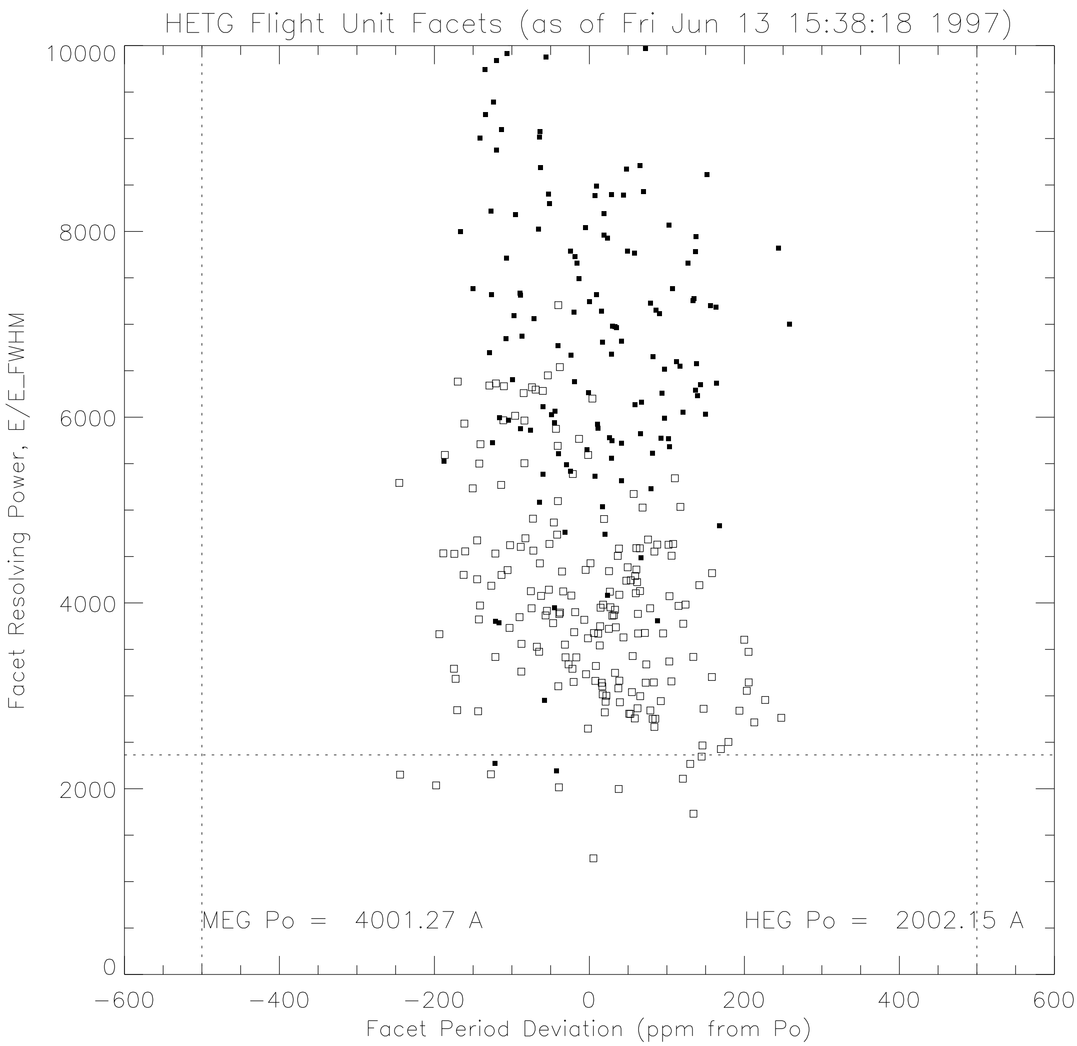

Figure 4.2: Period-dp/p scatter plot for the 336 HETG flight grating facets. The X-axis is each grating's departure from the average period for its type. The Y-axis is the inherent resolving power limit for the grating, that is: $(p/dp)(1/2.35)$. The horizontal dashed line at $E/dE \approx 2400$ corresponds to $dp/p = 180$ ppm.

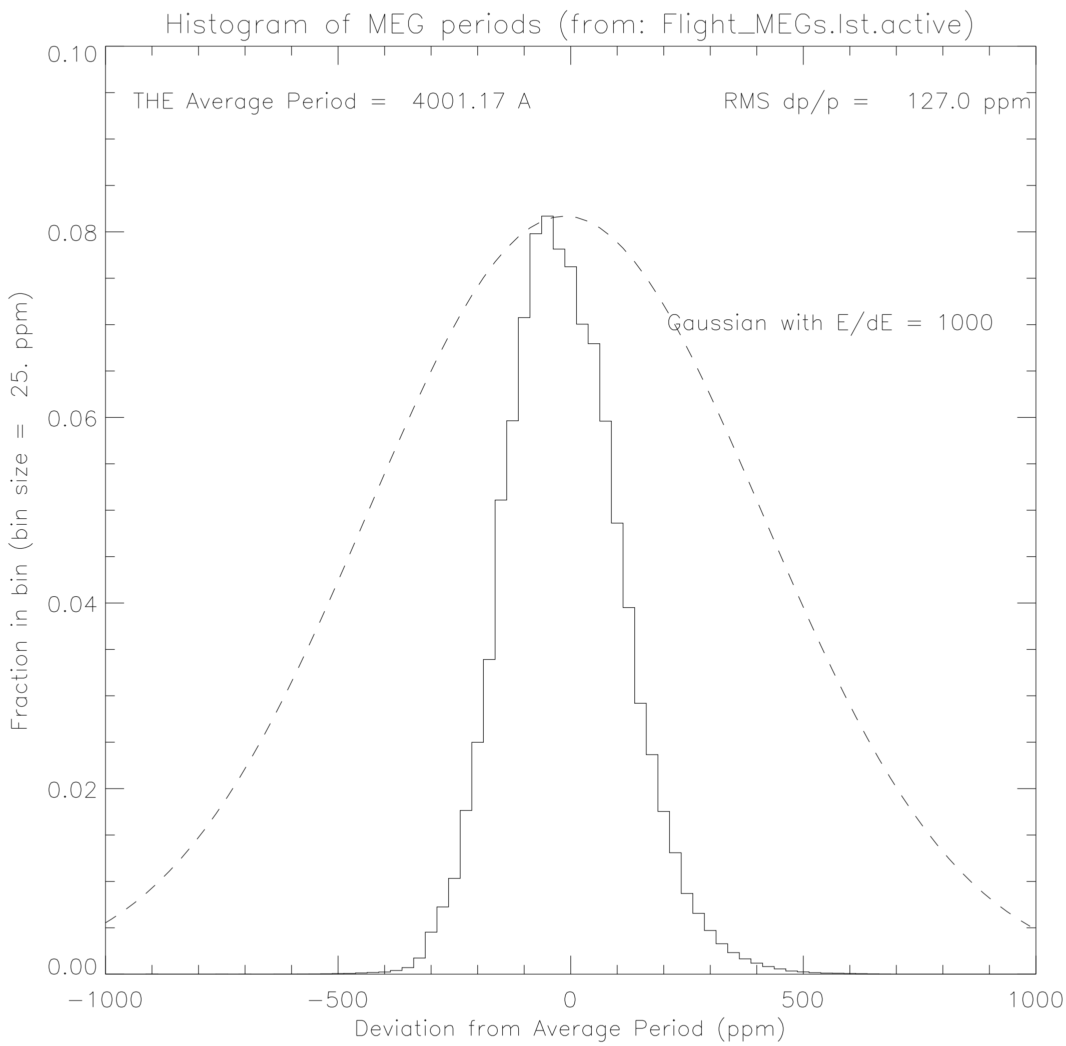

Figure 4.3: Period Histogram of the MEG Flight Gratings. The histogram and average period indicated here are based on the approximate "active" region of each facet. The rms dp/p value of 127 ppm corresponds to an E/dE limit of 3350. Note that the average period indicated here is in "LR-Å"; see Table 4.3 for the grating absolute periods.

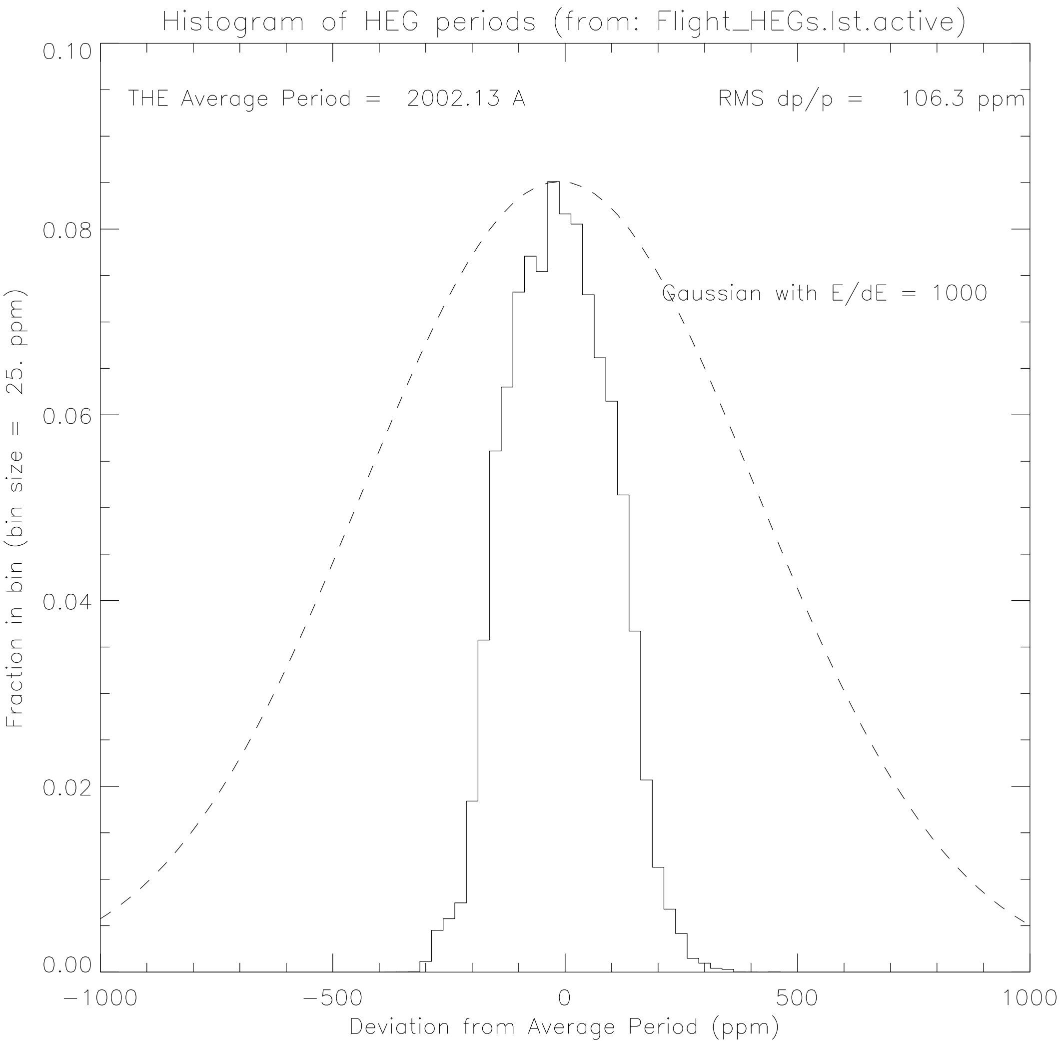

Figure 4.4: Period Histogram of the HEG Flight Gratings. The histogram and average period indicated here are based on the approximate "active" region of each facet. The rms dp/p value of 106.3 ppm corresponds to an E/dE limit of 4000. Note that the average period indicated here is in "LR-Å"; see Table 4.3 for the grating absolute periods.

4.1.2 LR Calibration using NIST Samples

The gratings on the flight HETG were each measured in the LR setup. The locations of the reflected and diffracted beams are measured from the grating under test and also from a fixed-in-the-instrument reference grating. Thus, all gratings are measured relative to fixed reference gratings (HEG or MEG). The periods of these reference gratings were assigned based on the laser wavelengths and the absolute diffraction angles (as measured by the encoded rotation stage.) The LR system has a high differential sensitivity and repeatability; however, its assigned periods are not expected to be absolutely accurate.

In order to set the absolute period of our reference gratings, we sent HEG and MEG calibration samples (on Silicon wafers) to John Kramar et al. at NIST (jkramar@NIST.GOV). They measured these HEG and MEG samples. Then these samples were measured by Dick Elder in the LR setup. From these measurements a *calibration factor* establishing the absolute period of our LR data is obtained, Table 4.2.

These calibration factors and errors are then applied to the measured average periods of the flight HETG and TOGA gratings yielding the final "LR-NIST" periods of Table 4.3.

Sample	NIST Period nm	NIST Error (1 σ) nm	LR Period Å[LR]	Calibration Factor Å/Å[LR]	Error ppm
NIST MEG	400.800	0.010	4007.74	1.00006	25.
NIST HEG	200.011	0.005	2001.43	0.999340	25.

Table 4.2: NIST samples for LR calibration

Grating	LR Average Period Å[LR]	LR-NIST Period Å	LR-NIST Error Å
Flight MEG	4001.17	4001.41	0.10
Flight HEG	2002.13	2000.81	0.05
TOGA MEG	4000.72	4000.96	0.10
TOGA HEG	2002.36	2001.04	0.05

Table 4.3: Correction of the LR Period Measurements

Please see `http://space.mit.edu/HETG/sub_details.html`

Figure 4.5: X-GEF Schematic

4.2 X-GEF Measurements

With the X-Ray Grating Evaluation Facility, X-GEF, at M.I.T. we have measured the diffraction efficiency of each flight grating at several energies and orders and fit these measurements to determine the physical-model parameters for each grating. From these best-fit parameters we can generate $g_f(E, m)$ for each grating on a fine energy scale.

The basic X-GEF test configuration is shown in Figure 4.5. The source of X-rays is an electron-impact source (Manson multi-anode) which has an X-ray spectrum that is made up of a continuum plus one or more discrete lines. The incoming X-ray beam, collimated by either a slit or 1-D optic, illuminates a grating. X-rays emerge from the grating into various diffraction orders and are detected by a position sensitive proportional counter, PSPC, which has a spatial range of +/- 60 mm. The goal of the measurement is to measure the fraction of the incoming beam (at the line energy) that is diffracted into the combined first-orders of the grating.

Because of the presence of continuum and other lines in the source and the poor energy resolution of the PSPC, there are many error sources that can foil a straight-forward measurement of the efficiency based only on with-grating/with-out-grating PSPC measurements. To avoid these pitfalls we have installed in X-GEF two gratings which serve as efficiency references, Section 3.2.5. During flight testing, measurements are also taken with the reference grating in the beam. The ratio of grating-under-test diffracted count rate to reference-grating diffracted count rate can then be made directly and with a much reduced sensitivity to systematic errors. In this way the known reference-grating efficiencies are transferred to the grating-under-test efficiencies.

Two gratings are tested in each unattended overnight X-GEF run. The $\approx$ 300 Mb of data collected are written to two DAT tapes (one stays at MIT and one goes to the ASC.) Figure 4.6 shows an example of the results of X-GEF data analysis[18] for an MEG grating. The measured plus and minus first order efficiencies at five energies (Cu L 0.930 keV, Mg K 1.254 keV, Al K 1.486 keV, Mo L 2.293 keV, and Ti K at 4.511 keV) are shown along with a model fit which uses a 5-vertex bar shape, Figure 4.8. For HEGs a measurement is additionally made at Fe K 6.400 keV, Figures 4.7 and 4.9.

These X-GEF model parameters and resulting model fits are the laboratory measure of $g_f(E, m)$ of Equation 1.4.

To-do:
Need a .ps version of the X-GEF schematic.
Add more details about the different regions tested.
Update X-GEF analysis and predictions when more accurate reference grating efficiencies are available.
Create table of measured asymmetry slopes for each grating-region to estimate HEG and MEG asymmetry slopes.

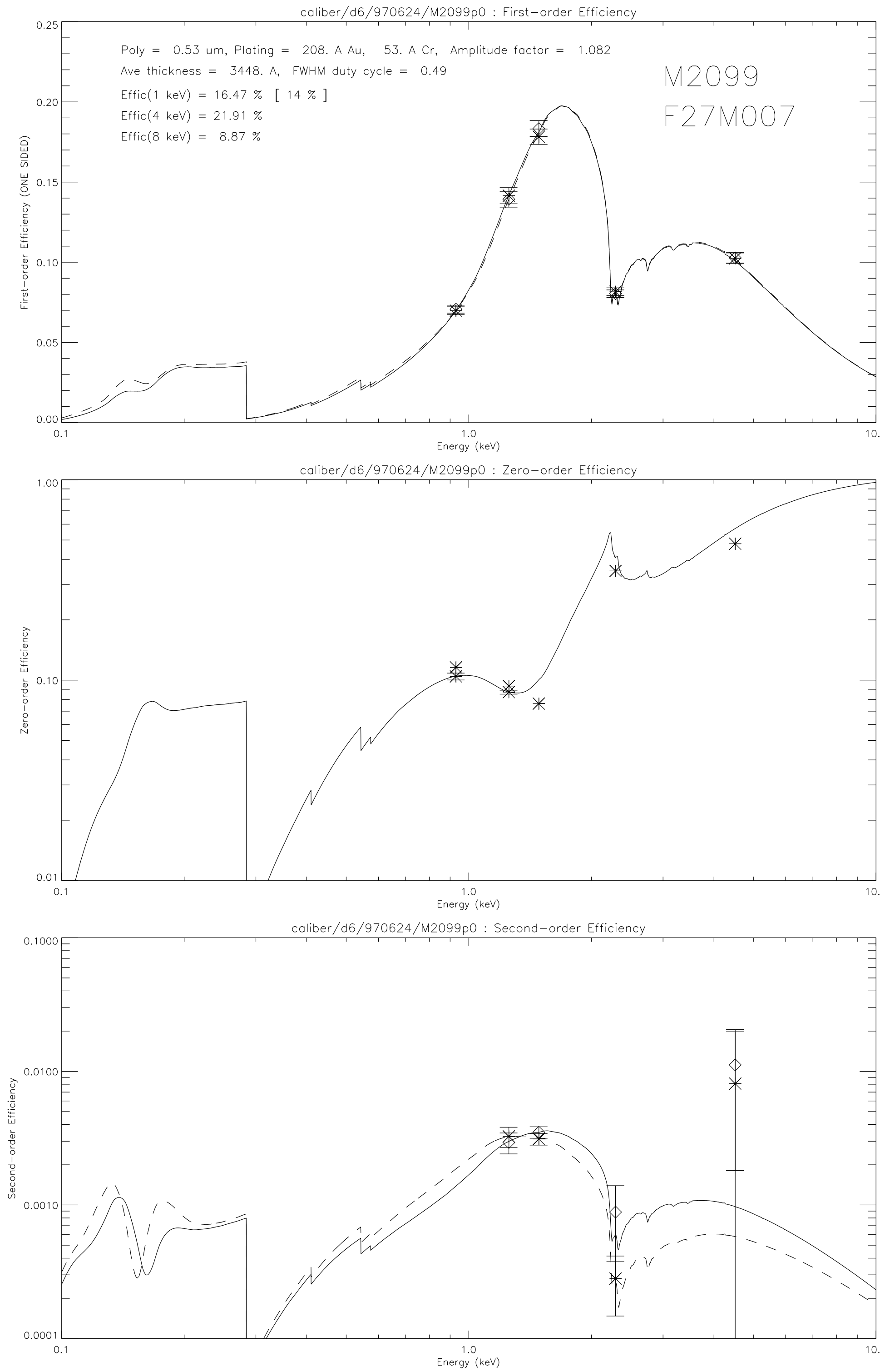

Figure 4.6: Measured and modeled first-order efficiency of the central region of MEG grating M2099. The model is simultaneously fit to +/- 1st-order, zero-order, and 2nd-order data. The interpolated combined efficiency at 1 keV of 16.47% exceeds the specification-required average of 14% .

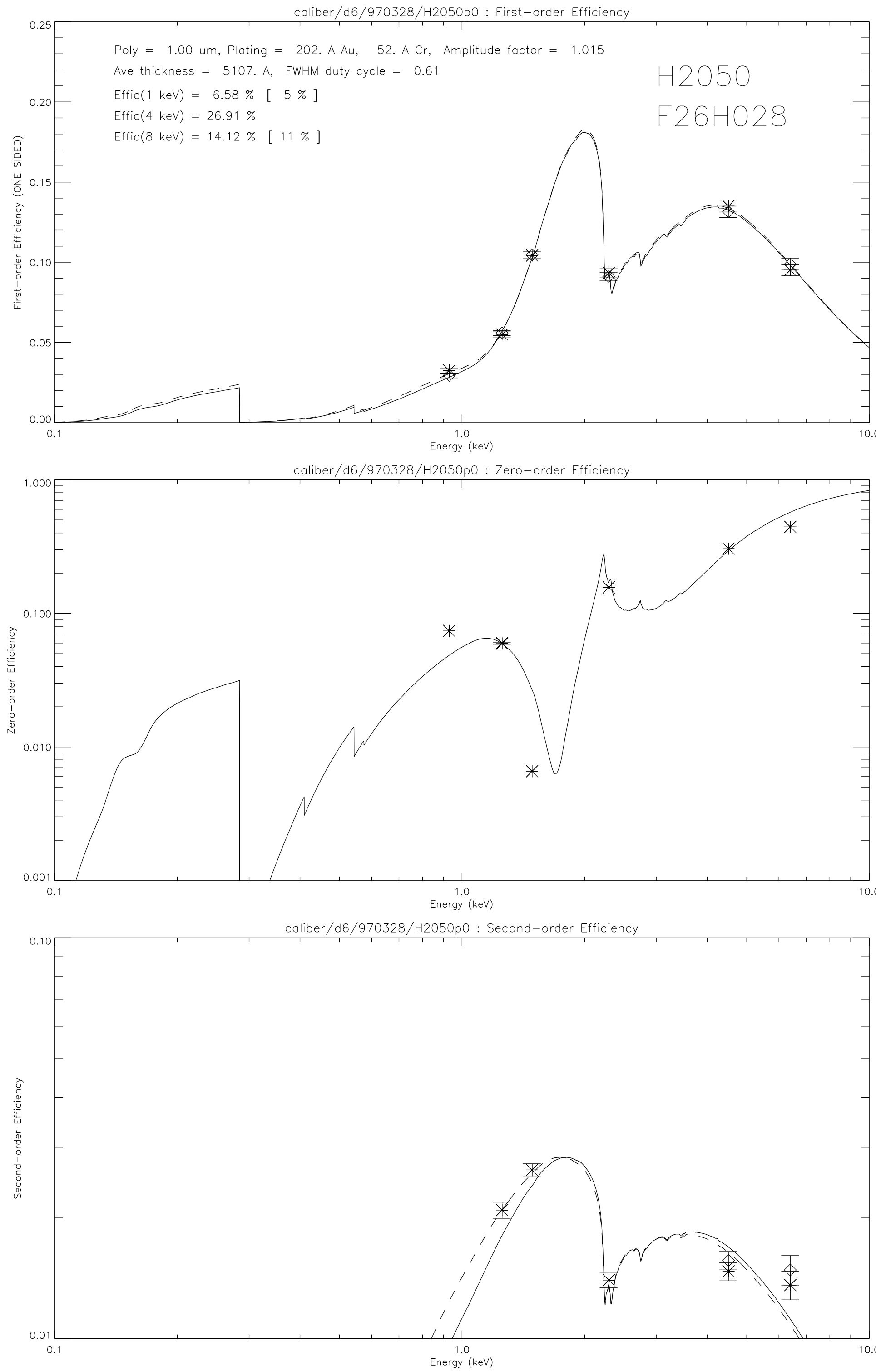

Figure 4.7: Measured and modeled first-order efficiency of the central region of HEG grating H2050. The model is simultaneously fit to +/- 1st-order, zero-order, and 2nd-order data. The interpolated combined efficiency at 8 keV of 14.1% exceeds the specification-required average of 11% .

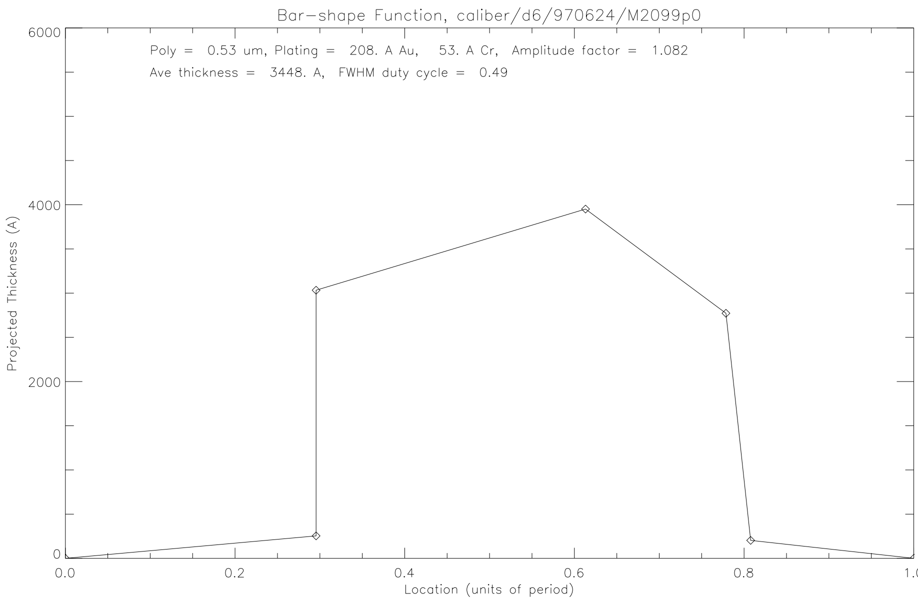

Figure 4.8: The 5-vertex bar shape used in the MEG model of Figure 4.6. The use of 5 adjustable vertices ensures a good fit of the model to the measured first-order efficiencies.

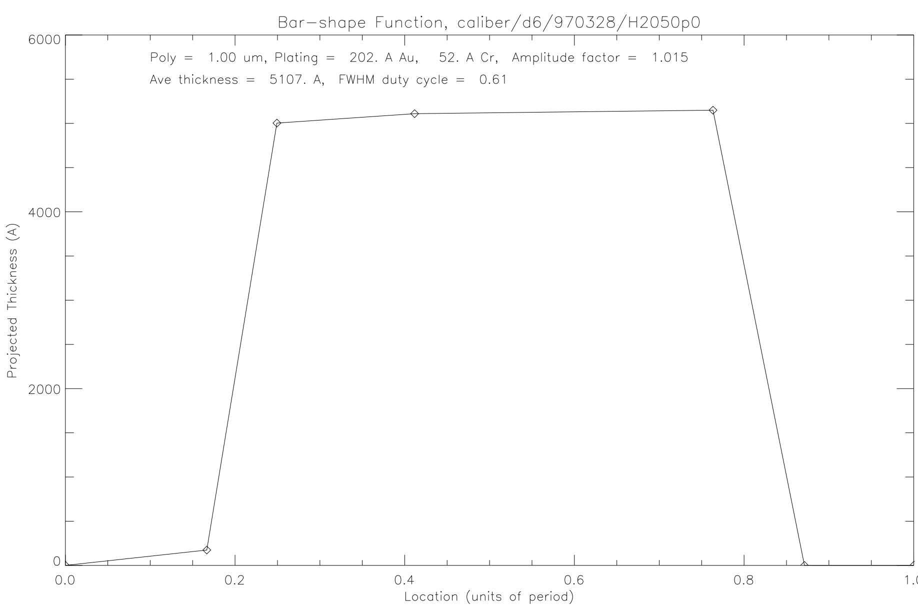

Figure 4.9: The vertex bar shape used in HEG the model of Figure 4.7. Note that the HEG shape here is thicker, wider, and more trapezoidal than the MEG example of Figure 4.8.

4.2.1 Order Assymmetry and Tilt

As expected by the diffraction theory, the trapezoidal profile of the gratings, when operated away from normal incidence, will produce an asymmetry in the intensity of the plus and minus diffracted orders. This asymmetry is measured routinely in X-GEF flight testing at the Al-K line, 1.486 keV. Figures 4.10 and 4.11 show the tilt test results for the example MEG and HEG gratings M2099 and H2050. Note the higher tilt sensitivity (steeper asymetry slope) of the HEG due to its more trapezoidal bar shape.

Because of the Rowland design of the HETG, the grating facets in use "see" X-rays arriving at normal incidence. For off-axis sources (due to multiple sources in the field or offset pointing of a desired source) the HETG may be called on to operate at angles of incidence of order 0.05 degrees (3 arc minutes or 9 mm off-axis.) Even for the HEG gratings this would result in an asymmetry of less than 2% between the plus and minus orders.

Note that the tilt curves are very linear within a degree of normal incidence (Grating Angle = 0). This means that the *total* first-order diffraction efficiency is very insensitive to small tilts. For this reason the primary efficiency calibration is the combined first-order values.

4.2.2 Laboratory Efficiency Predictions

The full set of model parameters derived from the X-GEF data are then used to create the shell-averaged efficiencies $G_s(E, m)$ for the full HETG. Coming into XRCF testing these represent out best estimate of expected HETG efficiency performance, Figures 7.4 and 7.5, and efficiency product, Section 9.3.4.

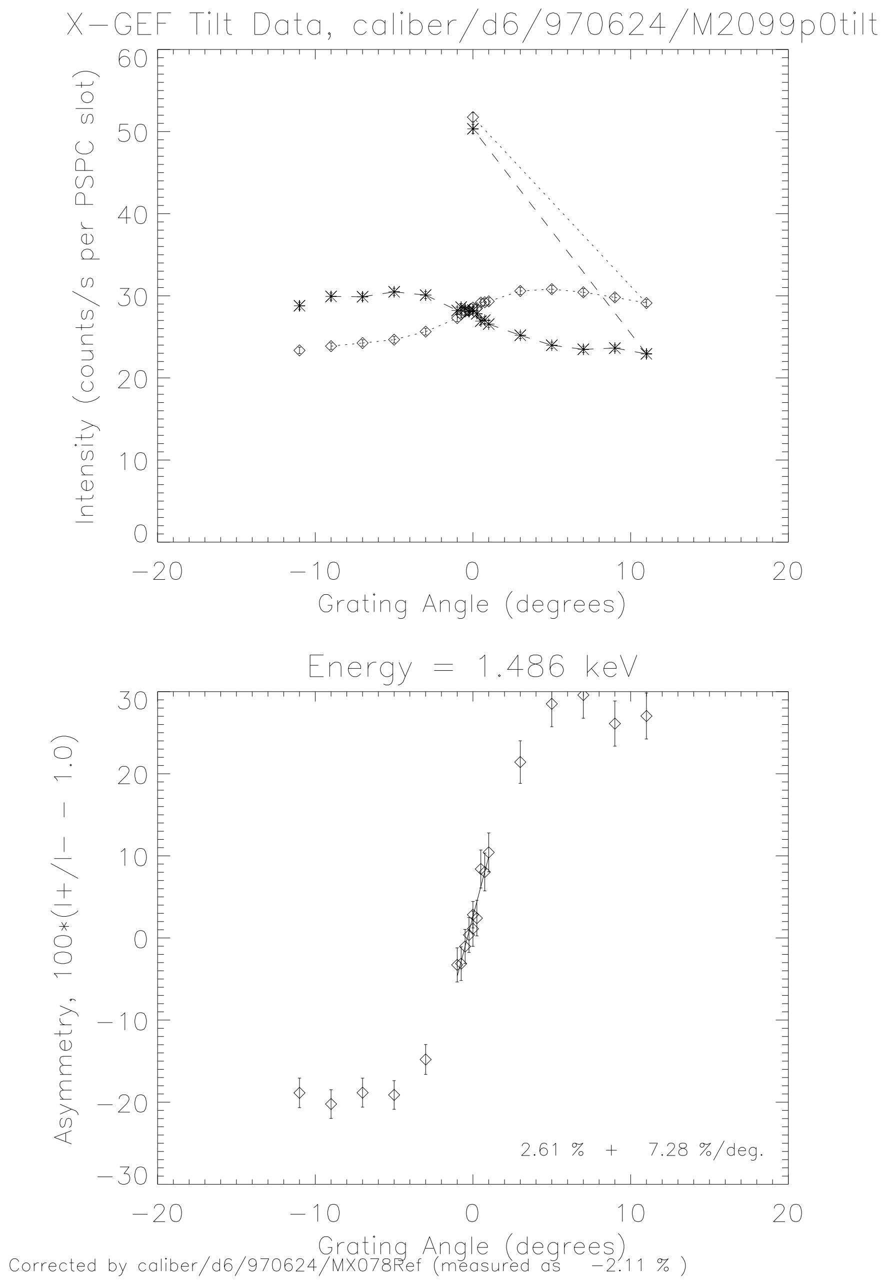

Figure 4.10: X-GEF Tilt Plots for an MEG. The top plot shows the plus and minus first-order Al-K count rates as a function of incidence angle. The bottom plot shows the "asymmetry" plotted versus angle. The normal-incidence asymmetry is only 2.6% with a slope of 7.3% per degree.

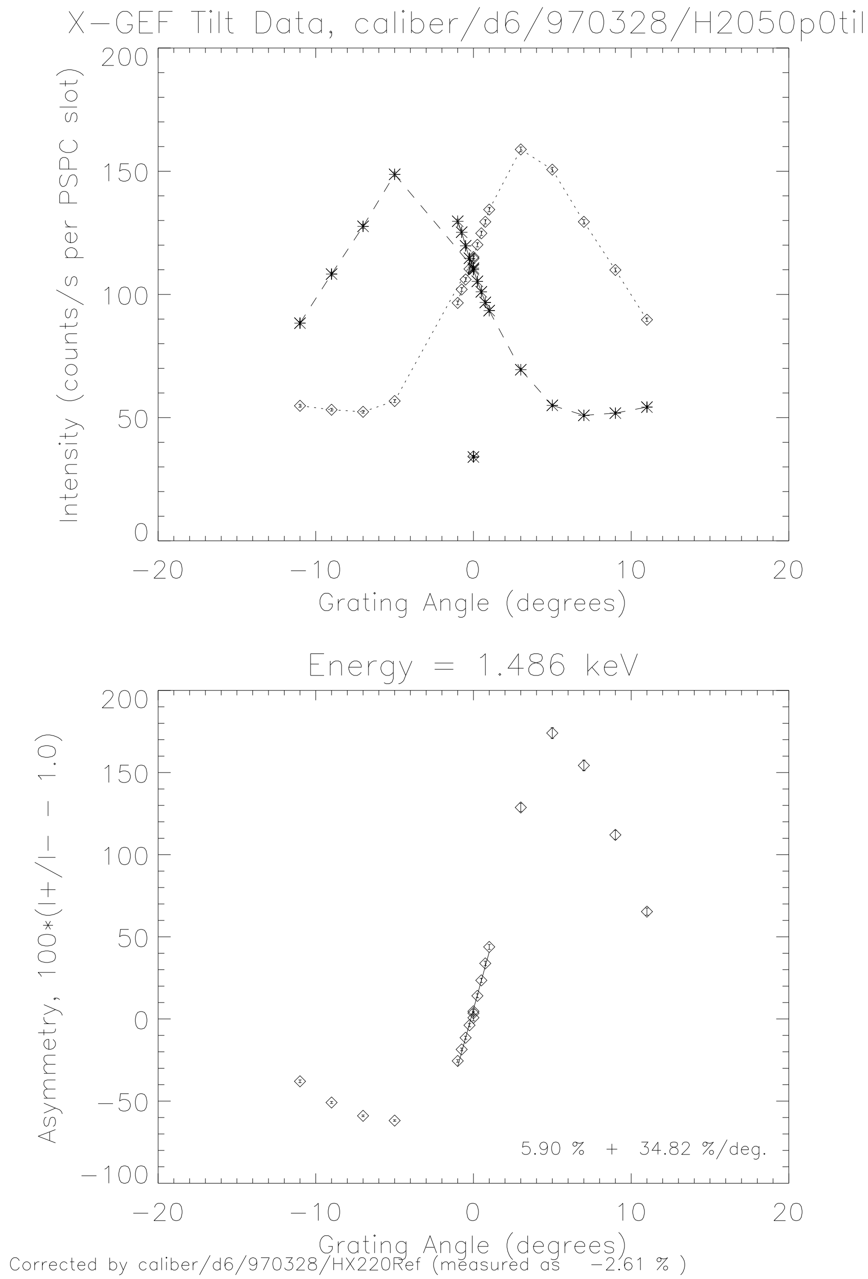

Figure 4.11: X-GEF Tilt Plots for an HEG. The top plot shows the plus and minus first-order Al-K count rates as a function of incidence angle. The bottom plot shows the "asymmetry" plotted versus angle. The normal-incidence asymmetry is 5.9% with a slope of almost 35% per degree. This strong asymmetry with angle is the result of the trapezoidal shape of the grating bar, Figure 4.9.

4.3 Alignment Measurements

The facet-to-facet alignment variations were measured as part of the facet installation procedure; the roll angle of each facet with respect to a reference facet was measured in the HETG Alignment Facility based on the polarization alignment technique of Anderson *et al.*[2]. The total roll variation of the facets is measured with the polarization technique to be well below our design specification of 1.1 arc minutes rms, Figure 4.12.

> *To-do*: Describe the measurements regarding polyimide effects on the polarization-measured angle.

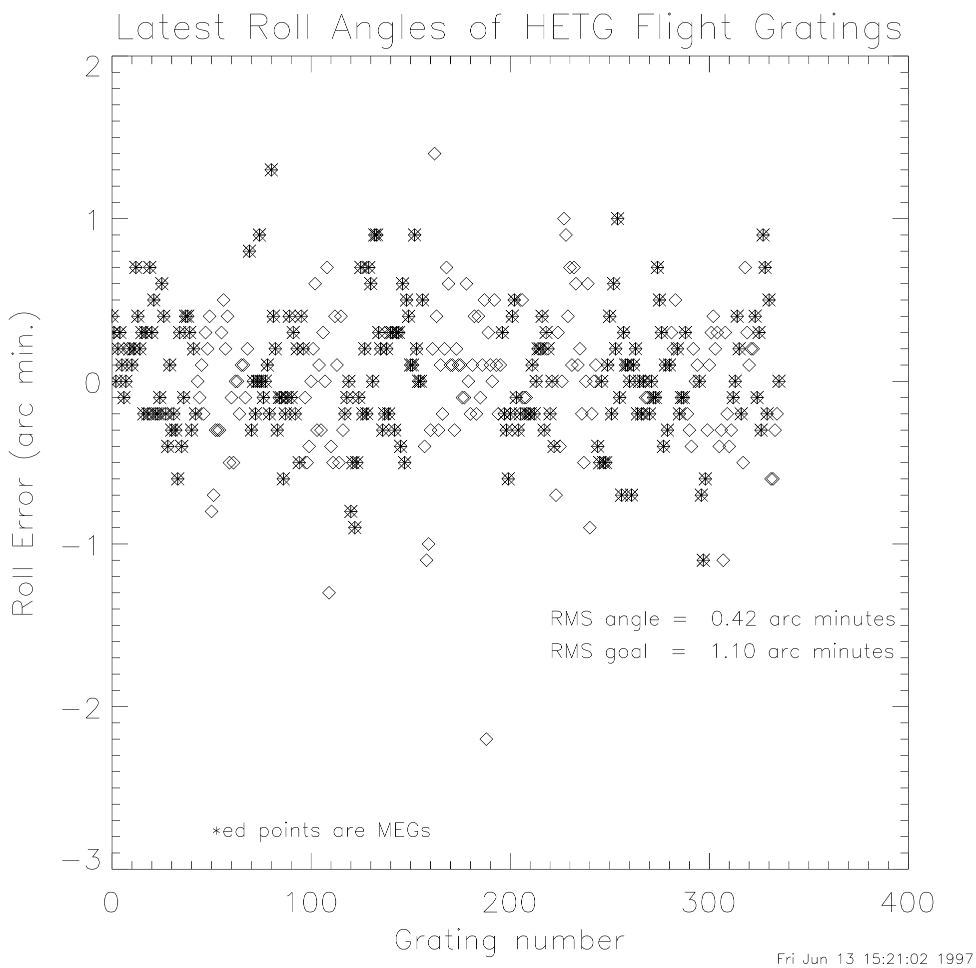

Figure 4.12: Measured roll errors for the 336 flight gratings. The rms value $\gamma = 0.42$ arc minutes is well below the specification of 1.1 arc minutes.

4.4 Long-term: Vacuum Storage Gratings

To-do: Describe the on-going vacuum storage program and summarize any measurement trends.

Sample gratings from the HETG flight fabrication batches have been retained at MIT. These gratings are stored in a vacuum system and periodically measured in the LR and X-GEF setups with flight procedures. This monitoring should allow us to set limits on any "aging" effects of the flight gratings.

Part II

X-Ray Calibration Facility Measurements and Analysis

Section 5

XRCF and the HETG

5.1 XRCF Introduction

During December 1996 through April 1997 all three key components of the HETGS, HRMA-HETG-ACIS-S, were integrated for test at NASA's Marshall Space Flight Center (MSFC) in their X-Ray Calibration Facility (XRCF). The XRCF and related hardware are described in great depth in the documents listed in Table 5.1, however some key concepts are presented here for completeness and to support the grating analysis discussion.

Table 5.1: XRCF Documents and References

XRCF Phase 1 Testing: Preliminary Results	MST	June 1997

The general layout of XRCF hardware is shown in Figure 5.1 and specifics of the key subsystems are presented below.

Calibration was divided into two main calibration phases, Phase I and Phase II, defined physically by differences in the focal plane detectors; the Beam normalization detectors (BND) were present in both Phases. Each of these major phases had subphases designated sequentially by letter, see Table 5.2.

Table 5.2: XRCF Phases and Detectors

Phase	Focal Plane	Comments
R	FPC, SSD, HSI	TMA and TOGA
I-C	FPC, SSD, HSI	
I-D	FPC, SSD, HSI	
I-E	FPC, SSD, HSI	
II-F	ACIS-2C	
II-G	HRC and '2C	
II-H	ACIS	
II-I	ACIS	Flat fields, no HRMA
J	FPC, SSD, HSI	HXDS detector cross-calibrations

In Phase I the non-flight detectors, FPC_X2 (Flow Proportional Counter), SSD_X (Solid State Detector), and HSI (micro-channel plate High Speed Imager), were in the focal plane. The philosophy of Phase I is that the detectors are (or will be) well characterized and of proven and understood technology so that measurements are performed to understand the HRMA and gratings. Grating-in grating-out measurements were performed to measure grating Efficiency; images and scans were obtained to verify the grating LRF model.

In Phase II a "two-chip ACIS" (ACIS-2C) and the flight ACIS and HRC detectors were variously present. Here the philosophy is that the HRMA and gratings are understood and the flight detectors and/or the HRMA-(grating-)detector interaction is being studied. For this reason, the HETG tests were primarily related to Effective Area. Because LRF tests generally require well focussed beams and given the HRC pore extraction limits and the ACIS telemetry limits, extensive LRF studies were not in general carried out with the HETG in Phase II – the exception being enough data with ACIS-S to allow us to verify the Rowland curvature of the CCDs.

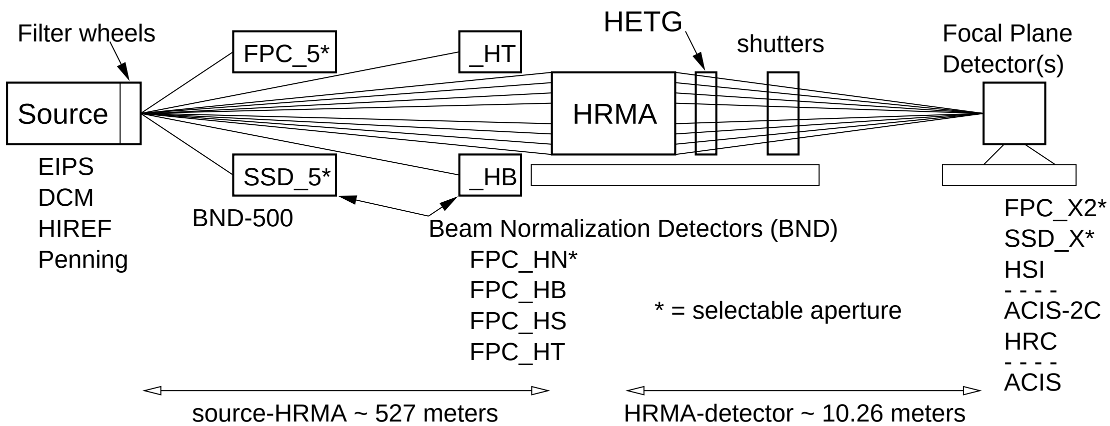

Figure 5.1: XRCF hardware schematic. The XRCF HETG configurations include i) X-ray source and filters, ii) Beam normalization detectors (BNDs), iii) AXAF optics (HRMA, HETG), iv) shutter assembly, and v) focal plane detectors.

5.1.1 XSS

5.1.2 BNDs

The beam normalization detectors (BNDs) monitor the source flux without the effects of the HRMA or HETG. There are six BND detectors: two, a Flow Proportional Counter (FPC) and a Ge solid state detector (SSD), are located 37.7 meters from the source in "Building 500", and four FPCs surround the HRMA entrance. To ensure some BND data is available over a wide range of source flux, apertures can be selected on the FPC_5, SSD_5, and FPC_HN BNDs.

5.1.3 HRMA, Gratings, and Shutters

Some useful XRCF HETG parameters are tabulated in Table 5.3 for reference. Note that the Rowland spacing for the HETG is still uncertain, Section 5.2.1.

Table 5.3: Table of useful XRCF HETG parameters. These preliminary values are based on sub-assembly and XRCF testing.

Description	value	error	units	comments
Rowland distance	8782.8	0.5	mm	based on XRCF drawings
MEG average period	4001.41	≈ 0.10	Å	based on lab measurement
HEG average period	2000.81	≈ 0.05	Å	LR/NIST: based on lab measurement
MEG angle	4.74	0.05	deg.s	
HEG angle	-5.19	0.05	deg.s	
MEG-HEG angle	9.93	0.01	deg.s	

5.1.4 HXDS Focal Plane System

In Phase I the non-flight detectors, FPC_X2 (Flow Proportional Counter), SSD_X (Solid State Detector), and HSI (micro-channel plate High Speed Imager), were in the focal plane.

5.1.4.1 HXDS translations

5.1.4.2 HSI in the Focal Plane

During Phase I calibration the HSI detector[15] provided imaging capability at high event rates, for example the image in Figure 1.4. The HSI also was fitted with a mask with a "cusp" to allow the bright PSF core to be occulted while the surrounding wings of the PSF were observed.

5.1.5 FPC and SSD in the Focal Plane

The FPC and SSD are non-imaging detectors with moderate energy resolution and have a variety of apertures used to isolate and measure grating-dispersed spectral features in the focal plane. These detectors have well studied characteristics[46], are similar to the BNDs, and provide some of the fundamental data for characterizing the efficiencies and effective area of the system without the complication of the flight-detector $QE(E, \ldots)$ terms.

The FPC and SSD detectors[46] could have a slit aperture selected for use - in this way a direct measurement of the 1D LRF was possible.

5.1.6 ACIS-2C

Extensive LRF tests could be performed with the ACIS-2C detector given its (non-flight) high event-rate readout.

5.1.7 ACIS

5.1.8 HRC

5.2 Differences between XRCF and Flight

The arrangement and operation of the components at XRCF are flight-like with the following differences:

◦ The source is not infinitely far away and so i) the HRMA focal length is greater than the flight value and ii) the HRMA reflection angles and optic illumination are different from flight.
◦ The HRMA is in a "1-g off-loaded" condition approximating the 0-g flight configuration, so flight PSFs will be slightly different.
◦ The $+Z$ axis of the HRMA, gratings, and flight detectors pointed "down" at XRCF, (*i.e.*, aligned to XRCF $-Z$).
◦ The gratings are designed to operate at a Rowland distance of 8633.69 mm but because of the HRMA focal length change they are placed $\approx$ 8800 mm from the focus; this introduces negligible LRF effects and some slight additional vignetting, primarily for the LETG ($< 5\%$).

5.2.1 HETG Location at XRCF

The Rowland spacing of the grating is the on-axis Rowland circle intercept to focal plane distance. This spacing must be inferred from measurements between the HETG and HRMA as well as assumed/measured location of the HRMA focus w.r.t. the HRMA fiducial location, *e.g.*, CAP center line. The following equation gives the Rowland spacing in terms of other measurable values:

$$\text{(RC spacing)} = \text{(Focus to CAP CL)} - \text{(CAP CL to OTGorg)} + \text{(OTGorg to RC)} \quad (5.1)$$

Values for these quantities are tabulated, Table 5.2.1, for three cases: i) XRCF design drawings, ii) drawings plus a shim designed to improve the vignetting performance of the gratings, and iii) values inferred from HRMA ARM to OTG ARM laser ranger measurements. The later of these is TRW's best value for the spacing and was used in the "period, angle, spacing" analysis of Section 6.2. Using the 8788.0 mm value for spacing, the XRCF derived periods of the HEG and MEG gratings are both too high by $\approx$500 ppm. This conspiracy suggests that the HETG spacing is not 8788.0 but closer to the "design plus shim" value of 8782.8 mm.

RC spacing		Focus to CAP CL	CAP CL to OTGorg	OTGorg to RC
mm	inches	inches	inches	inches
		Drawing 301331:		
8772.8 mm	345.387	403.5	60.613	2.5
		Drawing 301331 with 0.392 shim:		
8782.8 mm	345.779	403.5	60.221	2.5
		Measurements with laser ranger:		
8788.0 mm	345.986	403.512	60.026	2.5

To-do:
Create a diagram of the spacing distances, references, etc.
Track down th HETG location error
Add discussion of vignetting due to XRCF positioning.

5.2.2 HETG Orientation at XRCF

The drawing of Figure 1.3 **when turned upside down** shows the HETG as oriented at XRCF. The view will then be from the HRMA towards the HETG with the +Z_facility (Up) at the top of the (flipped) page and +Y_facility (South) is to the right. This orientation is rotated 180 degrees about X from the Lab and Flight orientations.

Grating facet locations are given by a code such as 6EE3 where:

> The leading digit is the shell number (1,3,4,6).
>
> The next one or two letters specify the sector
> (designated A, B,..., F, AA, BB,..., FF).
> For the **XRCF orientation**:
>
> > sector A is between 9 and 8 o'clock
> > sector B is between 8 and 7 o'clock
> > ...
> > sector F is between 4 and 3 o'clock
> > sector AA is between 3 and 2 o'clock
> > sector BB is between 2 and 1 o'clock
> > ...
> > sector FF is between 10 and 9 o'clock.
>
> The final number gives the grating location within
> the sector (numbered 1,2,... increasing in CCW direction,
> *i.e.*, grating 1 is the most clockwise in a given sector.)

When used with the XRCF shutters the following HETG sectors are illuminated:

Shutter	Illuminated Sectors
Top	BB high-numbered half, CC, DD, EE low-numbered half
North	EE high-numbered half, FF, A, B low-numbered half
Bottom	B high-numbered half, C, D, E low-numbered half
South	E high-numbered half, F, AA, BB low-numbered half

5.3 Summary of HETG XRCF Measurements

To support semi-automated test operation, the measurements to be made at XRCF were specified as rows in a 92 column tab-delimited ASCII file. These 92 columns specified nearly completely the desired state of the source, filters, HRMA, gratings, shutters, normalization detectors, and focal plane detectors. Testing proceeded through sequentially "executing" lines of this Calibration Measurement Data Base (CMDB). An as-run (or at least "as-requested"—modifications could be made manually in real time) version of the CMDB is now a useful starting point in understanding what data were taken.

The measurements (lines or rows of the CMDB) were assigned a "measurement type" which both specified a general focal plane hardware operating mode (Phase I in particular) and indicated the scientific purpose of the measurement. Tables 5.4 and 5.5 provide a summary of all data taken at XRCF with the HETG inserted in the optical path and an indication of their use and data volume (number of measurements in brackets.) These tables with hyper-links to CMDB summaries are available on the web at:

`http://space.mit.edu/HETG/mtab/meas_table.html`

5.3.1 Efficiency Measurements

The measurement types related to effective area break into two main divisions: *i*) quasi-monochromatic measurements: types EE (encircled energy), EA (effective area), and 3D(an automated version of EA); and *ii*) "Molecular Contamination" (MC) measurements where the broad-band continuum produced by the source is utilized (see the MC example in Section 7.3).

The distinctions between EE, 3D(EA), and EA are primarily in Phase I and represent different methods of placing the focal plane hardware at the desired location: in EE a "beam-center" is performed to set the aperture(s) relative to the reference location specified in the CMDB; in 3D(EA) measurements, one or more locations are sampled in the focal plane at coordinates specified by a locations file; and in EA the location is specified in the CMDB.

A valuable fraction of the data were taken while one of the XRCF monochromators was scanned in energy. Although scientifically similar to non-scanned data, these data are more difficult to analyze because there was no direct synchronization between the source scan and the data collection. These all have measurement type EA.

Finally, the "Alignement" test was originally designed to set limits on vignetting due to (unplanned) decentering of the HETG at XRCF. Because of the MEG misaligned gratings, the alignment test performed on high order became a tool for LRF diagnosis.

5.3.2 LRF Measurements

Phase I LRF measurements were performed with the HSI generally and with the FPC fitted with slits with a Mg-K source ("PSF/1-D").

In Phase II, the ACIS-2C was used extensively for PSF/Inner tests.

To-do:
description of TRW ID fields
IDL CMDB s/w description
Apendix with CMDB summary for each of the measurement types (or put these in respective analysis sections.)

Table 5.4: Summary of HETG XRCF Measurements in Phase I. Number of measurements is shown in brackets.

Type	Detector	
	FPC/SSD	HSI
LRF-related ...		
FC and SF	-	Verify focus, check PSF [16]
dFocus	-	Defocus and in-focus images [2]
Alignment	-	Gross vignetting, mis-aligned gratings [3]
PSF/1D	LRF core, wings [21]	-
PSF/Outer	-	Wings, scatter [8]
3D (Offaxis)	-	Offaxis images [6]
Eff.area-related ...		
EE	Order locations, effective area [33]	-
3D (EA)	Effective area, high orders [56]	Source spectra, MEG-Penning PSF [32]
EA (fixed E)	Effective area [10]	Source spectra (incl. DCM, HIREF) [9]
EA (mono scan)	Effective area [19]	-
3D (Molecular Contamination)	-	Identify and search for edges, etc. [6]

Table 5.5: Summary of HETG XRCF Measurements in Phase II. Number of measurements is shown in brackets.

Type	Detector		
	ACIS-2C	HRC	ACIS
LRF-related ...			
FC and SF	Verify/check focus [7]	Verify/check focus [1]	-
dFocus	Find best focus [10]	-	-
PSF/Inner	Core, wings; offaxis images [23]	-	Core, wings; offaxis images [8]
Scattering	Wings, scatter [5]	-	Grating scatter, pileup effects, readout modes (, eff. area) [7]
Eff.area-related ...			
EA (fixed E)	Effective area [133]	Effective area [33]	Effective area [11]
EA (mono scan)	Effective area [29]	Effective area [1]	Effective area [9]
MC (Molecular Contamination)	Identify and search for edges, etc. [53]	-	Identify and search for edges, etc. [5]

5.4 Examples of XRCF Data

With complicated data it is best to start with an image—and so in Phase I we generally took images of the diffracted X-rays with the High Speed Imager (HSI). Figure 5.2 shows the HSI image of the Al-K line in the MEG 3rd order—deflected 55 mm from the zero-order (HRMA focus) location. These are the "raw" HSI data and show the instrumental "gaps"[15], *e.g.*, one goes through the K-β peak. Note that the "line" in fact consists of several discrete lines as well as continuum. The "satellite" line just shortward of the K-α peak has been previously observed during XMM grating testing[38]; we also observe a second, weaker satellite line at 8.22Å.

To accurately measure the intensity of the line in Phase I, the FPC_X2 (or SSD_X) with selected aperture could be moved to the line center and the pulse-height histogram of events through the aperture measured. An example of the acquired focal-plane and BND histograms is shown in Figure 5.3 for the MEG first order of Al-K and a 500 μm diameter aperture. Note that while the BNDs are able to resolve an Al-K peak and broadband continuum, the detailed spectral structure of the Al-K line is unresolved. The 500 μm first-order aperture size corresponds spectrally to the region within the 1500 μm circle shown in Figure 5.2—thus the FPC_X2 is detecting the K-α and satellite lines and some continuum, but is excluding other continuun and the K-β peak.

In Phase II the focal plane detectors were all imaging instruments (ACIS-2C, ACIS, and HRC) and so provide their own source spectral diagnostics. Effective area measurements generally did not required precise positioning; in fact, because of per-pixel count-rate limits (set generally by pile-up for ACIS and dose limits for HRC) the measurements were performed with a large defocus. Figure 5.4 shows an ACIS-2C image of the HEG first-order of Al-K. The defocussed images of the HRMA shells 4 and 6 are modulated by the individual grating facets. Because of the defocus, extraction of the K-α events will necessarily be contaminated by the existence of the other lines and continuum. HRC and ACIS effective area data are very similar to this ACIS-2C example as the ACIS-S event plot of Figure 5.5 demonstrates.

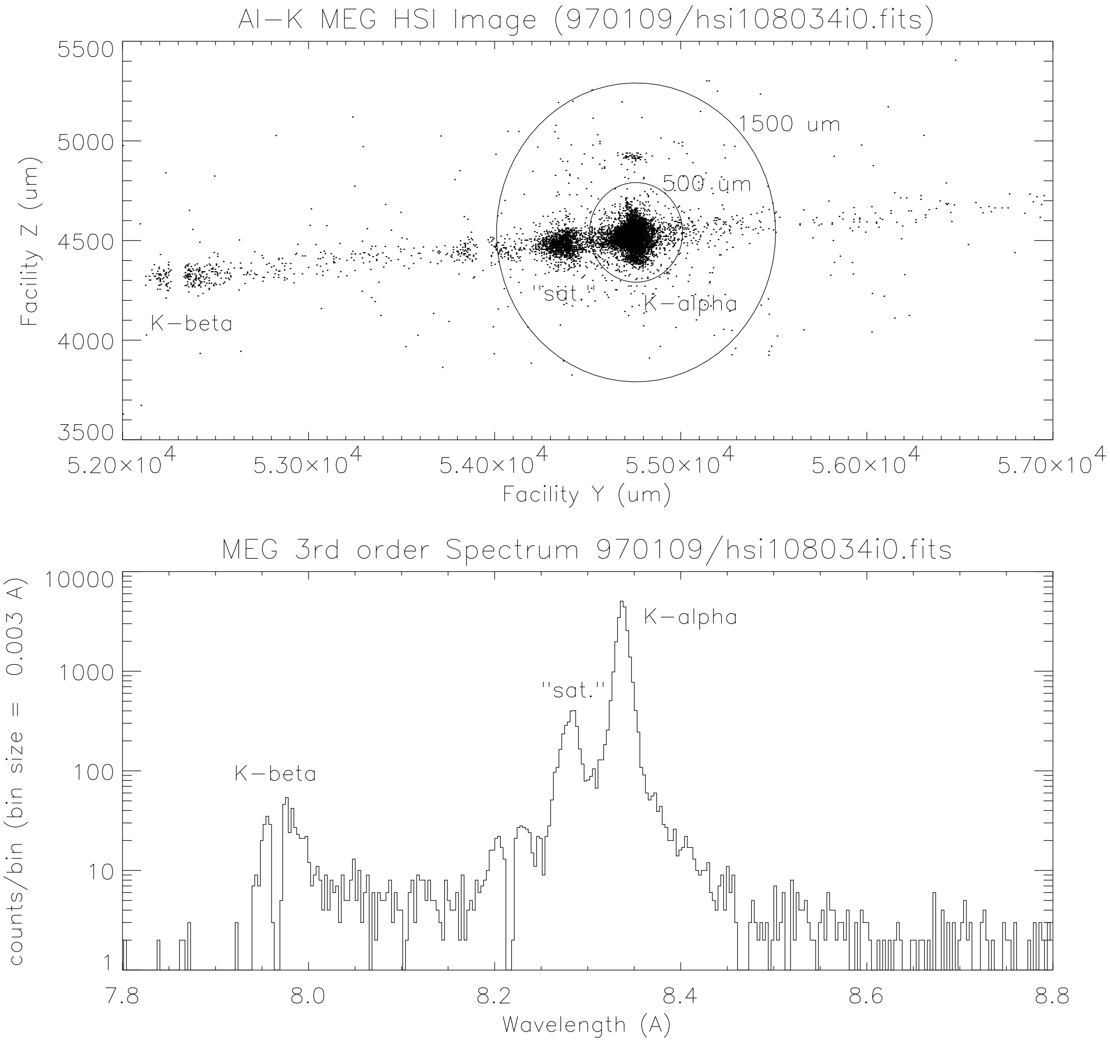

Figure 5.2: HSI image of 3rd-order MEG Al-K line (top) and the resulting grating-produced spectrum (bottom). Note that all of this spectral structure is unresolved by the FPC and SSD detectors, Figure 5.3. A strong "satellite" line is clearly visible near the K-α peak. HSI instrumental gaps have not been removed, *e.g.*, at the K-β line.

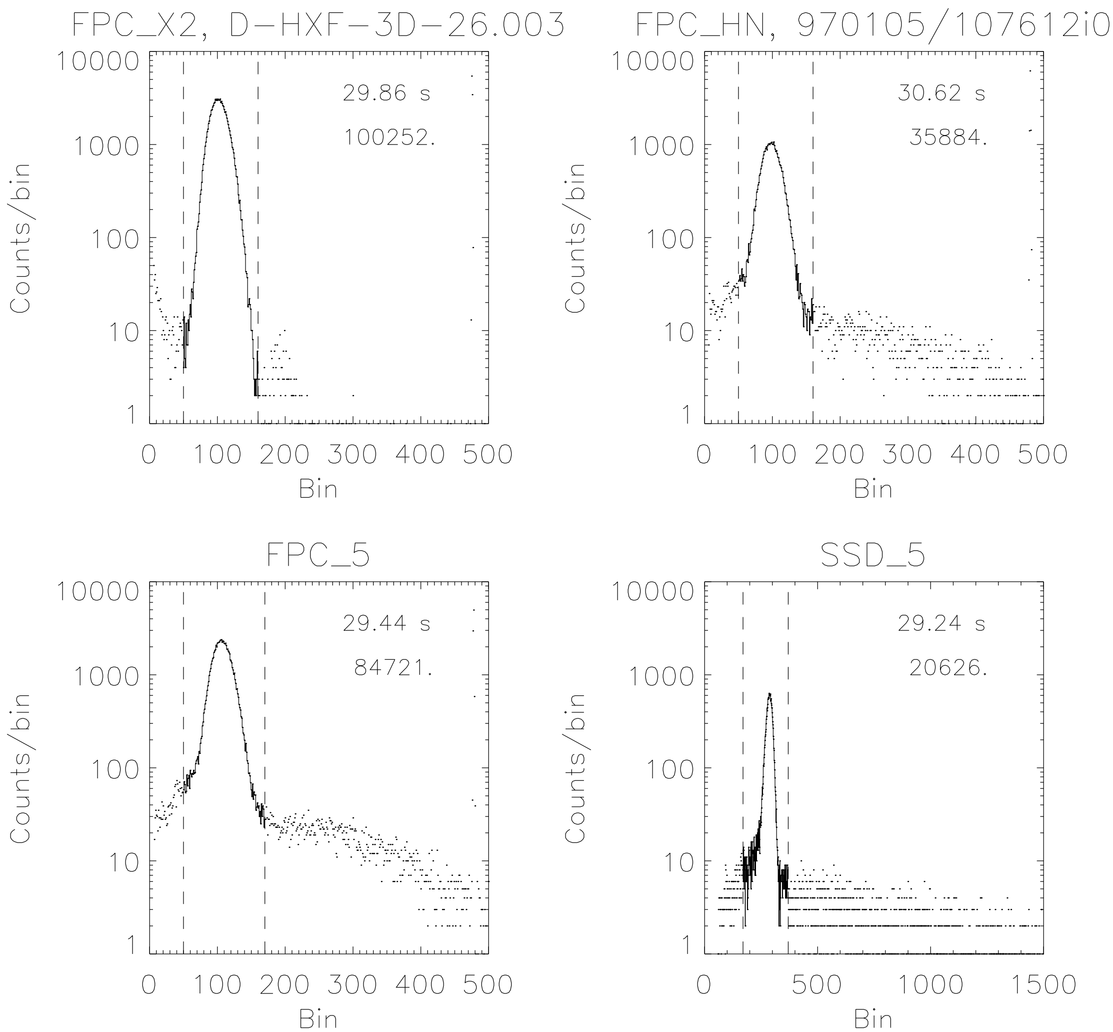

Figure 5.3: PHA spectra from Al-K MEG +1 order measurement. The focal plane FPC_X2 shows only a monochromatic response (with a slight pile-up peak at $2E$) while the beam normalization detectors (FPC_HN, FPC_5, and SSD_5) show both the Al-K "line" and broad-band (unfiltered) continuum.

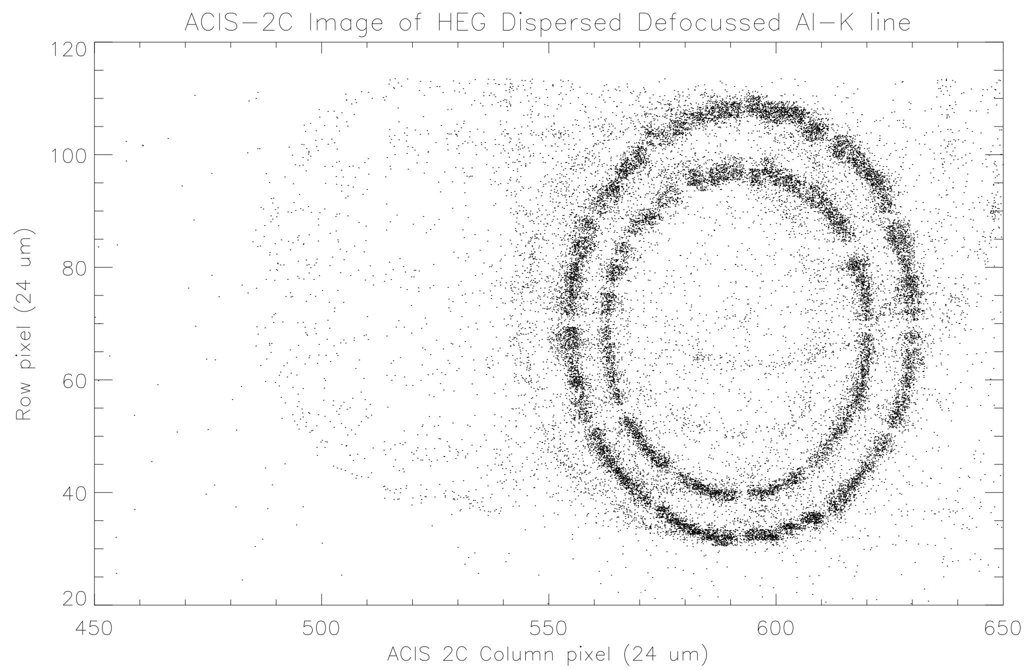

Figure 5.4: ACIS-2C defocussed image of HEG dispersed Al-K line. Note that the same line components as in Figure 5.2 are present.

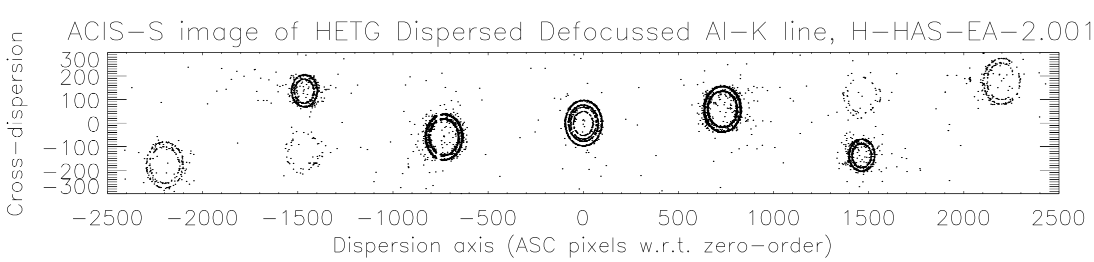

Figure 5.5: ACIS-S defocussed image of HETG dispersed Al-K line. The HEG and MEG diffracted orders are clearly identified by the corresponding HRMA shells in their images. For the MEG, orders $m = \pm1, \pm2, \pm3$ are visible.

5.5 Status of the HETG XRCF Analysis

The table below summarizes the status of the HETG XRCF analysis efforts. Only a few of the measurement projects listed here have reached the level of "adequate" analysis. Analysts are generally from the HETG and ASC/MIT groups; brackets indicate contributors expected beyond this preliminary report.

Table 5.6: Status Code

Status code	Analysis status
-	not yet analyzed
X	very preliminary analysis
XX	adequate analysis
XXX	complete analysis

Table 5.7: Status of HETG XRCF analyses

Section	Analysis Effort	Analyst(s)	Status
	LRF:		
6.2	Periods and Angles	dd	XX
6.3	Core: Period and Roll Variations	dd	x
6.4	MEG mis-aligned gratings	dd, hlm	XX
6.5	Between Core and Scatter	[dd, hlm]	-
6.6	Scatter	hlm,dd	Xx
6.7	Offaxis and Defocus	[dsd, wise]	-
6.8	ACIS Rowland Conformance	[kaf]	-
	Efficiency and Effective Area:		
7.2	Alignment Tests	dd	X
7.3	XRCF Source Characteristics	dd	Xx
7.4	Phase 1, Fixed Energies	dd	Xx
7.5	ACIS-2C Data	dd	x
7.6	Phase 1, Monochromator Scans	[dd]	-
7.7	Phase 2, Order Ratios	prp, [kaf]	x
7.8	Molecular Contamination	dd, [hlm]	X
7.9	Area with ACIS-S	[jhk, nss]	-
7.10	Area with HRC-I	[kaf]	-

Section 6

XRCF LRF Measurements

6.1 Overview

6.2 Periods and Angles

Objective: The Period and Angle analysis is used to determine the dispersion directions (angles) and a measure of the grating periods based on the dispersion distance of known narrow lines.

6.2.1 Analysis Method

At XRCF Encircled Energy measurements of the diffracted orders were performed with HXDS Beam Centering in order to precisely locate the diffracted images. The available EE data sets are listed in Table 6.1.

The beam centers obtained from these measurements are put into data files, `beam_cen_yymmdd.rdb`. The centers are reported in HXDS coordinates (`ypos, zpos` as in the .sum files) in microns, Figure 6.1. Each of these data files is analyzed with `xrcf_beam_cen_werr.pro` to get a best-fit period and angle (with errors) for each grating, Figure 6.2. The results are put, along with sub-assembly predicted values, into a results file, `beam_cen_results.rdb`, Figure 6.3.

For these analyses the following parameter values were assumed: Rowland distance = 8788.04 mm, hc = 12.3985, Al-K is at 1.4867 keV, and TOGA rowland distance = 5366.55 mm.

The Period and Angle contents of this results file are plotted using `beam_cen_plots.pro` and shown in Figures 6.4 and 6.5. The weighted-average period for each grating based *only* on the XRCF Al-K data sets is shown in the plot titles. The HETG opening angle and the HETG mean angle (MEG HEG bisector) are also calculated and plotted.

Phase	Date code	Line	Orders	TRW IDs (runids)
R	960827	Al-K	MEG -1,0,+1	102931, 102926, 102929
			HEG -1,0,+1	102938, 102933, 102935
1C	961223	Al-K	MEG 0,+1,-1	C-HXF-EE-3.003,4,10
			HEG 0,+1,-1,0	C-HXF-EE-3.005,6,13,5a
1D	970104	Al-K	MEG 0,+1,-1,-3,+3	D-HXF-EE-3.004,5,6,12,13
			HEG 0,+1,-1,-2,+2	D-HXF-EE-3.007,8,9,14,15
1D	970116	Mg-K	MEG 0,+1,-1	D-HXF-EE-3.021,22,23
			HEG 0,+1,-1	D-HXF-EE-3.024,25,26
1E	970208	Al-K	HEG 0,-2,+2	E-HXF-EE-3.007,14,15
			MEG -3,+3	E-HXF-EE-3.007,14,15

Table 6.1: Beam Center Measurements of Diffracted Order Locations

6.2.2 Results

Both the MEG and HEG periods agree much better with the Rowland spacing value derived from design plus shim of 8782.8 mm. Yet the LETG period agrees well with the 8788.0 mm value. The working hypothesis is that there is an HETG-LETG spacing difference that is not yet uncovered.

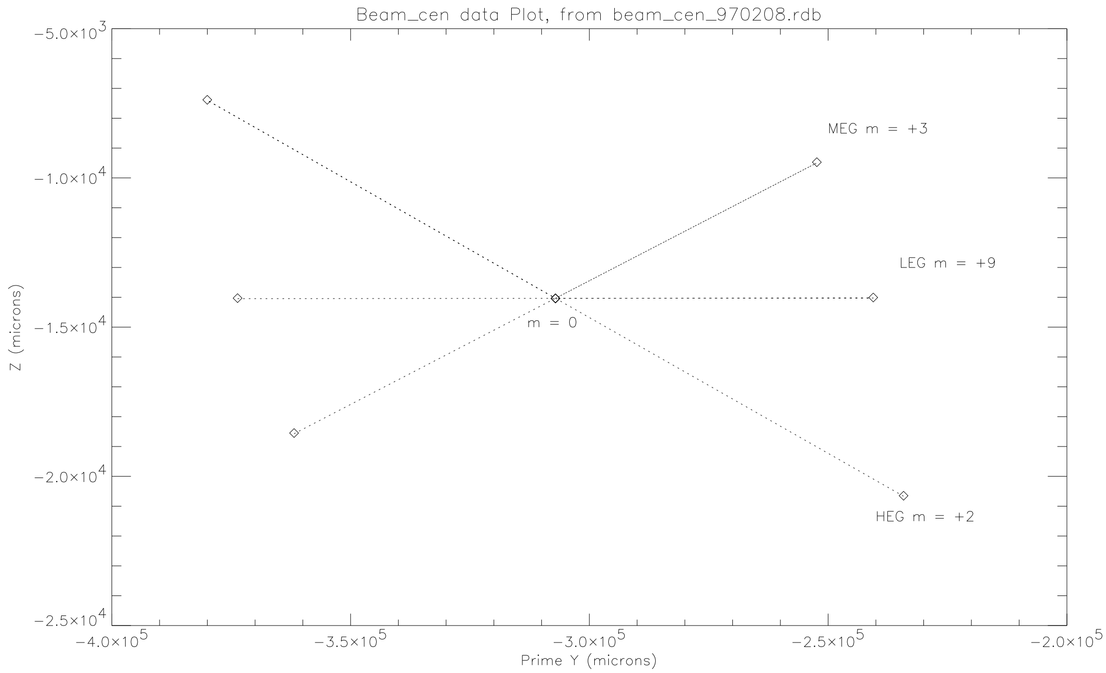

Figure 6.1: Beam center example plot

To-do:

- Improve analysis of EE data
  - Add mst_date and run_id values to 961223 and 970104 data files.
  - Re-do full analysis: .pha files to .sum files
  - Plot .sum files, compare with expected 1D scans (simulations); defocus?
  - Better "center" location and errors using 1D simulated shapes

- (Explain the LETG / HETG difference in spacing)
- Is the TOGA MEG period difference due to old LR version used for TOGA?
- Why the HEG Al/Mg difference? (by 1 part in 4000)
- Use HSI observations for period determination too.
- Use HRC and ACIS-S data sets to determine period/angle as well.

```
Output from xrcf_beam_cen_werr.pro , Fri Sep 12 13:08:01 1997
Input data file :  beam_cen_970208.rdb

Grating Order Prime Y Z Energy Y_err(um) Z_err(um)
HEG 0.00000 -307097.00 -14035.000 1.4867001 5.00000 5.00000
HEG -2.00000 -380012.00 -7383.0000 1.4867001 20.0000 20.0000
HEG 2.00000 -234206.00 -20650.000 1.4867001 20.0000 20.0000
MEG -3.00000 -361832.00 -18549.000 1.4867001 20.0000 20.0000
MEG 3.00000 -252366.00 -9473.0000 1.4867001 20.0000 20.0000
MEG 0.00000 -307097.00 -14035.000 1.4867001 7.00000 7.00000
MEG 0.00000 -307102.00 -14037.000 1.4867001 7.00000 7.00000
LEG -9.00000 -373666.00 -14028.000 1.4867001 20.0000 20.0000
LEG 9.00000 -240552.00 -14007.000 1.4867001 20.0000 20.0000
LEG 0.00000 -307102.00 -14037.000 1.4867001 5.00000 5.00000

Calculate Angles and Periods to best-fit the data:
(keeping the Rowland distance at 8788.04 )

LEG angle = 0.0090 +/- 0.0122 [ currently = 0.0059]
LEG period = 9910.03 +/- 2.11 [ currently = 9903.90]

Errors between measured and calculated Y,Z (microns):
Y: -373666.00 - -373663.67 = -2.3
Y: -240552.00 - -240549.66 = -2.3
Y: -307102.00 - -307106.67 = 4.7
Z: -14028.000 - -14034.498 = 6.5
Z: -14007.000 - -14013.502 = 6.5
Z: -14037.000 - -14024.000 = -13.0

MEG angle = 4.7396 +/- 0.0147 [ currently = 4.7412]
MEG period = 4003.27 +/- 1.03 [ currently = 4000.77]

Errors between measured and calculated Y,Z (microns):
Y: -361832.00 - -361832.25 = 0.3
Y: -252366.00 - -252366.25 = 0.2
Y: -307097.00 - -307099.25 = 2.2
Y: -307102.00 - -307099.25 = -2.8
Z: -18549.000 - -18561.501 = 12.5
Z: -9473.0000 - -9485.4993 = 12.5
Z: -14035.000 - -14023.500 = -11.5
Z: -14037.000 - -14023.500 = -13.5

HEG angle = -5.1991 +/- 0.0110 [ currently = -5.1908]
HEG period = 2002.25 +/- 0.39 [ currently = 2000.95]

Errors between measured and calculated Y,Z (microns):
Y: -307097.00 - -307105.00 = 8.0
Y: -380012.00 - -380008.00 = -4.0
Y: -234206.00 - -234202.00 = -4.0
Z: -14035.000 - -14022.667 = -12.3
Z: -7383.0000 - -7389.1638 = 6.2
Z: -20650.000 - -20656.170 = 6.2
```

Figure 6.2: Period and angle analysis output

```
#filename:  beam_cen_results.rdb
#
# Results of the XRCF HETG/LETG beam center analyses
# are compiled here along with sub-assembly values.
#
# These results are from running the idl procedure:
# IDL> xrcf_beam_cen_werr, 'beam_cen_YYMMDD.rdb'
# where YYMMDD is the dataset date code in the table below.
#
# The LETG period is taken from the MPE web page, the
# LETG period error is 1 part in 10000 (Predehl).
#
# 7/8/97 dd
# 7/9/97 dd Added TOGA (960827) values (both sub-assembly and XRCF)
# 7/10/97 dd Changed LEG sub-assembly period error.
# 7/18/97 dd Change MEG Flight and TOGA LR-NIST values based
# on NIST "M" sample period of 400.800 nm (instead
# of 400.770 nm).  Old lines:
# sub TOGA HeNe MEG 4000.68 2.0 5.0 0.5
# sub LR-NIST HeNe MEG 4001.13 2.0 5.0 0.5
# 8/20/97 dd New values from re-analysis using 8788.04 as spacing
#
phase dataset source grating p perr ang angerr
S S S S N N N N
sub TOGA HeCd LEG 9912.36 0.99 0.0 0.5
sub TOGA HeNe MEG 4000.96 0.10 5.0 0.5
sub TOGA HeCd HEG 2001.04 0.05 -5.0 0.5
Rehears TOGA Al-K LEG 9911.27 7.76 -0.9073 0.0449
Rehears TOGA Al-K MEG 4002.75 1.27 3.9489 0.0181
Rehears TOGA Al-K HEG 2001.33 0.64 -5.9974 0.0180
sub MP E HeCd LEG 9912.16 0.99 0.0 0.5
sub LR-NIST HeNe MEG 4001.41 0.10 5.0 0.5
sub LR-NIST HeCd HEG 2000.81 0.05 -5.0 0.5
XRCF 1C 961223 Al-K LEG 9910.48 1.92 -0.0435 0.0119
XRCF 1C 961223 Al-K MEG 4003.24 0.78 4.6935 0.0221
XRCF 1C 961223 Al-K HEG 2001.98 0.19 -5.2474 0.0110
XRCF 1D 970104 Al-K LEG 9910.05 1.92 0.0062 0.0111
XRCF 1D 970104 Al-K MEG 4003.81 0.62 4.7453 0.0088
XRCF 1D 970104 Al-K HEG 2002.06 0.17 -5.1879 0.0049
XRCF 1D 970116 Mg-K LEG 9911.57 5.33 0.0087 0.0308
XRCF 1D 970116 Mg-K MEG 4003.98 1.31 4.7313 0.0186
XRCF 1D 970116 Mg-K HEG 2002.52 0.33 -5.1917 0.0093
XRCF 1E 970208 Al-K LEG 9910.03 2.11 0.0090 0.0122
XRCF 1E 970208 Al-K MEG 4003.27 1.03 4.7396 0.0147
XRCF 1E 970208 Al-K HEG 2002.25 0.39 -5.1991 0.0110
```

Figure 6.3: Beam center results file

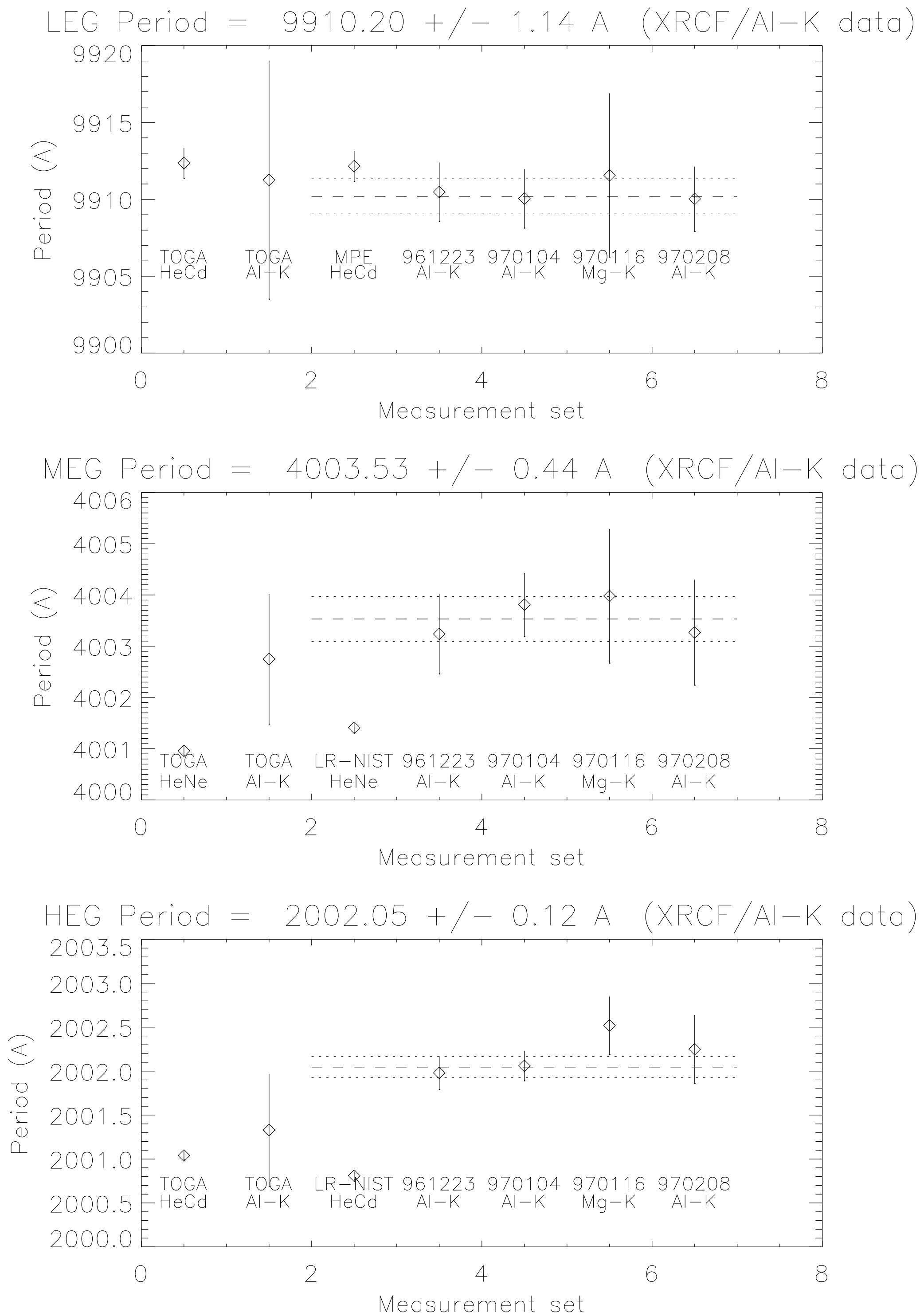

Figure 6.4: Measured Grating Periods. Parameter values assumed: $X_{\rm RS}$ = 8788.04 mm, hc = 12.3985, Al-K is at 1.4867 keV, and for TOGA $X_{\rm RS}$ = 5366.55 mm. Note that the XRCF derived periods for both MEG and HEG are larger by ≈500 ppm than the LR-NIST values, Section 4.1.2.

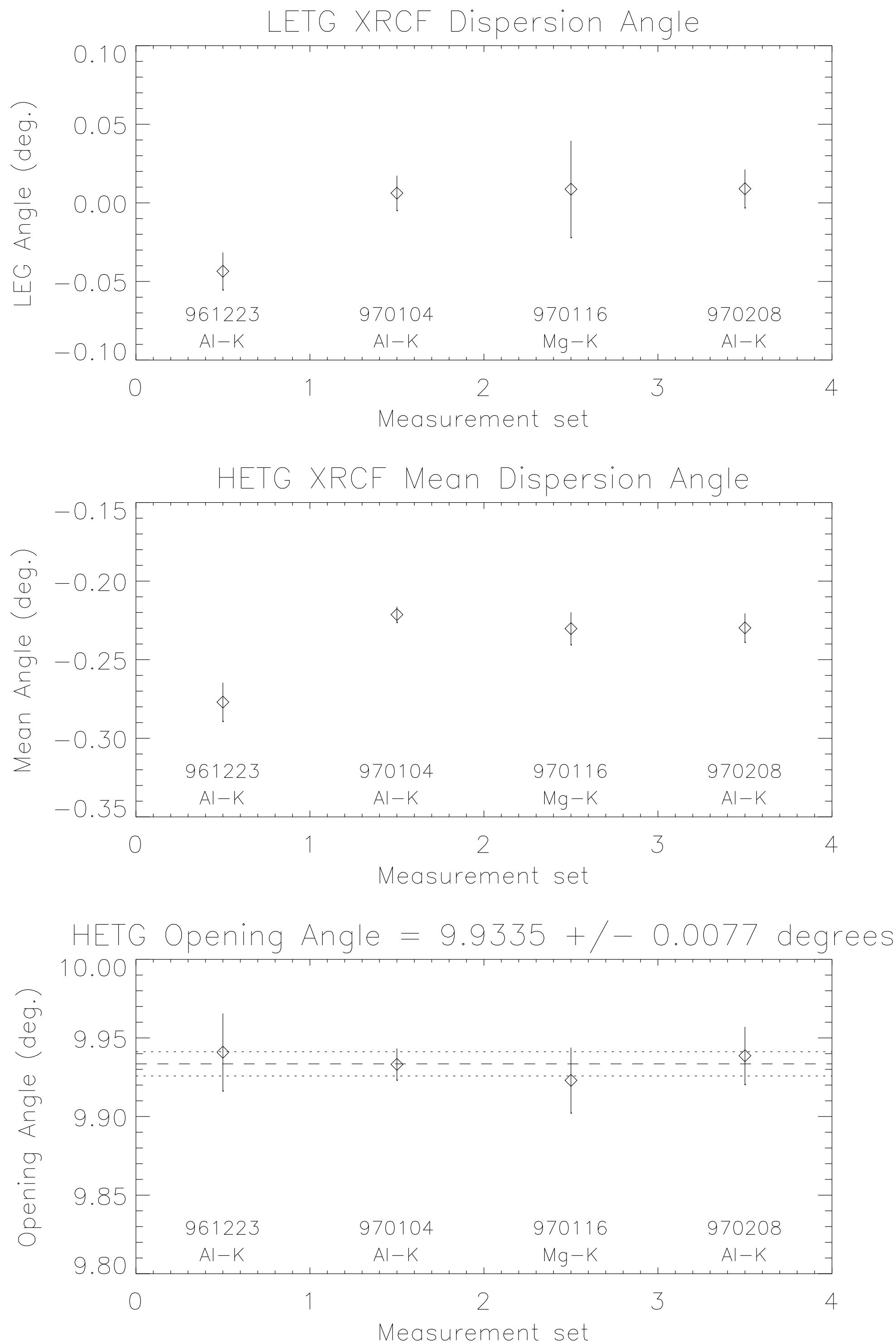

Figure 6.5: Measured Dispersion Angles. The LETG and HETG (mean) dispersion angles (w.r.t. HXDS axes) track very well through the XRCF Phase I subphases. The HETG opening angle is very stable as would be expected.

6.3 LRF Core: Period and Roll Variations

Objective: Imperfections in grating fabrication produce blur in the dispersion and cross-dispersion directions. These blurs are dominated, respectively, by the rms period variation and and the rms roll (alignment) variation. The core of the diffracted image is studied and compared with the core of the no-grating (or zero-order) image to measure the size of these variations.

6.3.1 Focus tests

The focus tests (Focus Check FC and Shutter Focus SF) were performed by cycling through the quadrants of the mirror. When examining the 0th order, the inner shells were closed for images of the MEG 0th order and opened (while closing the outer shell pair) for the HEG 0th order measurement. The displacement of the image centroids gave an estimate of the detector defocus using a simple thin lens approximation and the knowledge that the detector was already placed within 0.5 mm of the desired focus position. The insertion of gratings was not expected to have an effect on detector focus location, and this was observed to the measurement accuracy of about 25 microns. Furthermore, once the fixed offset of about 180 microns was corrected, an additional defocus measurement gave an answer consistent with zero defocus error. All 0th order images were shaped as bowties or hourglasses, depending on the set of open shutters, as expected, due to mirror scattering, which redistributes photons preferentially perpendicular to the scattering surface.

Higher order images were examined in order to verify the placement of the gratings and detectors on the Rowland circle. The detector was offset by the amount appropriate to the Rowland circle and a shutter focus was performed.

Data from D-HXH-FC-1.010, Figure 1.4, were crudely analyzed to obtain $E/dE \approx 978$ for a Gaussian fit to the LRF core. In the cross dispersion a value of $\gamma = 2$ arc minutes was determined (including astigmatism contributions.)

6.3.2 1D Scans of LRF

The direct approach to resolution measurement would be to use an X-ray source with an intrinsically narrow line at low energy. The best candidate emission line for this function was the Mg-Kα line at 1.253 keV. Lower energy K lines have resolvable natural line widths (e.g. O-K or C-K) and the L lines (of Ti, Fe, and Ni, for example) were generally much weaker and substantially more complex. Therefore, we used an indirect approach, observing the higher energy K lines at high order. Using a 200 μ m by 10 μ m slit, the HEG+1, HEG+2, MEG+1, and MEG+3 images were scanned directly ("PSF/1D" measurement) to measure the LRF. Figures 6.6 and 6.7 show the data and a simple fits for the HEG and MEG orders.

6.3.3 Results

The E/dE measurements made so far are tabulated in Table 6.2 and plotted in Figure 6.8.

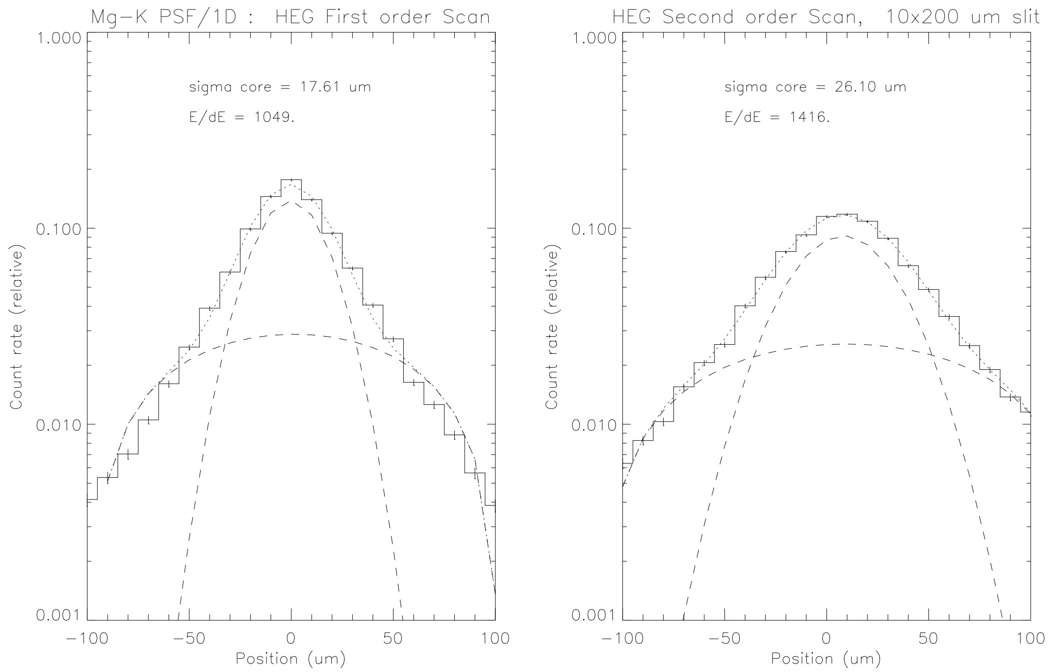

Figure 6.6: Slit scans with the FPC across Mg-K HEG 1st and 2nd orders. Gaussian approximations to the cores indicate high resolving powers are being achieved.

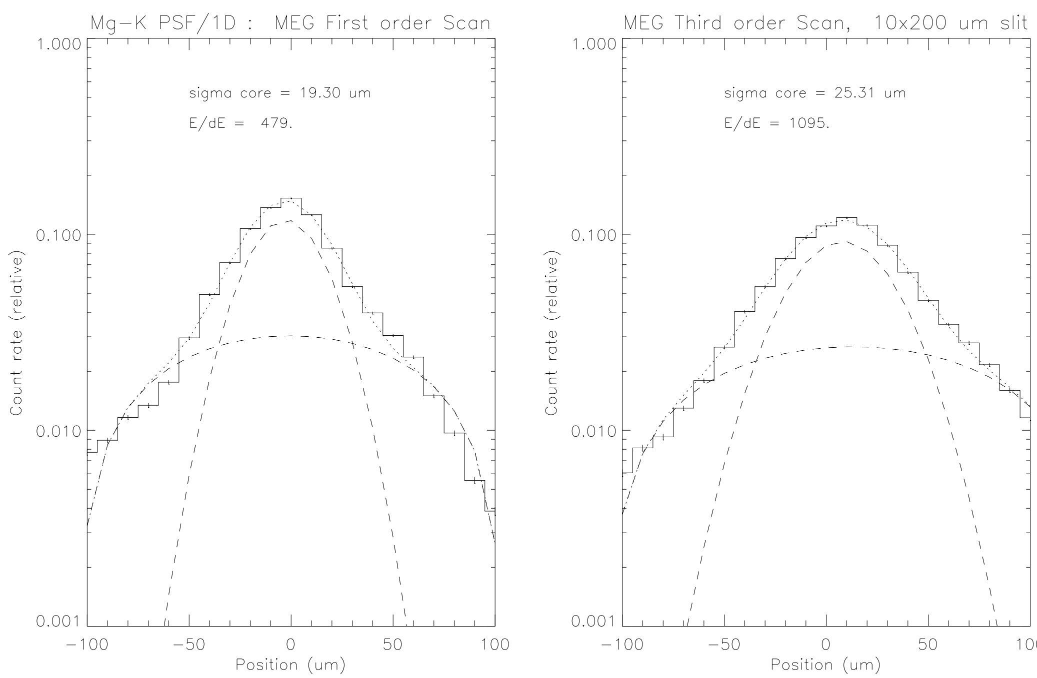

Figure 6.7: Slit scans with the FPC across Mg-K MEG 1st and 3rd orders. Gaussian approximations to the cores indicate high resolving powers are being achieved.

To-do:
Create XRCF E/dE predictions $(m = 1, 2, 3)$ for comparison with results.
Analyze all data available
Remove HRMA effects to determine grating-only contribution

Data Set	Grating	Energy	Order	E/dE	dp/p rms limit
FC (Fig.1.4)	MEG	1.486	3	978.	$<$ 435. ppm
1D scan	HEG	1.254	1	1049.	$<$ 405. ppm
1D scan	HEG	1.254	2	1418.	$<$ 300. ppm
1D scan	MEG	1.254	1	479.	$<$ 888. ppm
1D scan	MEG	1.254	3	1095.	$<$ 389. ppm

Table 6.2: Results of some XRCF LRF core measurements

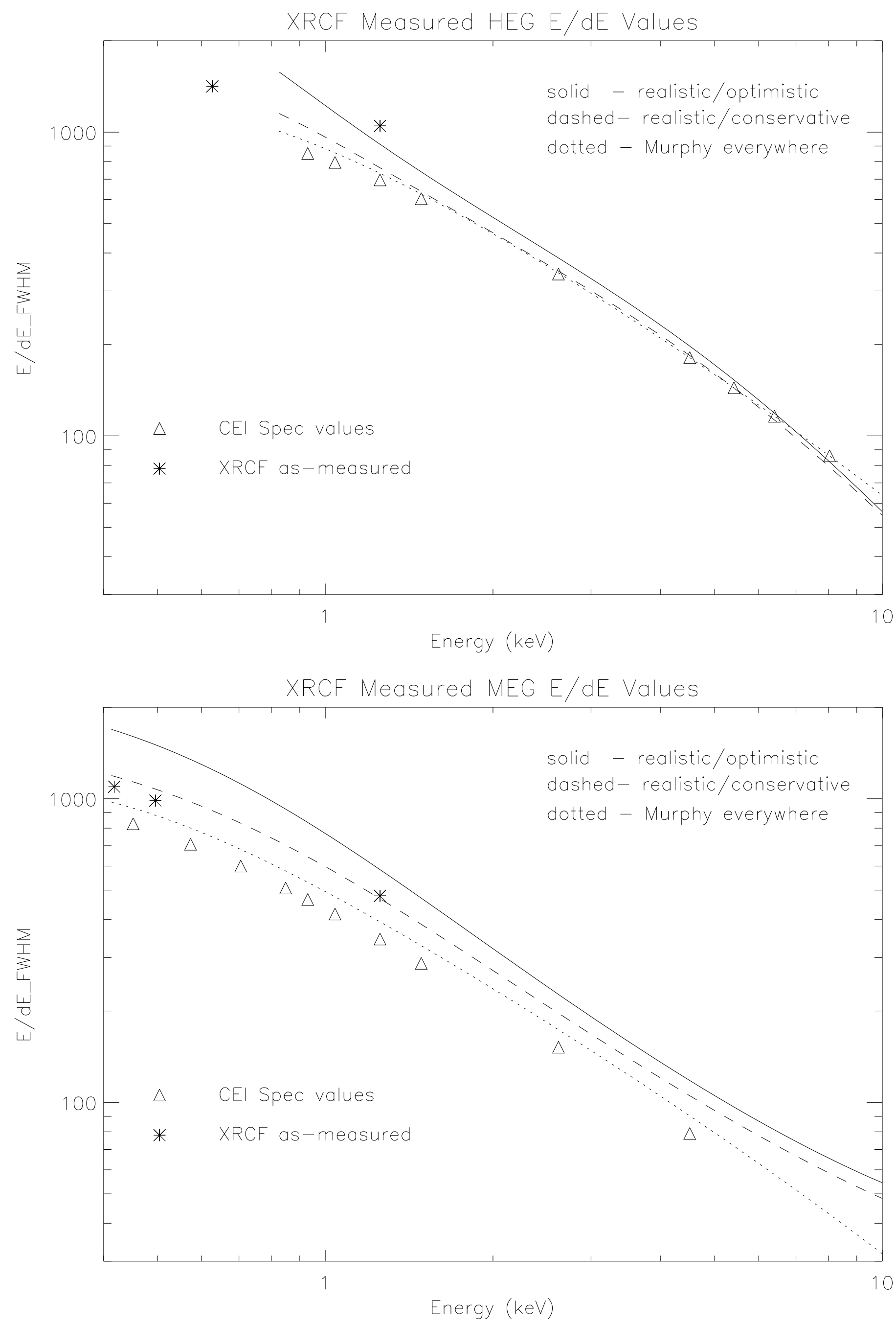

Figure 6.8: XRCF E/dE Measurements. Resolving Power for the HRMA-HEG and HRMA-MEG as measured at XRCF during Phase I. The E/dE values(*) are from Table 6.2 and the high-order points are plotted at an energy of E/m.
Various flight error budget curves are plotted for reference only (see Figure 2.2 for their details.)

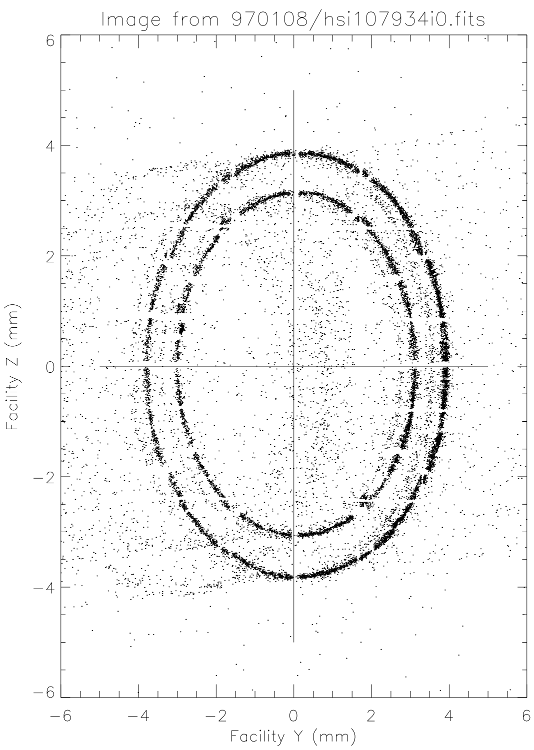

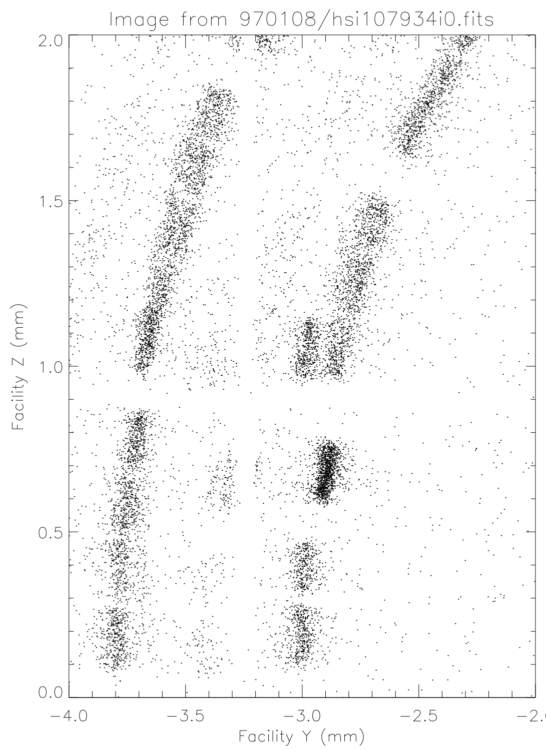

Figure 6.9: Defocussed HSI image of the MEG Al-K 3rd order. Individual grating facets are visible here in the two MEG rings of gratings. At right a blowup shows mis-aligned facets by the doubling up of the facet images near the center.

6.4 MEG Mis-Aligned Gratings

Objective: Identify the grating facets responsible for the cross-dispersion outlier images and produce a model to reproduce the data.

Surprisingly, the images of MEG Al-Kα in third order showed several additional images at the same dispersion distance as the Al-Kα line, these are the weak features at +400 and -100 in HSI Z seen in Figure 1.4. The images individually were 2-6% of the power in the main image. Several of the images were displaced in the cross-dispersion direction by 120 microns and a fourth deviated by almost 400 microns, corresponding to rotations of the dispersion direction by 7 arc minutes and 24 arc minutes, respectively. Such large rotations were not expected, based on subassembly measurements (*e.g.*, Figure 4.12) so an additional test was devised to confirm this possibility.

A defocussed image of the MEG +3 order Al-K line (Alignement test) reveals the individual facets, Figure 6.9. A grating mis-aligned in roll will show up as having its image shifted along the z' axis – this can be seen for the "400 μm offender" at around coordinates Y = -3 mm, Z = +1 mm where the regular set of grating images has a gap and a doubled facet. By analyzing this image 6 MEG gratings were found to be misaligned by 5 to 23 arc minutes. All of these were from a single fabrication lot. Further tests have confirmed that fabrication irregularities produced excess stress gradients in the grating polyimide support structure leading to inaccurate polarization

run id	Quadrant, hlm feature	$I_{\rm spot}/I_{\rm quad.}$	roll (arc min.)	HESS ID
107463	Top, -?- (see in image?)	.	+5	3EE2
107464	North, Spot 1	5.6 %	-8	3FF4
107464	North, Spot 2	2.3 %	+23	3FF5
107465	Bottom, Spot 1	3.0 %	+8	3E1
.	S/B, -?- (shutter blocked?)	.	+5	1E4
107466	South, Spot 1	4.0 %	-6	1F4

HESS ID	Grating	Lab ID	Fab ID	Al-K 3rd order	Al-K 1st order
3EE2	ME1411	189	F07M012	1.8-2.0 %	17-19%
3FF4	MD1312	201	F07M027	2.3-4.9 %	6.9-7.8 %
3FF5	MD1307	195	F07M020	1.3-1.6 %	15-17 %
3E1	ME1405	185	F07M008	1.5-1.7 %	18 %
1E4	ME1402	187	F07M010	1.5-1.8 %	15-18 %
1F4	MF1502	192	F07M017	1.4-1.6 %	18 %

Table 6.3: Mis-aligned MEGs. The upper table provides information on the identified misaligned gratings and their location on the HESS. The lower table gives information on the specific grating facets at these locations.

alignment measurement values. These "mis-aligned gratings" will be explicitly included in our instrument model.

The image in Figure 6.9 (TRW ID D-HXH-AL-27.001, run id 107934, taken 1/7/97, logged as 1/8/97) is MEG 3rd order Al-K defocussed to 65.54 mm. The main K-alpha line, satellite line, and K-beta/O-K lines are visible. The image used is the raw HSI image and HSI "gaps" are visible.

Each MEG grating creates an image in one of the shells around the rings. If a grating is mis-aligned in roll ("alignement") its image will move roughly in the +/- Z direction. The 3rd order MEG Al-K is diffracted $\approx$ 55 mm in the dispersion direction, so a 30 arc minute grating roll results in a 0.48 mm Z shift.

The events in each sector (A through FF) of each shell (1 and 3) have been converted from facility Y,Z values into R, theta about the ring center, Figure 6.10. The events for shell-sector can be view by plotting the appropriate anglular range (0 degrees is along the +Y axis, south; positive angles are right-hand rule about X, e.g., towards +Z) and radial (shell) range. The gaps between facets are generlly visible. In this theta-R space the cross-dispersion direction is indicated with an arrow of length 30 arc minutes of grating roll and pointing in the direction of "unscrewing" (+ righthand about +X). A histogram of counts vs theta helps identify the gratings, gaps, etc. The orientation of these plots is as if standing in the center of the HESS HRMA-side looking radially out towards the sector: grating 1 of the sector is to the right and grating 7/9 to the left (larger angles.)

Table 6.3 presents a list of gratings which appear to be highly-rolled. Herman Marshall identified 4 spots in the Focus Check MEG +3 image in his memo and they are here as well as two others: one in the Top quadrant (3EE2) that may be visible in the Top image and one (1E4) that is not clearly visible in South or Bottom but is is on their boundary and so may be blocked by either shutter.

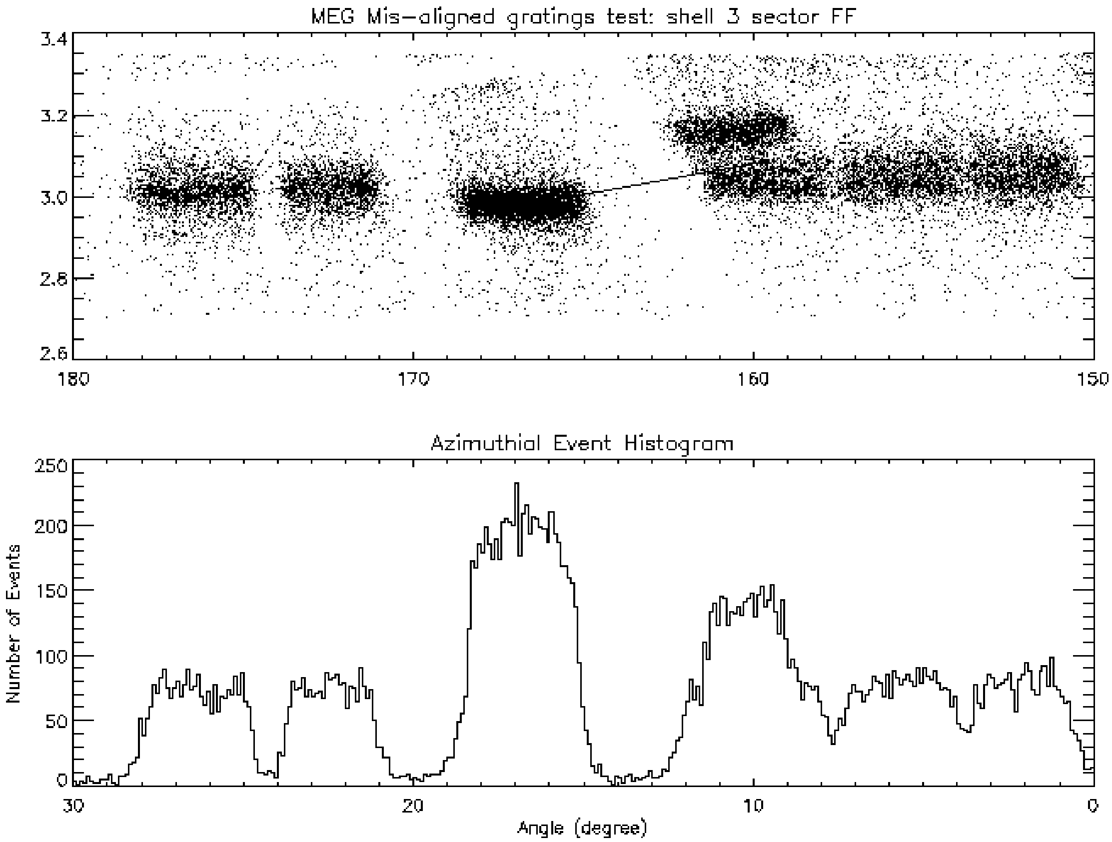

Figure 6.10: Shell 3 sector FF Events plotted in radial vs. azimuthal coordinates (top) and event histogram (bottom). The 7 gratings in shell 3 sector FF are numbered 1 through 7 from right to left. The grating in location 3FF4, bright in 3rd order, is rotated such that its image has moved left. The grating in location 3FF5 has rotated in the other direction by 23 arc minutes to almost the location of 3FF3.
In memory of Tom, grating 3FF1, its diffracted events visible on the right, is inscribed with "Thomas H. Markert" inplace of a grating ID.

Note that all of these gratings are from Lot F07M ! In fact these are 6 of the (only) 11 lot F07M gratings that are on the flight unit. The other five are: 3EE3, 1FF5, 1F1, 3F5, 3F2.

6.5 Between Core and Scatter

Objective: Determine the detailed structure of the grating effects on the PSF in the region between the LRF core and the scatter region. Ideally, this may be well modelled by a period distribution function.

Create a composite LRF from the core through the wings and scatter by merging all available data.

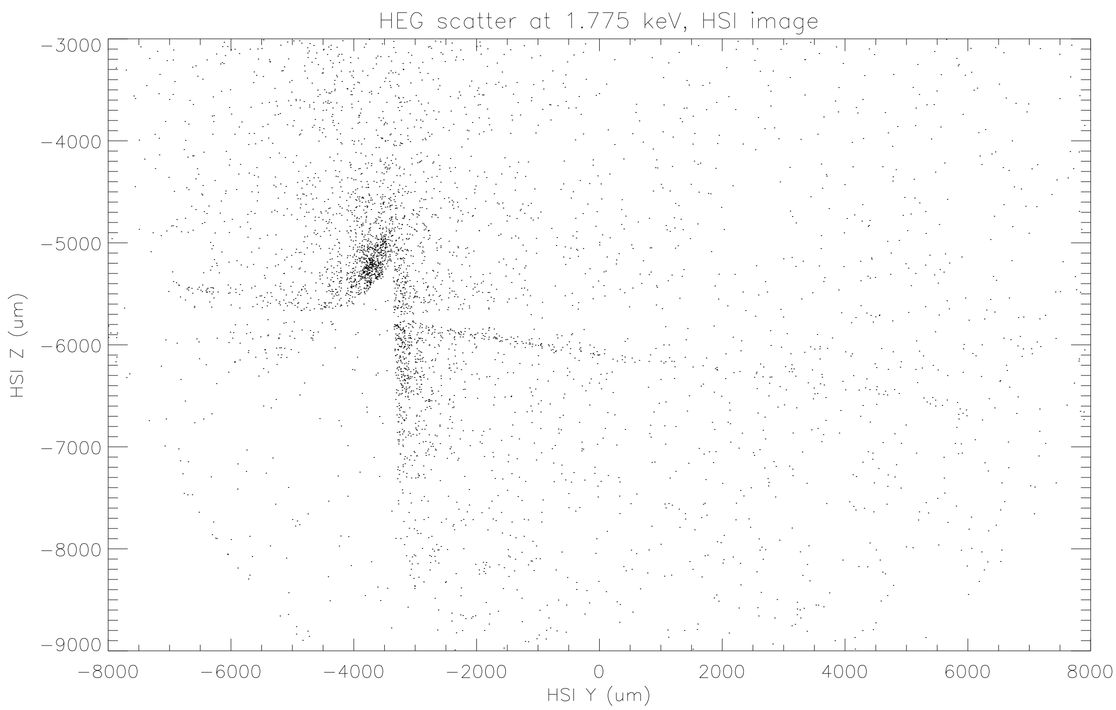

Figure 6.11: Phase I HEG scatter test. The core of the HSI image of the DCM monochromatic 1.775 keV line in HEG first order is blocked by the HSI cusp (triangular low-count region.) Extending from the cusp along the HEG dispersion axis are scattered 1.775 keV photons. Of order 0.4% of the line flux is scattered.

6.6 Scatter

Objective: Measure or set upper limits on the wide-angle contribution of the grating to the LRF, *i.e.*, the "scatter". Investigate the energy dependance of the scatter and the ability to fit it with a model.

6.6.1 Phase I HSI Data

A test series was developed to search for near line scattering wings (PSF/Outer, Scattering) that would be a concern when measuring absorption features near bright lines. The Double Crystal Monochromator (DCM) was tuned to the bright line W-Mα at 1.775 keV in the anode spectrum. The current was turned to the lowest possible value to get a count rate for the total line and then the current was turned to the highest possible value for the scattering test. The image was placed on a detector mask "cusp" in order to block the core of the image but allow photons beyond $E/100$ of the target line. Mirror scattering was expected but would be azimuthally symmetric, while grating line scatter was expected preferentially along the direction of dispersion, so would be distinguishable from mirror scattering. After a long integration at high current, a total of 100,000 counts would be obtained from the core of the line (without the blocking cusp), so the test could detect scattered power levels below 0.1% of peak.

The result, Figure 6.11, was somewhat surprising at the time: although there was no obvious evidence for power along the dispersion direction near the line, there were clearly significant events dispersed 1-10 mm from the line. In order to verify that the DCM had no significant spectral leakage that could cause the observed effect, we tuned the DCM off of the bright line by only 15 eV. The DCM resolution at 1.775 keV is about 5 eV, so very little power was expected and the current was turned up to its maximum setting. There were no events at the expected dispersion location of 1.775 keV, indicating that it had been suppressed at a level better than one part in 10^5. We concluded, therefore, that the gratings were incoherently diffracting a modest fraction of the line emission to large dispersion distances. This fraction was estimated at 0.4% over a 10 mm span.

Subsequent modelling and further tests indicated that minor bar location variations could cause an incoherent redistribution of monochromatic light. The grating-bar variations needed can be quite small, of order a few percent of the the distance between bars, Section 3.3.

To-do:
Create normalized scattering plot from HSI data and compare with '2C data (Figure 6.18.)

6.6.2 HETG Scatter Tests with ACIS-2C

The data for this analysis came from XRCF tests G-H2C-SC-88.001 through 88.005. The objective of this test was to map out the distribution of the flux dispersed by the HEGs that does not go into integer orders.

6.6.2.1 Setup

For this test, the HETG was used in combination with the DCM set to the bright W Mα line at 1.775 keV, and the HRMA with all shells open. The detector is the backside illuminated chip (ID 0, detname was "w148c4") in the ACIS-2C detector. The detector was run in 114 row mode, so the integration times were about 0.66 s. In this mode, the MEG and HEG spectra criss-cross through the detector window, Figure 6.12. In order to map the so-called "scattered" light out to +3 order, the '2C0 was positioned by the FAM to 5 locations 22 mm apart along the +Y axis. Since the actual level in the lines was not of primary concern, the cores of the dispersed orders were allowed to pile up.

The reduction and analysis were done in IDL. The data came in FITS format as the result of second floor processing at the XRCF and was read into IDL using the **mrdfits** routine. Besides the event data, various test- and ACIS-specific FITS keywords were read. The keyword values were used to set system parameters and calibration values such as the detector gain, the grating period, mirror focal length and Rowland distance. The event finding algorithm used in quicklook processing does not process the last two rows of data, even though the charge in these rows is collected. This feature is evident as a 2 pixel wide gap. PH data for each event consisted of 25 values in a 1-D array.

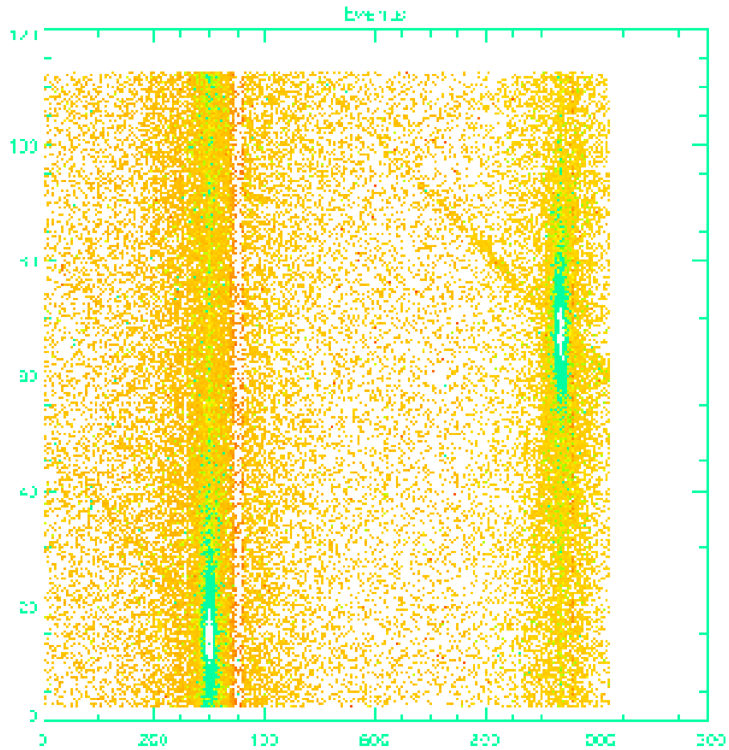

Figure 6.12: ACIS-2C event plot showing HEG scatter at 1.775 keV. The range shown is 114 rows tall by 1024 columns wide. Zero-order is off the chip to the left, MEG first order is on chip at left and HEG first order is on chip at right. The scattered light from the HEG is visible as the upper-left-to-lower-right diagonal streak through the HEG first order; this is the HEG dispersion direction. Due to the wrapping of the ACIS-2C readout mode used, this scattered light appears to go through the MEG first order. Note that the MEG produces no scattered light as there is no 'lower-left-to-upper-right' streak along the MEG dispersion direction.

6.6.2.2 Reduction Details

The reduction proceeded as follows.

1. Various FITS keywords were read: ONTIME to get the exposure time, OBS_ID to get the TRW ID, WINSIZE to get the ACIS-2C window size (in pixels), CCD_ID to get the character setting which chip in the 2C was being used (so the detector name is assigned to ACIS-2C0 to indicate the BI chip in the 2C), DETNAM to get the chip serial number, and TLMAX4 to determine the number of columns allowed. The TRW ID is parsed into components to give the XRCF phase, grating, and detector assembly.

2. The chip serial number is used to set the chip gain parameters. For the chip used in these tests, w148c4, no "official" values were available, so the gain was set to 0.322 DN per eV, estimated from the PH distribution so that the highest peak would centered at the DCM energy, 1.775 keV.

3. The 25 PH values were reordered from the subassembly order, which places the center event first, to the flight order, where the center event is 5th in the array. The event PH

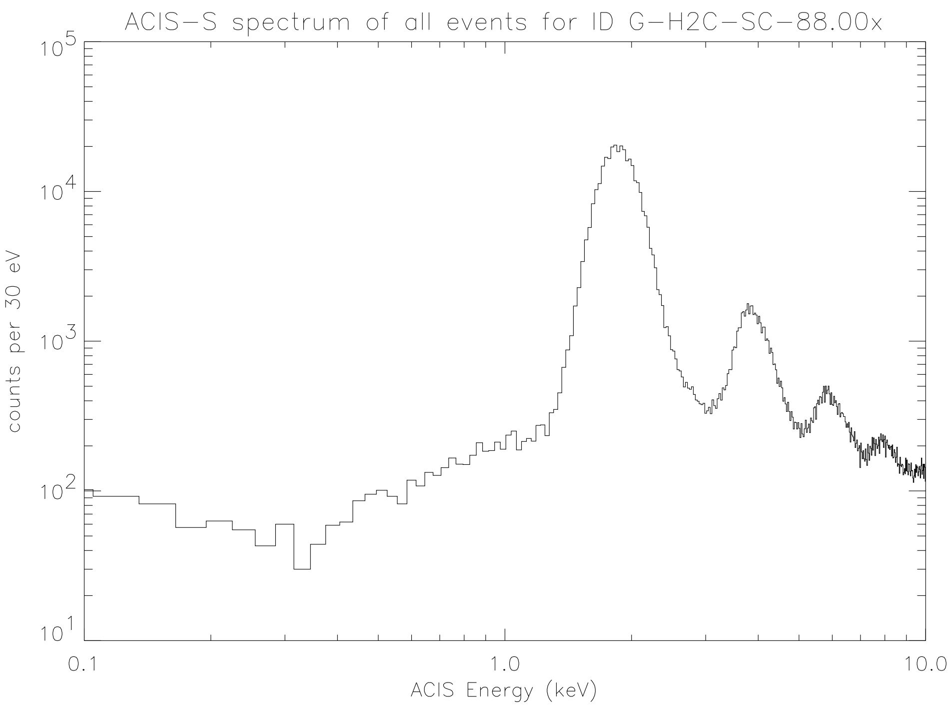

Figure 6.13: Pulse height distribution for the entire five image data set, converted to energy in keV. The input is monochromatic at 1.775 keV, so all features are related to pileup or incomplete charge collection

amplitude is formed as the sum of all 25 PHs. The "ASCA" grading criterion is applied to the 3x3 PH data but is not used in processing. The event amplitudes are converted to energy using the chip gain and offset parameters.

See figure 6.13 for the pulse height distribution for the entire 5 image data set. The input is monochromatic at 1.775 keV and background is negligible. Thus, the pileup peaks are apparent and there is a tail of incomplete charge collection events below 1 keV. The ACIS-2C0 gain parameters vary significantly over the entire array, so peaks are broad.

4. Randomized event chip coordinates by ± 0.5 pixel.

5. Offset by FOA loc (584, 72.8), then rotated -0.58 degrees to convert from chip (real) XY to XRCF YZ. The rotation angle and offset were estimated from the first image where the FAM position was set to (0,0) so that the 0th order image would be centered and the HEG scattering would be horizontal after HEG rotation in step 7

6. Offset by FAM Y and Z shifts. Coordinates are now in pixels from 0th order. Subsequent analysis (section 6.6.2.3) showed that the commanded and reported values, both specifying no motion in Z and 22 mm motions in y only, gave incorrect results.

7. Rotated XRCF YZ coordinates by the grating dispersion angles (HEG: -5.2 degrees, MEG: 4.7 degrees), determined from the value of the angle of the MEG-HEG bisector, -0.225 degrees and the MEG-HEG opening angle, 9.934 degrees, taken from analysis of Phase I EE data (see Section 6.2). New coordinates are dispersion y' and cross-dispersion distances z' in pixels. NOTE: The rotation is about the (virtual) 0th order location, not chip FOA, so the rotations are distinguishable (as with HSI).

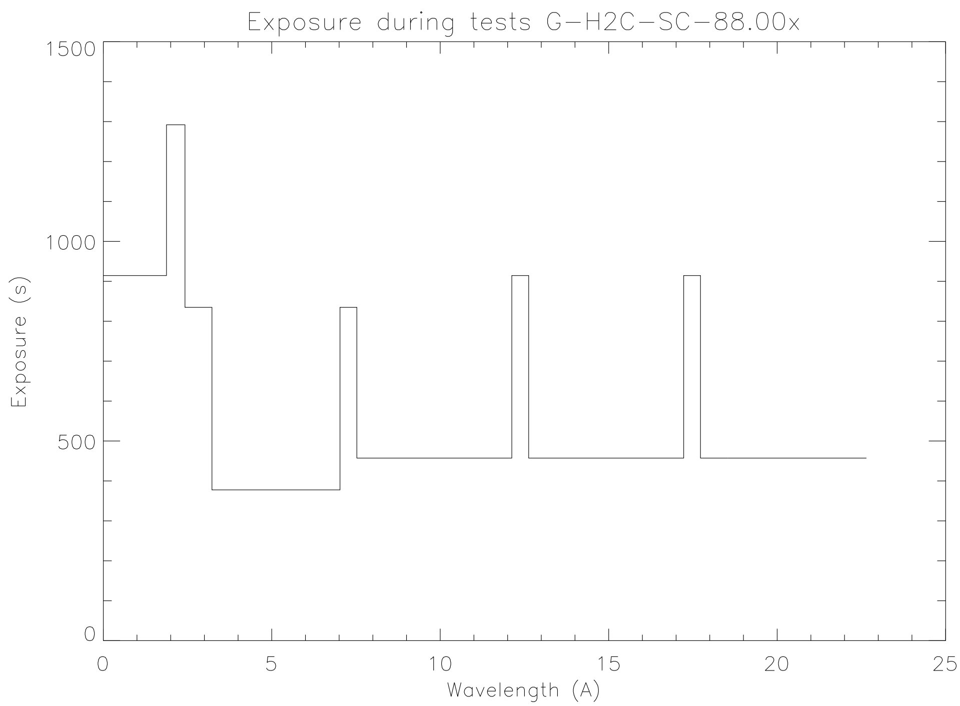

Figure 6.14: Exposure time "map"for the '2C HEG scattering tests.

8. Coordinates are scaled to physical units (mm) using 24 microns per ACIS pixel.

9. "Unwrapped" the '2C image in order to center the dispersion axis. The result depends only on the cross-dispersion distance, z'. The event z' values are offset by plus or minus W to put them in the range $-W/2 <$z'$< W/2$, where W = 114 $\times$ 0.024 mm.

10. Wavelengths are based on the grating equation $\lambda = |p \sin\beta|$, where p is the grating period (either 4001.13 Å for the MEG or 2000.81 Å for the HEG), $\tan\beta = y'/X_{\rm RS}$, y' is the dispersion distance, and $X_{\rm RS}$ is the Rowland spacing, taken to be 8782.8 mm. See Section 9.3.2 for a discussion of these values.

11. Converted z' values to angles (in arcsec) using the XRCF HRMA focal length, taken to be 10258.30 mm.

12. The exposure for each wavelength bin was estimated by setting up dummy "events" at the chip corners. These events were sent through the same transformations as the photon events, steps 5 through 11. The chip exposure time was added to array elements corresponding to all allowed wavelength bins.

13. Energies are computed from the event wavelengths.

14. Accumulated exposures for each (overlapping) ACIS-2C0 position. The events were concatenated. Figure 6.14 gives the resultant exposure time as a function of wavelength, adding all 5 chips.

6.6.2.3 Analysis Results

The events were binned into an array with 0.05 Å by 0.5 arcsec pixels. Events were not restricted on the basis of ACIS energy (i.e. event amplitude) because there were many piled events and incomplete charge collection events with low total PH values.

Some of the conclusions that can be drawn from the binned images follow.

1. The MEG shows no detectable scattering. This is evident on many images but no quantitative limits have been measured yet.

2. The cross-dispersion profiles were fitted with Gaussians of variable location, width, background, and normalization at each wavelength bin for HEG scattered light only in order to diagnose effects of the data reduction procedures. An aperture subtraction technique could not be applied immediately because it was apparent that the initial assumptions about the FAM motion were incorrect. Figure 6.15 shows results from one reduction run. Fits have been eliminated where unreasonable centroids, widths, or intensities were obtained, causing gaps in the plots. Some bad data points remain, however, and have to be reviewed individually.

3. A pattern of rotated spectra in each measurement was corrected by applying a rotation in the ACIS-2C0 frame about the FOA. A "global" drift remained; centroid values in figure 6.15 drift downward by about 1.0 arcsec as the wavelength increases from 5 Å to 21 Å. This drift is corrected with a 0.016 mm Z shift for each 22 mm FAM motion. This drift could be caused by a difference between the FAM and XRCF Y axes (defined in phase C) of 0.04 degrees.

4. The total counts in the cross dispersion profiles are given by the integral over the Gaussian, which is proportional to the fitted normalization and the fitted σ. These data, also shown in figure 6.15, show the dispersion peaks expected at multiples of 7.0Å and at the wavelengths halfway between due to the MEG. Bad fits often occur at these locations because the profiles are not Gaussian when the line cores are so dominated by event pileup. The wavelengths are measurably different from the expected values, reaching a maximum deviation of 0.5 Å at the HEG +3 location, expected to be observed at 21.0 Å. The wavelength errors are eliminated by assuming that the FAM moved 22.25 mm on each step, 1.1% too far. The FAM was commanded to move 22.000 mm and FAM log data agree, so the source of the discrepancy is not known at this time.

5. For the remaining analysis, a simple aperture extraction method was sufficient because the spectrum was level and smooth. The source aperture was defined to be 2.5 arcsec (5 pix) wide and background was estimated from a region 11-26 arcsec above the source. Figure 6.16 shows the count spectra derived in these two regions.

6. Subtracted background and normalized to expected rate in first order of 1700 cps. Figure 6.17 shows the net scattered light after dividing by the estimated exposure time. There are still background subtraction errors near the MEG and HEG orders but the overall subtraction is good off the lines so that the scattered light is apparent.

7. Added points at +1, +2, +3 orders affected by pileup in order to make a figure that combines the dominant grating orders from HEG "coherent" diffraction with the HEG incoherently diffracted or scattered light. The total scattered light gives 17 count/s and is normalized to the count rate expected from the W-M line in +1 order, which is estimated to be about 1700 count/s. Thus, the total of the incoherently scattered light is estimated

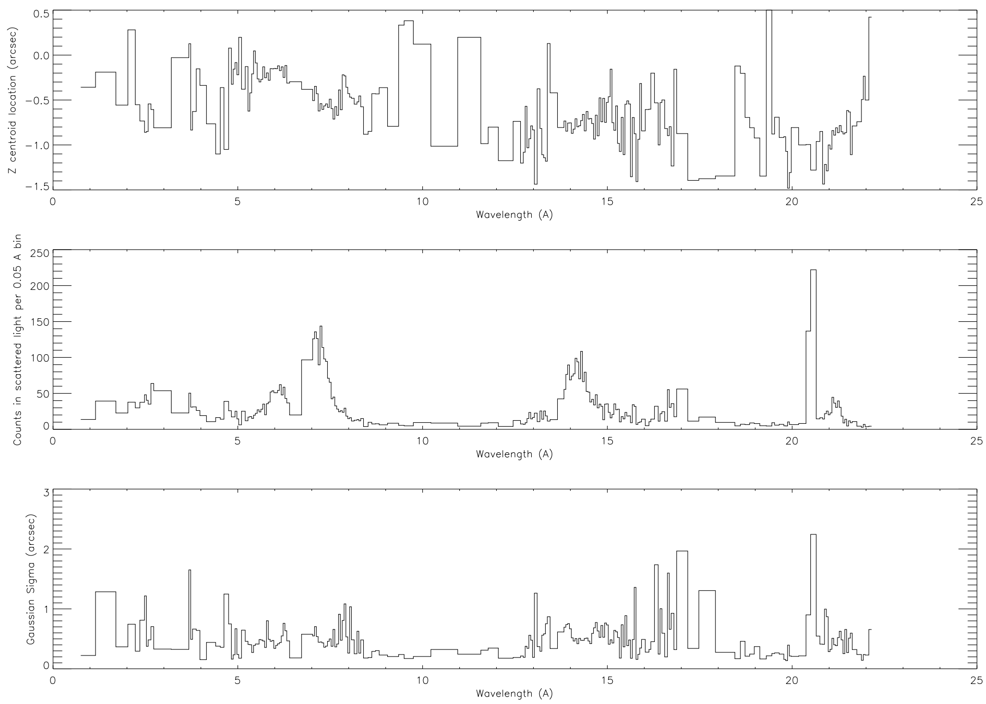

Figure 6.15: Fitting Gaussian functions to the HEG scattered light cross-dispersion profiles. *Top curve* The centroid location in arc seconds from a fiducial horizontal reference. Note that the centroid drifts downward by about 1.0 arcsec as the wavelength increases from 5 Åto 21 Å. *Middle curve* The inferred total counts in the Gaussian fits. Scattering peaks appear near 7 Å, 14 Å, and 21.2 Å. Bad fits occurred at the HEG and MEG orders. These should have been at 3.5 Å (or 7.0 Å for the MEG +1), 7.0 Å (HEG +1), 10.5 Å (MEG +3), 14.0 Å (HEG +2, MEG +4), etc. At HEG +3, the line is observed at 20.5 Å, compared to the expected value of 21.0 Å, thus wavelengths of orders showed systematic error. The wavelength errors are eliminated by assuming that the FAM moved 22.25 mm on each step, 1.1% further than the commanded motion. *Bottom curve* The fitted Gaussian sigma parameter; good fits give values near 0.5 arc sec (about 2 ACIS pixels, as expected).

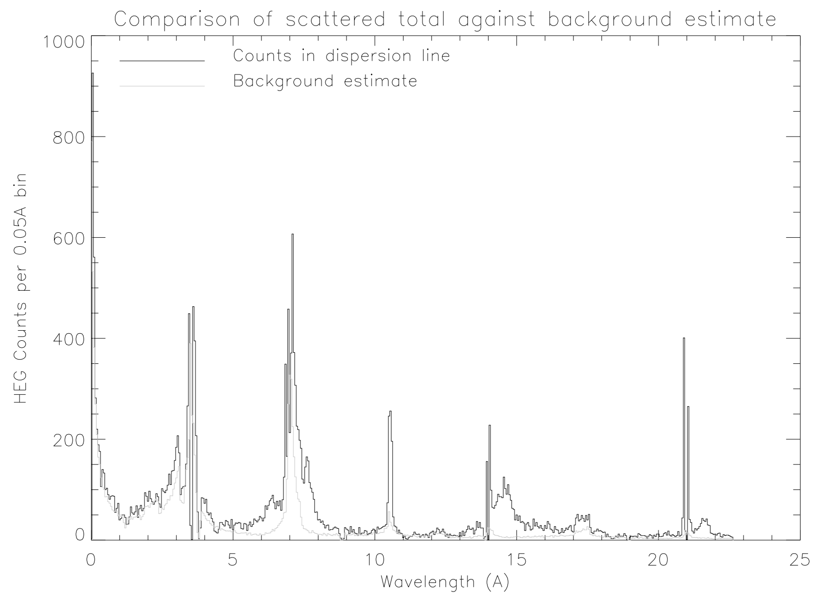

Figure 6.16: The estimated "background" and the count spectra in the source region. Note that the background increases towards 0Å due to mirror scattering from 0th order. The orders show up in background due to mirror scattering and when the MEG image does not land on top of the HEG image; e.g., at 10.5 and 17.5 . (Note wavelengths have been corrected for the FAM motion error mentioned in figure 6.15.)

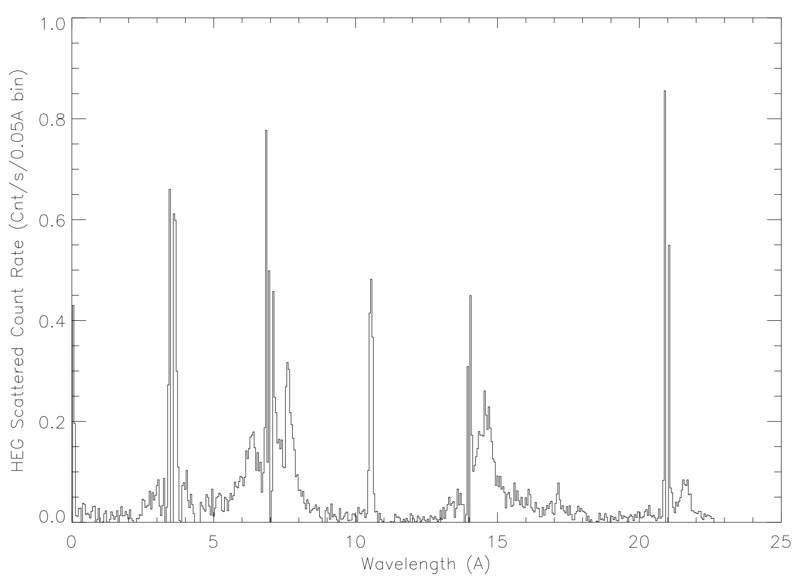

Figure 6.17: The net scattered light after dividing by the estimated exposure time. There are still background subtraction errors near the MEG and HEG orders. Scattered light is apparent well away from the dispersed orders.

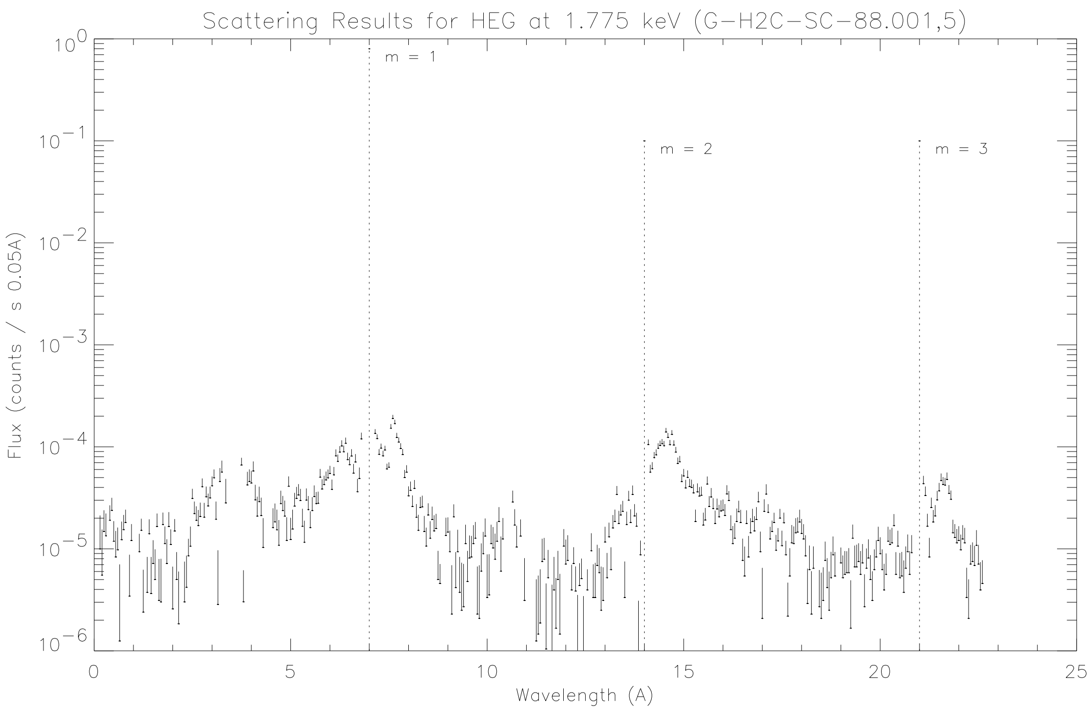

Figure 6.18: Estimate of the normalized response of the HEG to a monochromatic light source at 1.775 keV, including coherent scattering into the HEG orders (up to +2 HEG) and incoherent diffraction (scattering) in between. Some bad background subtraction results have been eliminated. Error bars (in positive direction only) have been added to show that the "detection limit" is about 1e-5 of total power per 0.05 Å bin.

to be about 1% of the power in first order. The scattered light is occasionally detected at values approaching 2×10^{-4} of the flux in order +1. The detection limit is about a factor of 20 below this value.

6.6.3 Interpretation of scattering profile results

Theoretical work to interpret these data are in progress, e.g., Section 3.3, but the highly structured, asymmetric, and off-order scattering peaks seen here are probably telltale features that the models must produce.

To-do:
Reduce all scatter data (several energies are available as well)
Reduce HSI, '2C, and ACIS LRF/scatter data to a common format for intercomparison
How and do we need to include scatter in out instrument model?

6.7 Offaxis and Defocus Tests

Objective: Compare the XRCF grating data taken under offaxis and defocus conditions to predicted images from **MARX** in order to validate the model in these conditions.

6.8 ACIS-S Rowland Conformance

Objective: Use the ACIS-S focus check (shutter focus) measurements to measure the conformance of the ACIS-S to the Rowland (best focus) curvature.

Section 7

XRCF Efficiency and Effective Area Measurements

7.1 Overview

7.2 Alignment Tests

Objective: Compare the defocussed ("ring focus") images with and without the HETG inserted to look for any gross vignetting that would indicate a decentering of the HETG with respect to the HRMA rays.

Using data from the no-grating ring-focus image C-IXH-RF-1.005 (961223/106856) and the grating-in "alignment" image C-HXH-AL-4.002 (961223/106860), the sector-by-sector grating-in/grating-out ratio is measured. The measured ratios are shown in Figure 7.1 for shells 1 and 6 (wide histograms.) Also plotted is a simple estimate of each grating's zero-order diffraction efficiency (from the X-GEF facet measurements) as it varies around the shell. The measured ratios have been adjusted by an overall normalization. This very preliminary analysis shows rough agreement between the measured and predicted efficiency variations; a more detailed analysis should allow vignetting and decenter limits to be placed on the as-installed HETG at XRCF.

To-do:
Re-analyze the images on a finer scale
Use the detailed X-GEF model parameters to create zero-order efficiency values.
Analyze the reference BND data to set absolute scale for normalization.

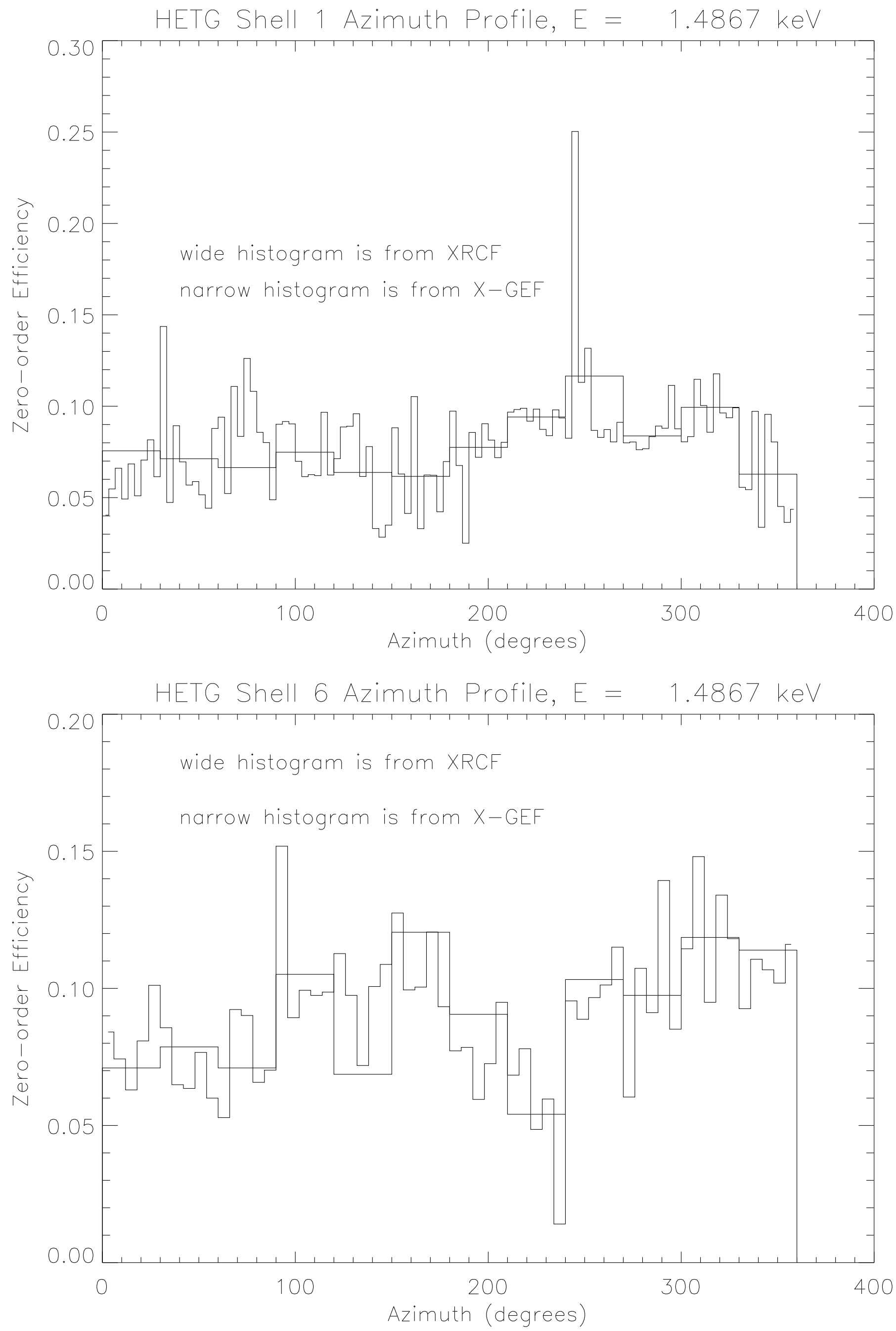

Figure 7.1: "Alignment" Test Results, Shells 1 and 6.

7.3 XRCF Source Characteristics

7.3.1 Source Spectra and Efficiency Measurements

Objective: Use the HSI images of the various source lines to create a grating-derived high resolution spectrum of the source.

Source spectra from grating-HSI observations are available at:
`http://space.mit.edu/HETG/xrcf_sources/sources.html`

7.3.2 Beam Uniformity Effects on Efficiency Measurements

Objective: Evaluate the effect of non-uniform illumination on "grating-in grating-out" efficiency measurements in Phase I and on relative efficiency measurements in Phase II.

7.4 Efficiency: Phase 1, Fixed Energies

Objective: Derive the diffraction efficiency of the HEG or MEG using Phase I "grating-in grating-out" measurements made at fixed (non-scanned, non-continuum) energies.

7.4.1 System Effective Area

The system effective area is calculated from the measurements through the equation:

$$SEA(E_{\rm line}, m, {\rm mode}) = \frac{\text{focal plane counts/s in line order}}{\text{source flux in line}} \quad [\frac{\rm counts/s}{\rm photons/cm^2 s} = \frac{\rm cm^2 counts}{\rm photon}] \tag{7.1}$$

where the units for the quantities are given as well. (Although the terminology "line order" suggests grating applications these considerations apply to HRMA-only measurements as well.) The numerator is derived from the focal plane data through:

$$\text{focal plane counts/s in line order} = R_{\rm fp}({\rm mode}) \times L_{\rm fp}({\rm aperture}, {\rm spectrum}, QE_{\rm fp}) \tag{7.2}$$

where the focal plane rate $R_{\rm fp}({\rm mode})$ is the observed count rate in the data—generally this count rate will represent the counts per second within a spatial-spectral "bump" in the data, *e.g.*, the counts in the ROI region of the FPC_X2 spectra. As such this quantity, and others that follow, *has meaning only in the context of a specific analysis method.* The variable "mode" is used here to indicate the additional effect that this rate can depend on the focal plane detector mode of operation, *e.g.*, continous *vs.* timed-exposure modes for ACIS.

The focal-plane line fraction term $L_{\rm fp}({\rm aperture}, {\rm spectrum}, QE_{\rm fp})$ is a conversion factor from the observed count rate to the count rate that would be due to the line fraction alone. This factor is required because the sources are not truly mono-chromatic and the detectors do not fully separate the line, as indicated in the discussion regarding Figures 5.3 and 5.4 above. The line fraction defined here will generally not depend on the detector mode, but *is* taken in the context of an analysis method, *e.g.*, the line fraction will be different if ROI analysis is performed or XSPEC[14] fitting is used.

Note that the SEA as defined here is equivalent to the "total effective area" into 2π and there is an assumption that the line-fraction correction also includes a small correction for the line counts that are outside the aperture. Not discussed here but treated similarly is the *Encircled Effective Area* (often called "Encircled Energy"), *e.g.*, $EEA(E_{\rm line}, m, {\rm mode}, {\rm diameter})$ which considers only the counts within the aperture.

The SEA denominator, "source flux in line", is given by:

$$\text{source flux in line} = \frac{R_{\rm BND} \times L_{\rm BND}({\rm spectrum}, QE_{\rm BND})}{QE_{\rm BND}(E_{\rm line}) \times A_{\rm BND@HRMA}} \tag{7.3}$$

where the BND rate $R_{\rm BND}$ and BND line fraction $L_{\rm BND}(\text{spectrum}, QE_{\rm BND})$ are defined analogously to the focal plane terms above. The two additional terms in the denominator provide the key ingredients for the calibration: the BND quantum efficiency $QE_{\rm BND}(E_{\rm line})$ provides the conversion from counts to photons for the BND (supporting relative calibration), and the BND area $A_{\rm BND@HRMA}$ is the equivalent geometric area of the BND detector at the HRMA aperture and provides the absolute calibration; for the BNDs near the HRMA (*e.g.*, FPC_HN fully open) this value is 32.55 cm^2.

7.4.2 Optic Effective Area

In the calibration of the optical components, the HRMA and HRMA-Gratings, it is useful to consider the *optic effective area (OEA)* which represents the ability of the optical system to collect photons and does not include detector effects:

$$OEA(E_{\rm line}, m) = \frac{\text{focal plane photons/s in line order}}{\text{source flux in line}} \quad [\frac{\text{photons/s}}{\text{photons/cm}^2\text{s}} = \text{cm}^2] \qquad (7.4)$$

where we get the usual cm^2 units. The OEA may be calculated from the measurements through:

$$OEA(E_{\rm line}, m) = A_{\rm BND@HRMA} \times \frac{R_{\rm fp}(\text{mode}) \times L_{\rm fp}(\text{aperture}, \text{spectrum}, QE_{fp})}{R_{\rm BND} \times L_{\rm BND}(\text{spectrum}, QE_{\rm BND})} \qquad (7.5)$$

$$\times \frac{QE_{\rm BND}(E_{\rm line})}{QE_{\rm fp}(E_{\rm line}, \text{mode})}. \qquad (7.6)$$

When the focal plane detector has a QE identical to the BND detector the last term is unity and, for non-dispersed orders ($m = 0$ or HRMA-only), the line-fraction corrections are also close to unity. In this way the HRMA effective area can be accurately measured[27].

7.4.3 Optic Effective Area Results

Figures 7.2 and 7.3 show the results of an initial analysis of the fixed-energy Phase I optic effective area measurements of the HRMA-HETG in 1st-order and zero-order. A crude region-of-interest analysis (*e.g.*, Figure 5.3) was performed and a simplified version of the optic effective was calculated:

$$OEA(E_{\rm line}, m) = A_{BND@HRMA} \times \frac{R_{\rm fp}}{R_{\rm BND}} \qquad (7.7)$$

The solid curves in these Figures are the combination of the pre-XRCF mirror model with the pre-XRCF HETG efficiency data; the dotted curves give an estimate of the error range for the predictions. The data points have horizontal lines to indicate the size of the data statistical errors; the vertical lines indicate an estimate of the measurement systematic errors.

The 1st-order HRMA-HETG effective area curves can be divided (somewhat arbitrarily) into 5 regions where different physical mechanisms govern the effective area of the optical (mirror-grating) system:

below 1 keV – The polyimide membrane of the gratings is dominating the area changes, with edges due to C, N, and O.

1-2 keV – The phase effects of the grating cause an increasing enhancement of the diffraction efficiency.

2-2.5 keV – Edge structure from the mirror (Ir) and grating (Au) dominates, sharply reducing effective area.

2.5-5.5 keV – Effective area is slowly varying, with some low-amplitude Ir and Au edge structure.

5.5-10 keV – The mirror reflectivity and grating efficiency are decreasing rapidly with energy.

Horizontal error bars on the data indicate the corresponding statistical error of the measurement, which is generally below ± 5 %. The vertical error lines indicate the probable systematic errors estimated for the 1st-order measurements as $+30$ % and -10 %. These data illustrate that the absolute effective areas are close to expected values and they show the large range of energies sampled at XRCF.

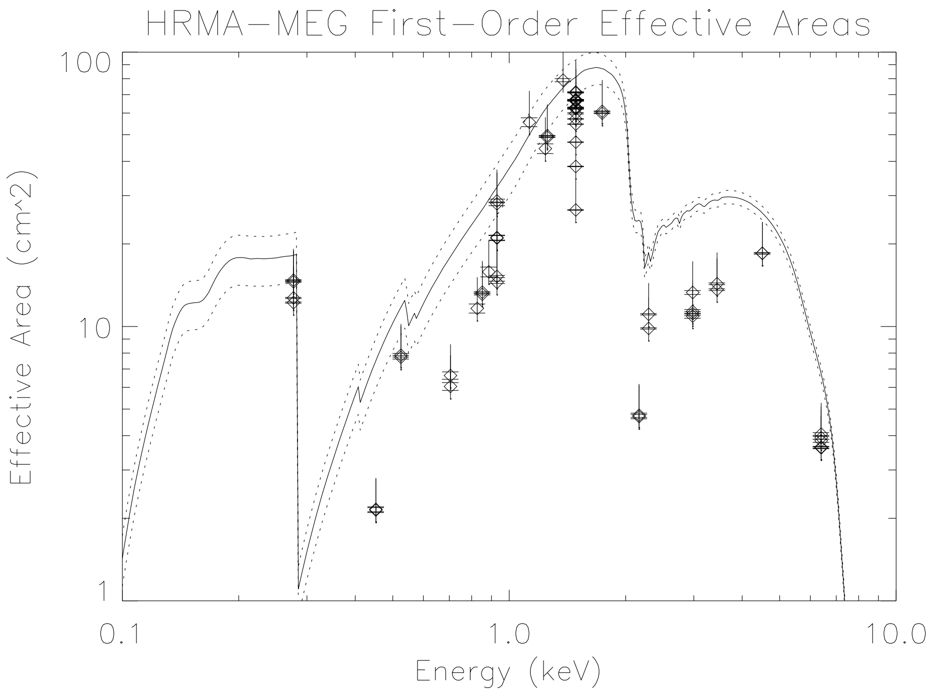

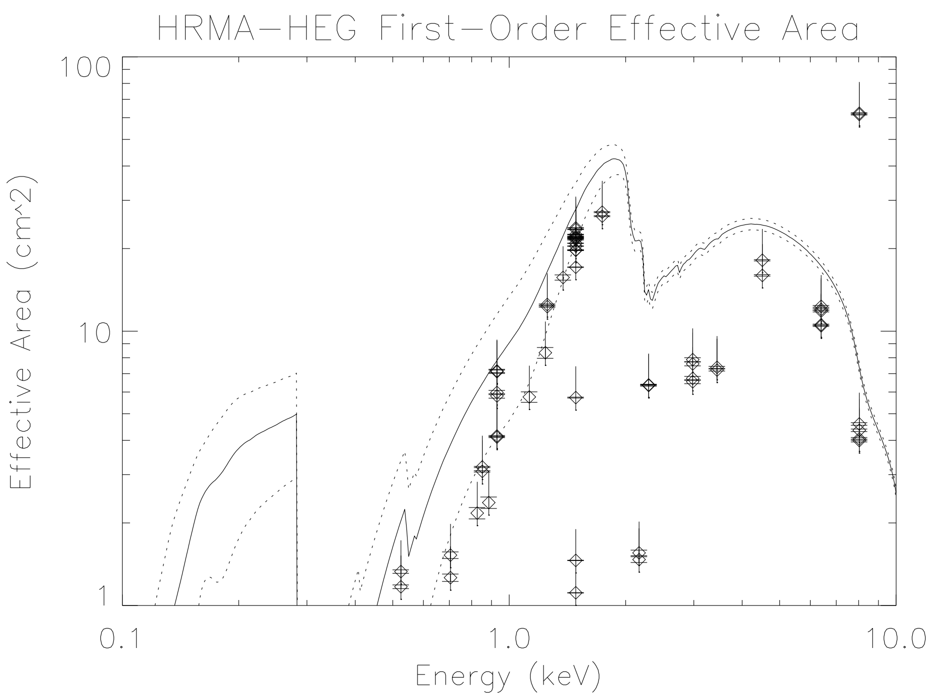

Figure 7.2: Preliminary First-order Optic Effective Area results for the HRMA-MEG (top) and HRMA-HEG (bottom) at XRCF. These plots represent the automated application of the simplified Equation 7.7 to 132 fixed-energy data sets from Phase I.
Discrepancies arise from i) the need for "line-fraction" corrections (the L functions of Equation 7.5), ii) departure of the HRMA area from prediction, and iii) inaccurate facility setup information (*e.g.*, incorrect BND aperture sizes.)

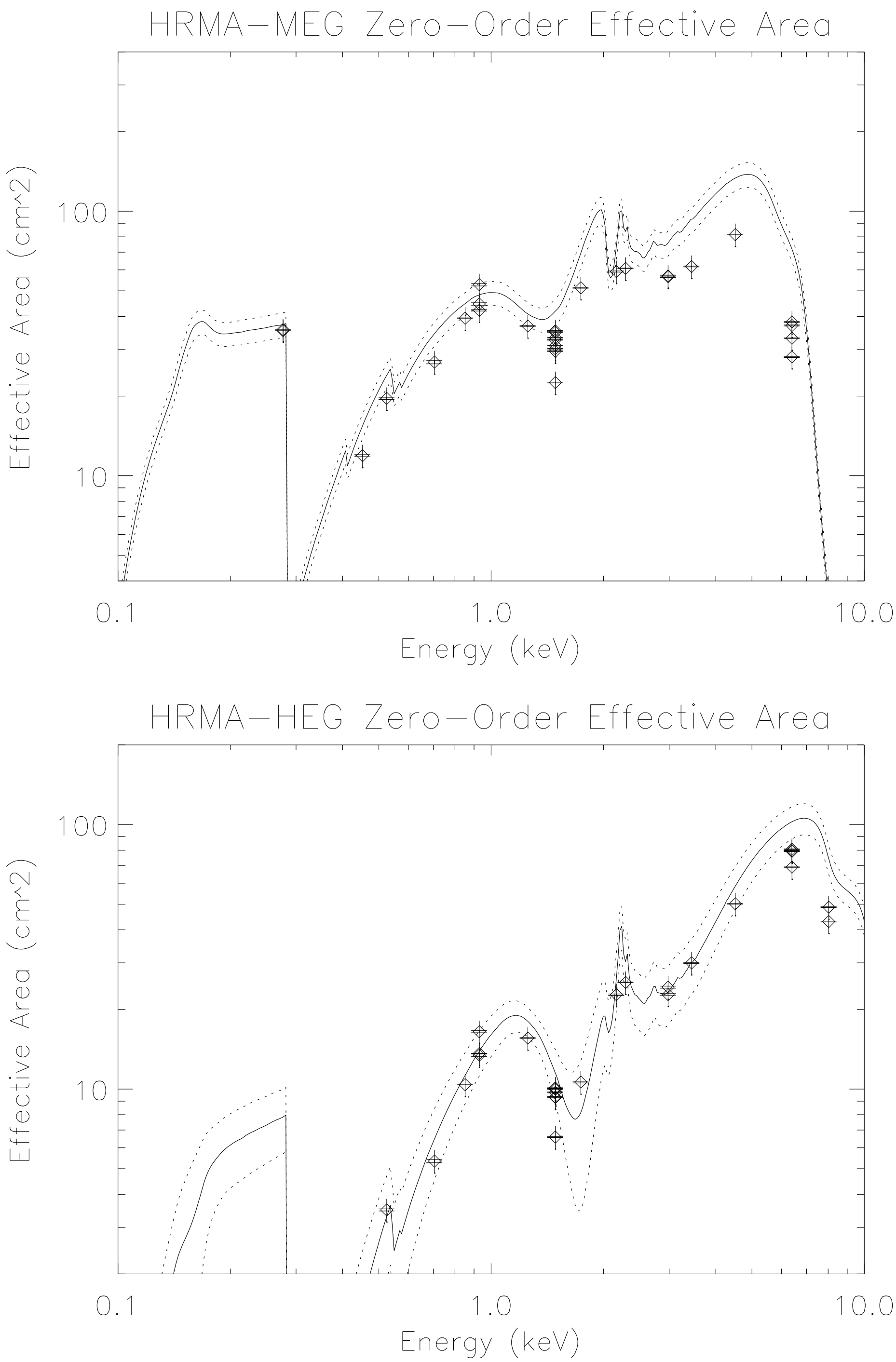

Figure 7.3: Preliminary Zero-order Optic Effective Area results for the HRMA-MEG (top) and HRMA-HEG (bottom) at XRCF. These plots represent the automated analysis of 88 fixed-energy data sets from Phase I. Because the zero-order is not dispersed, the effect of ignoring "line-fraction" corrections is not as severe as in the first-order case.

7.4.4 Grating Efficiency

The grating effective diffraction efficiency, Equation 1.5, is measured as the ratio of the optic effective area with the grating in place to the optic effective area without the grating:

$$G_{\text{config}}(E, m) = \frac{OEA_{\text{grating}}(E_{\text{line}}, m)}{OEA_{\text{HRMA}}(E_{\text{line}})} \tag{7.8}$$

Many of the terms of Equations 7.5 and 7.6 will cancel leaving only:

$$G_{\text{config}}(E, m) = \frac{\frac{R^g_{\text{fp}}(\text{mode}) \times L^g_{\text{fp}}(\text{aperture,spectrum}, QE_{fp})}{R^g_{\text{BND}}}}{\frac{R^H_{\text{fp}}(\text{mode}) \times L^H_{\text{fp}}(\text{aperture,spectrum}, QE_{fp})}{R^H_{\text{BND}}}} \tag{7.9}$$

Thus, the only corrections required to the efficiency measurements are for the line fraction terms in the focal plane detector.

7.4.5 Grating Efficiency Results

Using Equation 7.8 the grating effective efficiencies were derived from the previous optic effective area data. The results in Figures 7.4 and 7.5 show good agreement with the pre-XRCF efficiency predictions (solid curves).

7.4.6 Effective Area / Efficiency Analysis Software

The results presented here were automatically processed by a set of IDL procedures that used as input the CMDB, TRW ID to run id mapping, raw PHA data files, etc. The results were kept in a custom rdb database table. Please see the following web reference for details:

`http://space.mit.edu/HETG/eae/eae.html`

> *To-do:*
> Create s/w to estimate the L^g_{fp} and L^H_{fp} corrections using the measured grating-HSI source spectra.
> Work with MST and ASC to incorporate XSPEC fitting results.
> Repeat the auto analysis here using IDL Gaussian fitting plus a modeled continuum – as an XSPEC cross check.
> Validate all relevant CMDB entries used in the analysis.

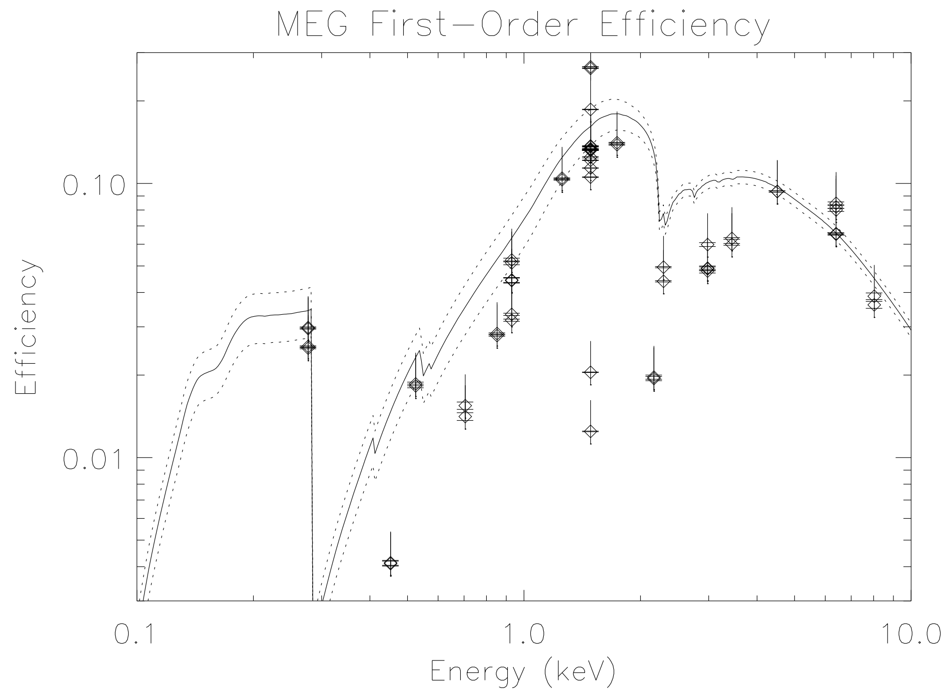

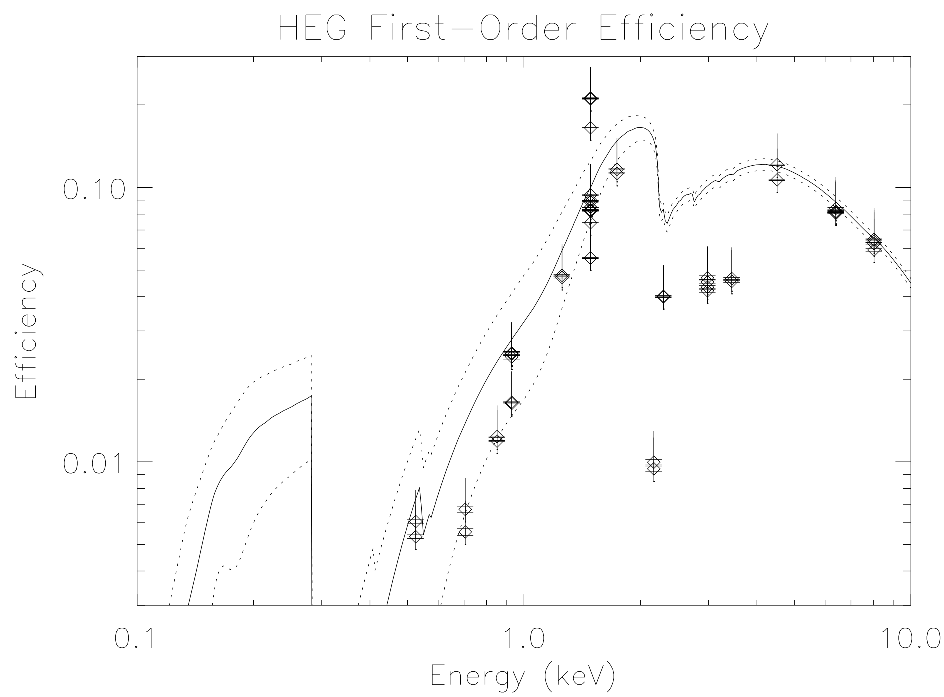

Figure 7.4: Preliminary XRCF MEG and HEG Efficiencies: 1st order. Because of the "ratio-of-ratios" nature of the efficiency measurement, there is good agreement with the laboratory predictions except for the L-lines where the "line-fraction" corrections are large; these L function corrections of Equation 7.5 were not included in this simple, first-pass analysis.
The solid curve is the model prediction, the dotted curves give an estimate of the error range for the prediction. The data points have horizontal lines to indicate the size of the statistical errors; the vertical lines indicate an estimate of the measurement systematic errors.

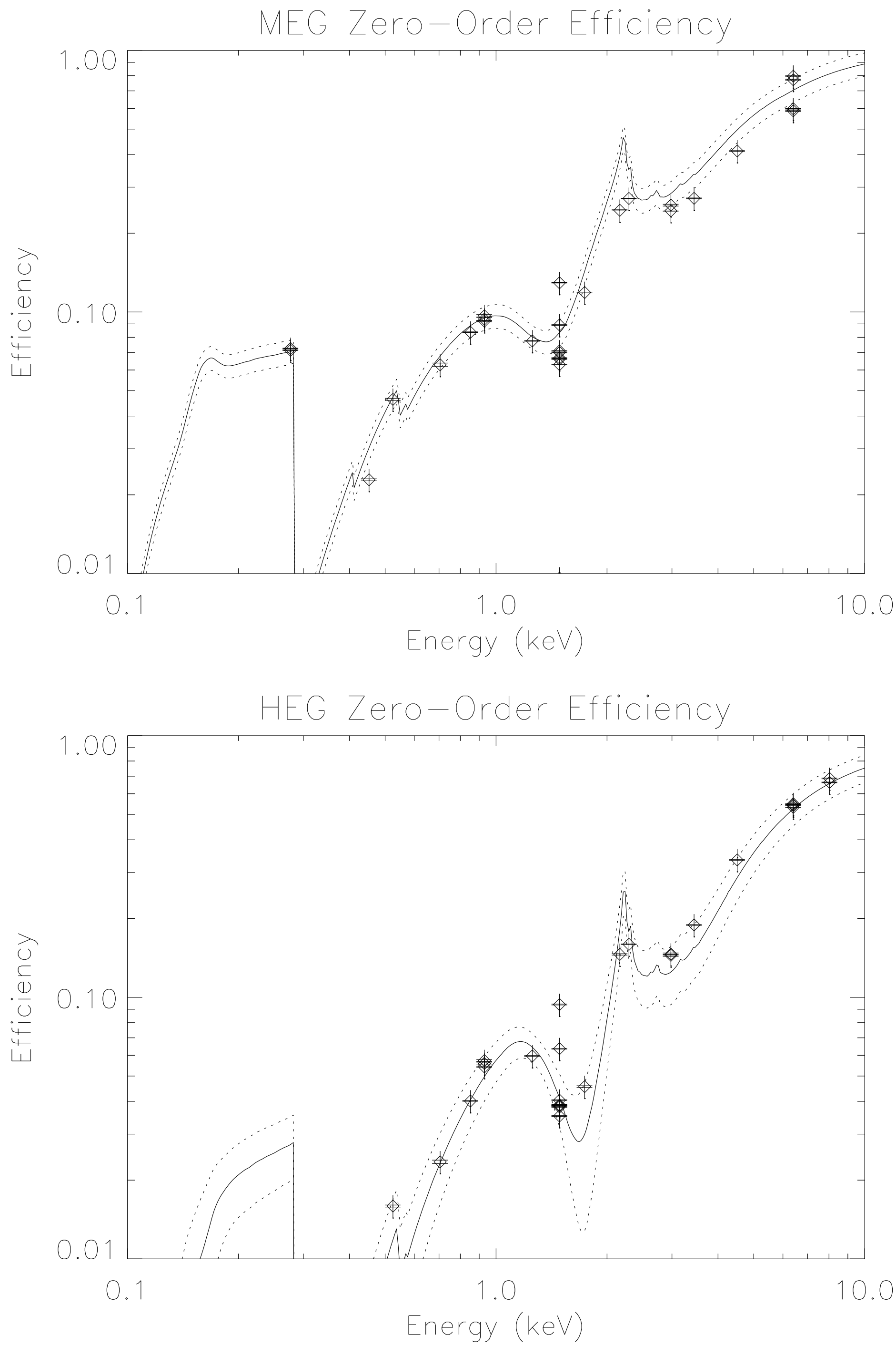

Figure 7.5: Preliminary XRCF MEG and HEG Efficiencies: 0 order. Because the zero-order is non-dispersed the L functions of Equation 7.5 will be nearly the same with and without the grating in place resulting in a clean measurement.

7.5 Efficiency: ACIS-2C Data

Objective: Derive the diffraction efficiency of the HEG or MEG using ACIS-2C "grating-in grating-out" measurements made at fixed (non-scanned, non-continuum) energies.

To-do:
Create automated analysis s/w similar to the Phase I Fixed energy analysis.
Generalize the rdb results table (eae_weffics.rdb) to include these '2C results, etc.

7.6 Efficiency: Phase 1, Monochromator Scans

Objective: Derive efficiencies of the HEG and MEG using the monochromator scan data.

7.7 Efficiency: Phase 2, Order Ratios

Objective: Calculate the relative efficiencies of the diffracted orders as seen in the Phase II flight detector data. This analysis is to calibrate the HETG order ratios.

During Phase II some 54 HRC-I and ACIS-S EA measurements were made with the HETG inserted in the beam.

7.7.1 DCM-HETG-HRC-I Efficiency Ratio

That the XRCF data will support a 3% relative and 10% absolute HETGS calibration is better domonstrated with a DCM-HETG-HRC data set, Figure 7.6. Here, the DCM was tuned to energies in the 1.5 to 7 keV range (TRW IDs G-HHI-EA-7.030 to '48, and '99.059 to '61). At each energy the ratio of counts detected in the HEG and MEG plus-first orders to the counts detected in the combined HEG and MEG zero order was computed. This ratio depends primarily on the HETG zero-order and first-order efficiencies and secondarily on the HRMA effective areas and the HRC-I spatial uniformity:

$$\frac{R_{1\mathrm{st}}}{R_0}(E) = \frac{QE_{\mathrm{HRC}}(E,\vec{X_M})\sum_{s=1,3}A_s(E)G_s(E,1) \quad + \quad QE_{\mathrm{HRC}}(E,\vec{X_H})\sum_{s=4,6}A_s(E)G_s(E,1)}{QE_{\mathrm{HRC}}(E,\vec{X_0})\sum_{s=1,3,4,6}A_s(E)G_s(E,0)} \tag{7.10}$$

where $QE_{\mathrm{HRC}}(E,\vec{X_*})$ is the quantum efficiency of the HRC-I at the different detected spatial regions (MEG 1st, HEG 1st, and zero orders) and the other terms have been previously defined.

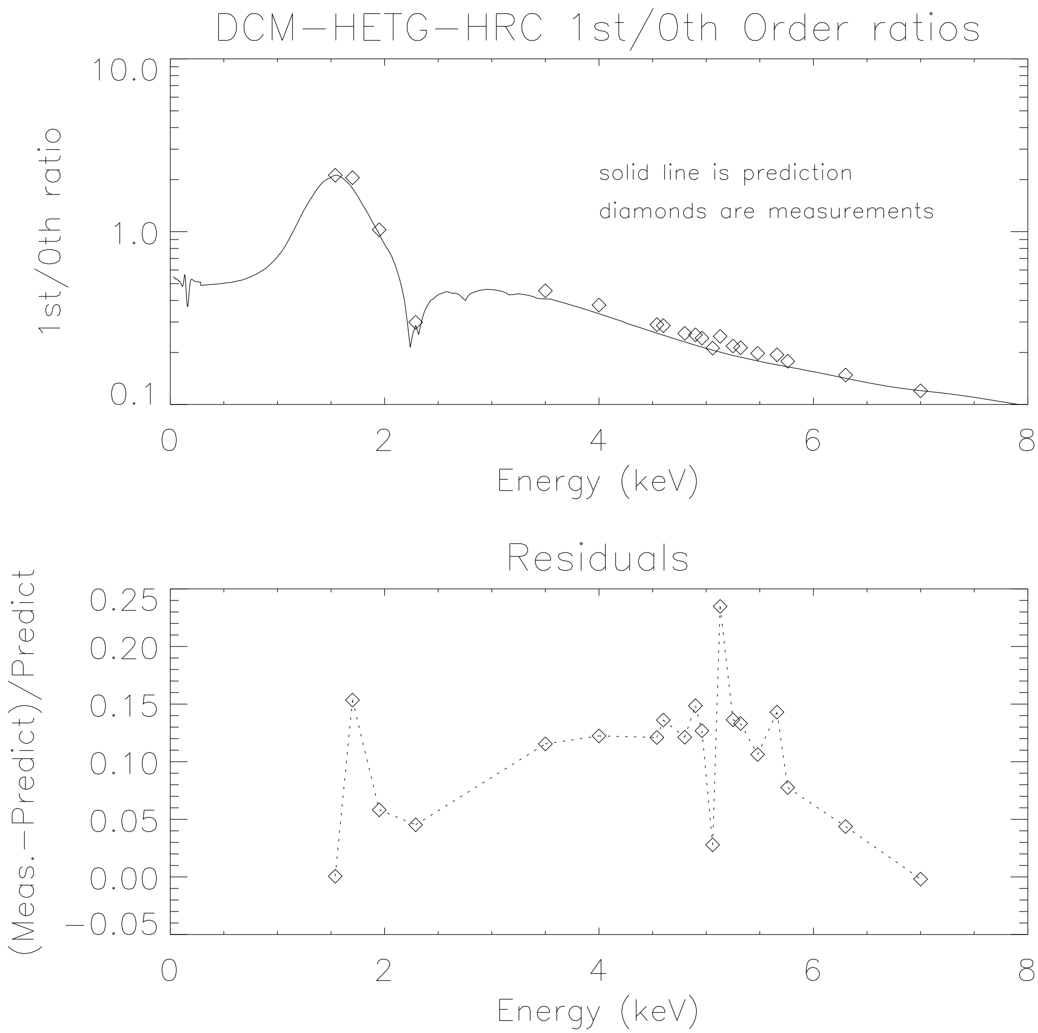

Figure 7.6: DCM-HETG-HRC data: ratio of first orders to zero-order.

7.8 Relative Effective Area: Molecular Contamination

Objective: Verify our detailed grating and detector spectral models and search for unexpected spectral features by observing a continuum source with the HETGS.

7.8.1 HETGS Molecular Contamination Result

The quasi-monochromatic energy measurements, *e.g.*, Figure 7.2, do not provide data at *all* energies. In order to verify our detailed grating and detector spectral models and to search for unexpected spectral features, we observed a continuum source with the HETGS. This type of test is called "molecular contamination" (MC) because of its ability to detect the effects of contaminating layers in the system components. Figure 7.7 shows the result of the analysis of a fraction of the MC data taken with the HETGS. The modeled source spectrum, continuum from a Carbon target, is expected to be smooth and featureless in the 1 keV to 10 keV range. In fact, emission lines due to trace contaminants on the source anode, *e.g.*, Al-K and W-M, are visible.

This MC data has also been put into a format allowing it to be fit by XSPEC (see also Section 9.4.3). Figures 7.8 to 7.12 show the data fit with an XSPEC power law and discrete lines.

With the full set of MC data we will be able to assess our knowledge of the relative effective area calibration of the HETGS over the full energy range.

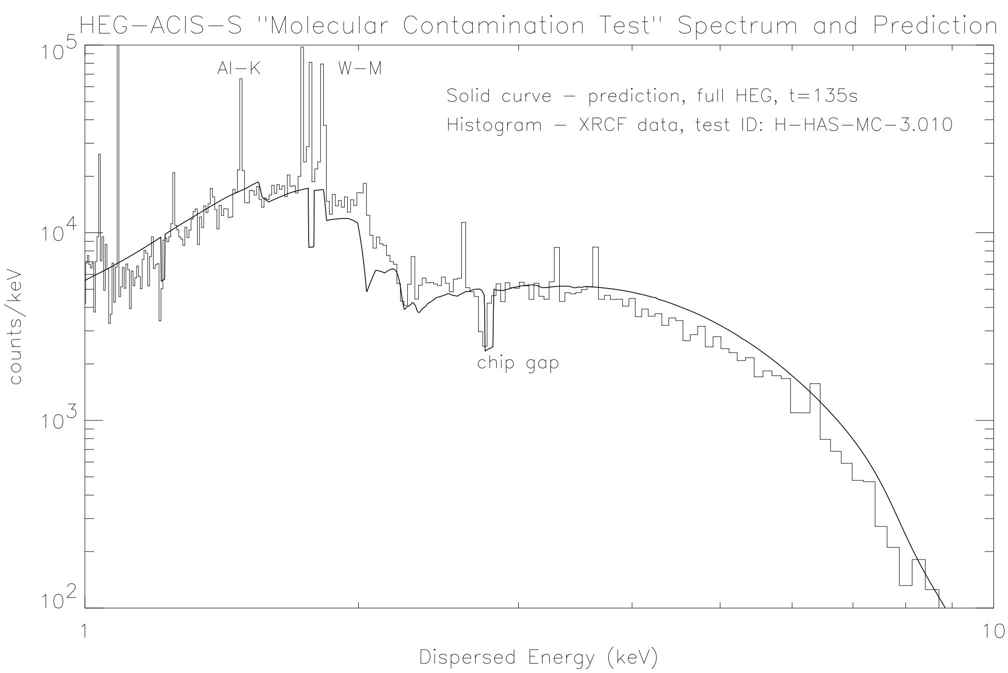

Figure 7.7: Molecular contamination data and prediction. An HEG-ACIS-S spectrum is taken with the XRCF source set to produce primarily continuum photons (C target, 15 kV). The resulting observed spectrum shows source-instrumental features. Using sub-assembly models a predicted curve is plotted where only the exposure time (normalization) and chip-gap location (aim point on the ACIS-S array) have been adjusted.

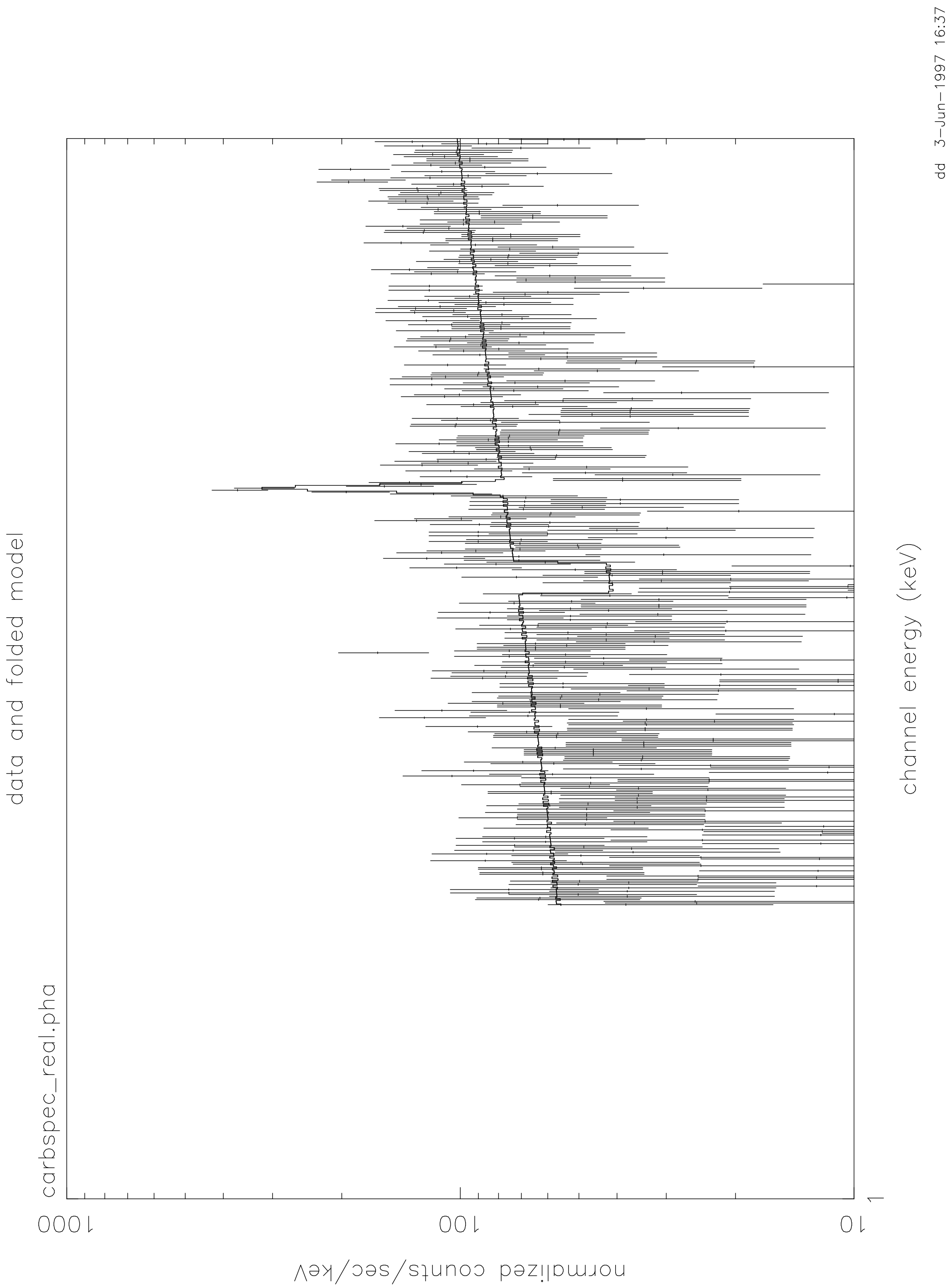

Figure 7.8: Molecular contamination spectrum, HEG-ACIS-S, 1-1.4 keV. Mg line at 1.253 keV is seen.

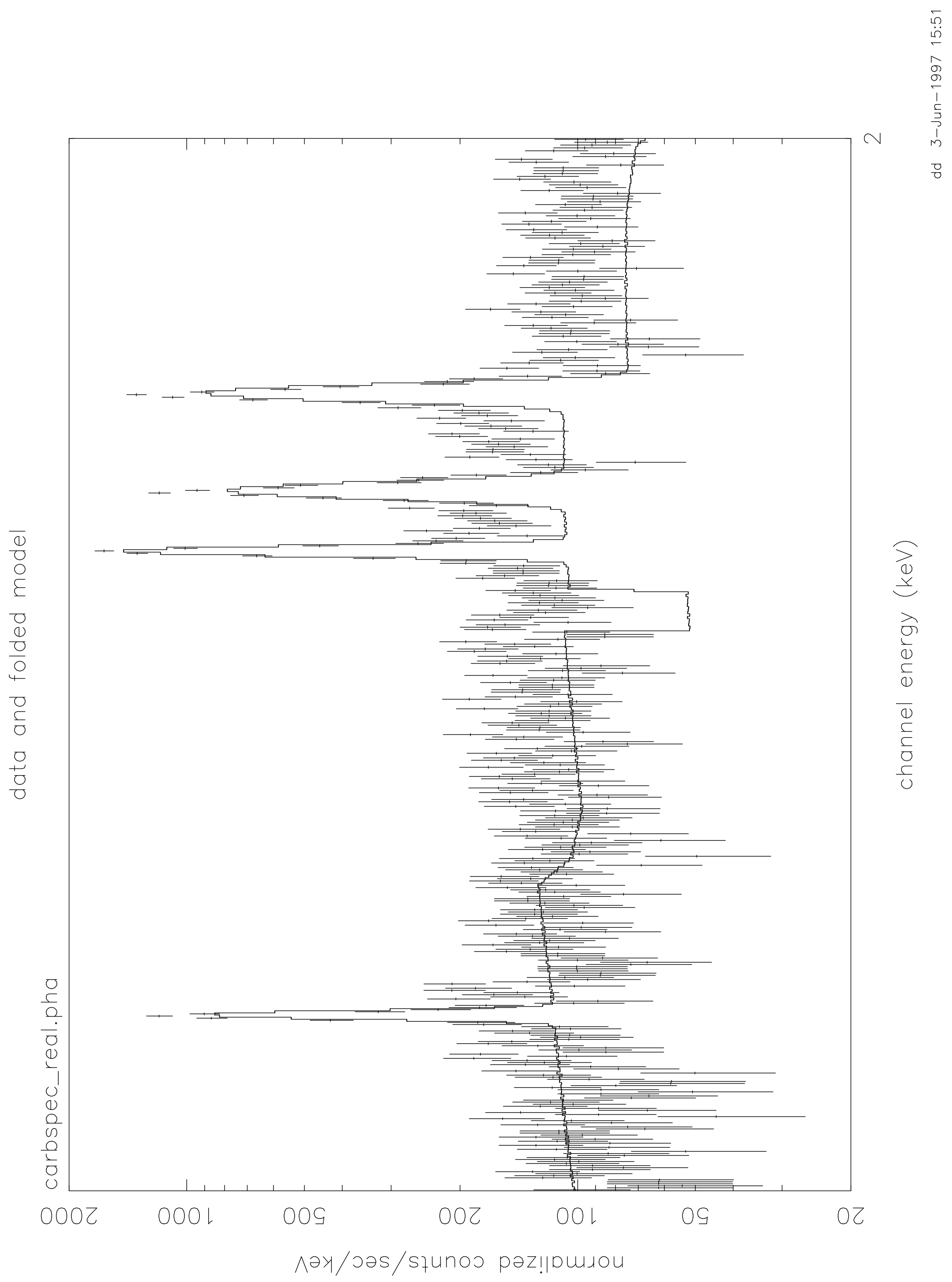

Figure 7.9: Molecular contamination spectrum, HEG-ACIS-S, 1.4-2 keV. Al-K line at 1.486 keV was used to set the energy scale. A "chip-gap" shows up in the modeled response just below the Si-K (1.739) and two W-M lines (1.775,1.839) - this gap is actually at the middle line (the line appears in one side order and not the other. The ACIS-S Si-K edge appears just after the W-M lines.

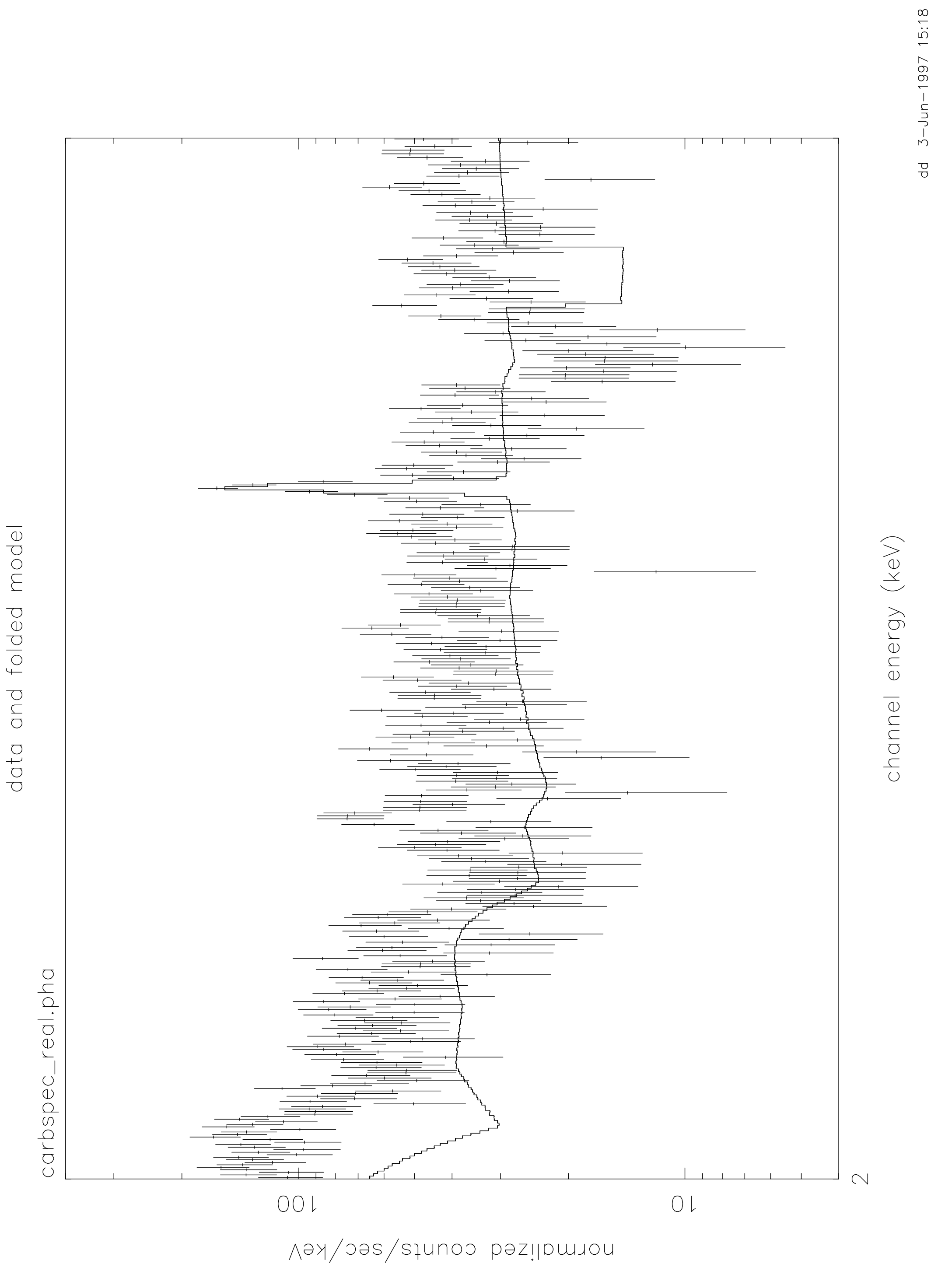

Figure 7.10: Molecular contamination spectrum, HEG-ACIS-S, 2-3 keV. Ir and Au edge structure dominate here – the modeled response and the real response are significantly different just above 2 keV. There is probably a Mo line (2.293 keV) that was not included in the model. The line at 2.618 is certainly Cl-K (listed as 2.622 keV). The modeled vs real location of the chip gaps is clearly seen here just below 3 keV.

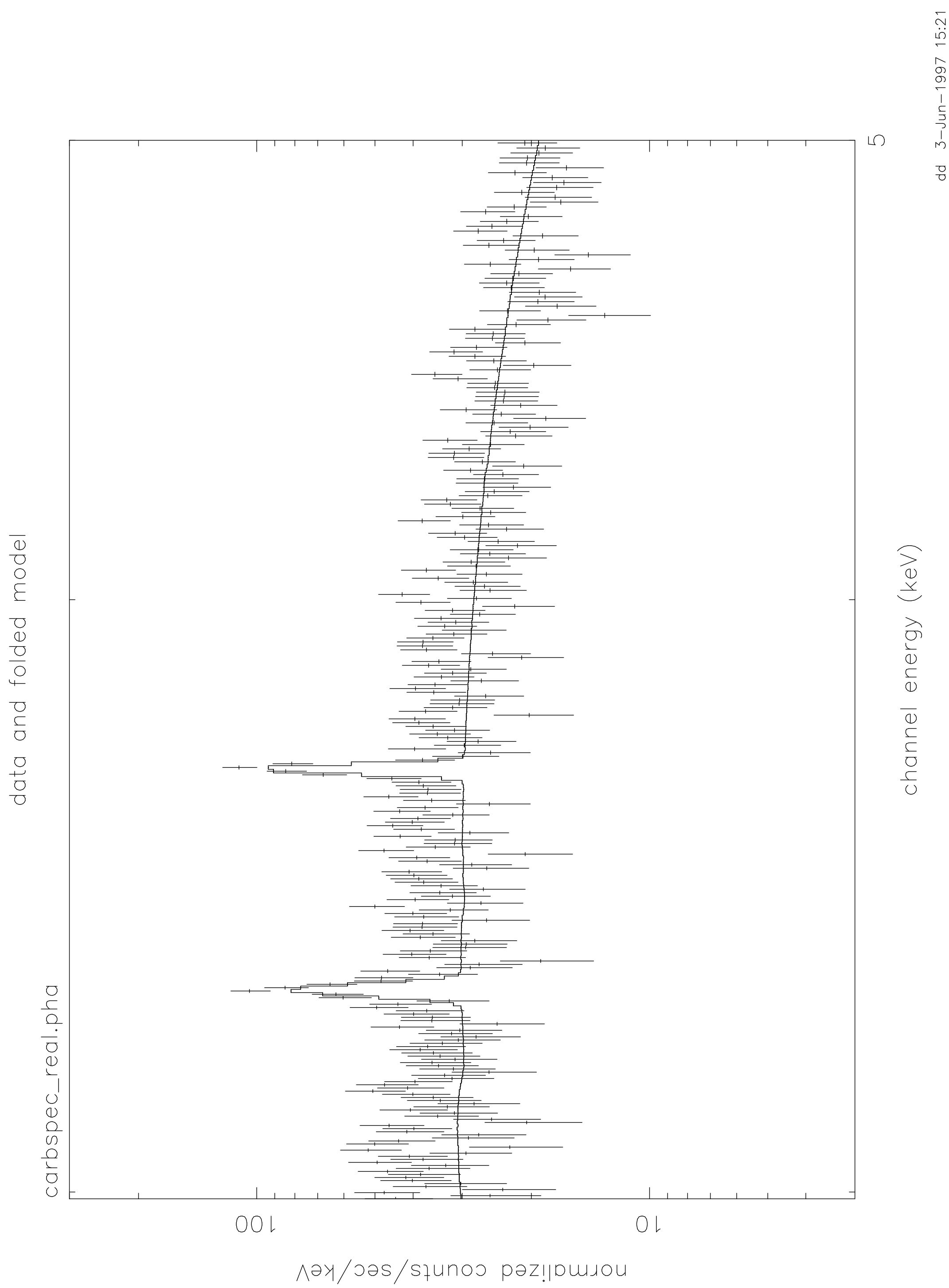

Figure 7.11: Molecular contamination spectrum, HEG-ACIS-S, 3-5 keV. These two lines (measured at 3.309, 3.684) are identified with K-K (3.313) and Ca-K (3.691).

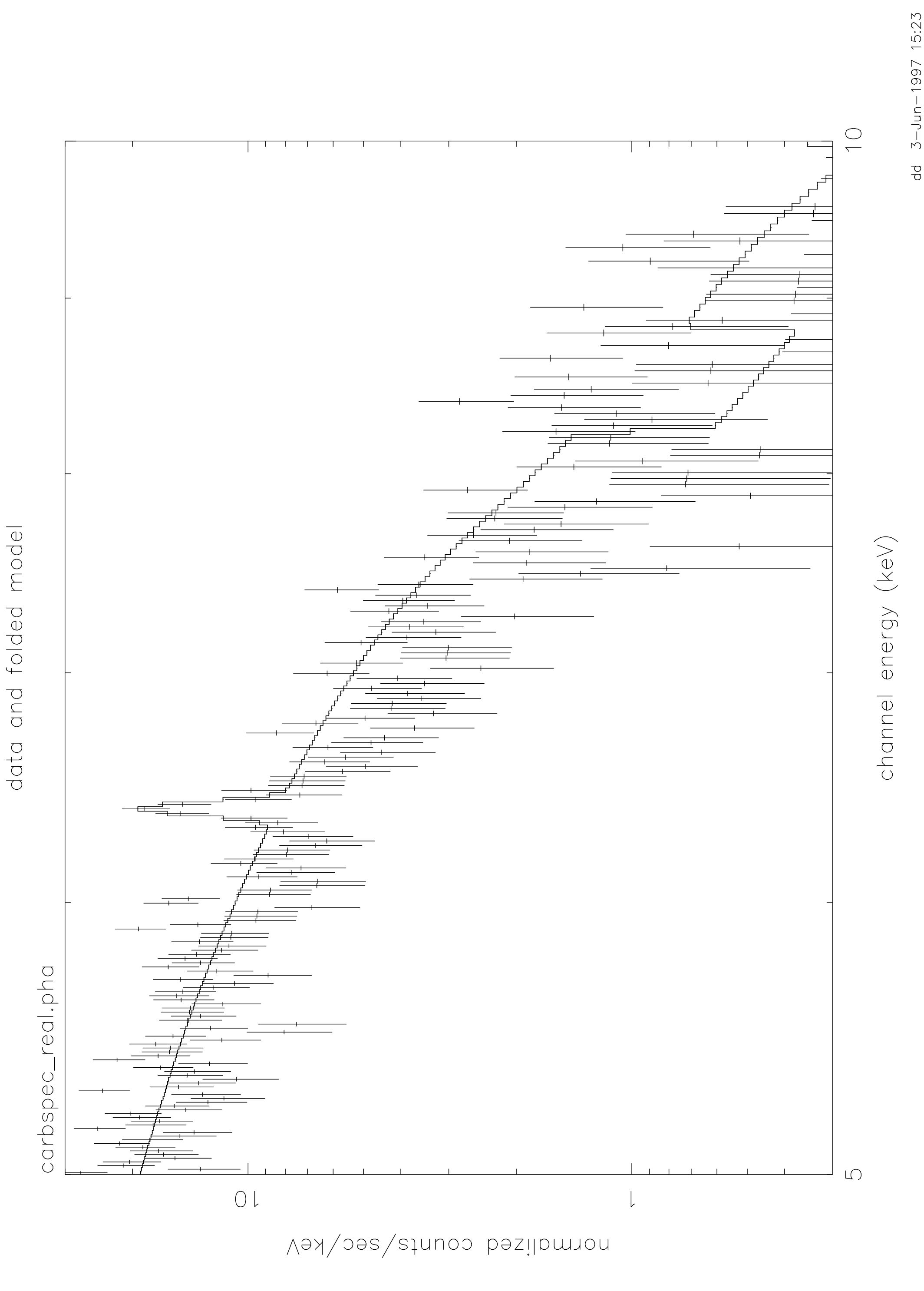

Figure 7.12: Molecular contamination spectrum, HEG-ACIS-S, 5-10 keV. Fe-K is seen at 6.391 keV. The S2-S3 chip gap shows up in the predicted response.

7.9 Effective Area with ACIS-S

Objective: Derive the HETGS(ACIS-S) effective area and compare it to HRMA, HETG, and ACIS-S measurements and predictions. ACIS effects that must be understood include: pileup, grade effects, exposure times.

7.10 Effective Area with HRC-I

Objective: Derive the HETGS(HRC-I) effective area and compare it to HRMA, HETG, and HRC-I measurements and predictions. HRC-I effects that must be understood include: quantum efficiency, quantum efficiency, and quantum efficiency.

Part III

Calibration Data and Products

Section 8

Calibration Data

8.1 Synchrotron Data

8.2 HETG Facet Data

8.3 LR Data

8.4 X-GEF Data

8.5 HESS Design and Metrology Data

8.6 Alignment Data

8.7 XRCF Data

Section 9

Calibration Products

9.1 Overview of Products

This section provides a general overview to the types of calibration products, the next sections provide the HETG and HETGS products themselves.

Calibration Data are all the raw data acquired that has information to constrain the instrument models; these are the basis of a calibration.

Calibration Measurement Products are the specific results from specific manipulations of the Calibration Data and cover many levels of complexity. They represent the results when the raw data have been "analyzed" to create something, *e.g.*, "counts per second in the Al-K BND bump", "ACIS-I 5 arc min Mo-L off-axis encircled-energy curve", or "witness flat reflectivity at 8.04 keV". There are lots of these! And their meaning and organization and synthesis can require a lot of human knowledge. Many results may be ammenable to database storage, others may require memos to describe and define them. Error estimates are produced for each measurement result as well.

Fundamental Calibration Products are the most detailed "encoding" of the calibration activity into detailed (complex) models, *e.g.*, SAOSAC as a model of the HRMA. This requires a synthesizing by calibrationists of the various Calibration Measurement Products and model expectations.

Calibration Interface Products are specific, well-defined, useful parameters, tables, models which describe the essence of the instrument to sufficient accuracy to be useful yet in a more accessible form than the Fundamental Calibration Products. (The distinction is blurred and need not be too strict. For example the ACIS pixel size is about as Fundamental as can be yet it is also a very useful CIP value.) These CIPs are the main interface between the calibration activity and the rest of the system.

Analysis Reference Data is used to explicitly identify those data that are needed and used by, *e.g.*, the ASC Data System for simulation and data analysis. The formats are dictated by the analysis algorithms and software architecture; often these data may be simply reformatted versions of the CIPs. The **MARX** parameters, Section 9.3.5, are a good example of Analysis

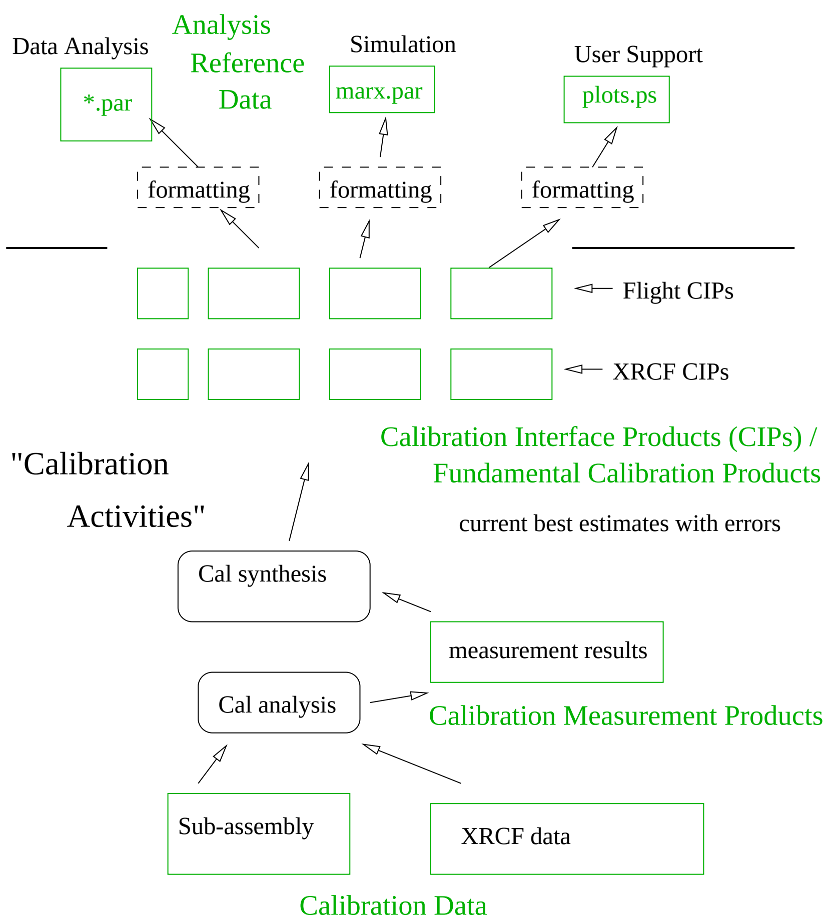

Figure 9.1: Schematic Diagram of the Types of Calibration Products

Reference Data.

The relationship of these products is schematically shown in Figure 9.1.

9.2 Fundamental Calibration Products for HETG

As we have seen, the LRF functions depend not only on shell-level quantities but on grating-level data, *e.g.*, grating mis-alignment angles[32]. For this reason, *the fundamental HETG calibration or model is at the grating facet level.*

For each grating facet, $f = 1$ to 336, we have a diffraction efficiency $g_f(E, m)$, period map in facet coordinates $p_f(x, y)$, and alignment distribution $\Gamma_f(\phi_{\rm roll})$ as well as mechanical parameters. These fundamental data can be combined with other information to produce, *e.g.*, ν_s, $G_s(E, m)$, $SEA(E, m, \ldots)$, and $LRF(E, m, \ldots)$.

9.3 HETG Calibration Interface Products

A discussion of and values for the HETG CIPs are presented here; data files, discussions, and updates are available at `http://space.mit.edu/HETG/xrcf.html` under "Calibration Products".

9.3.1 Basic Parameters

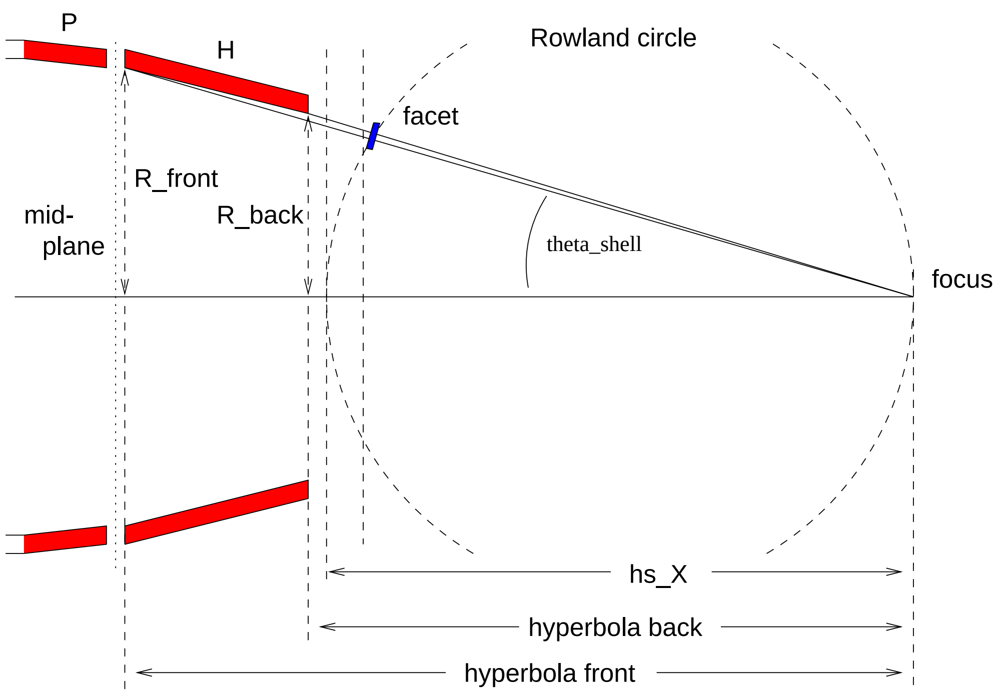

Figure 9.2: Basic Geometry for HETG Facet Location

Basic parameters of the HETG design are tabulated in the file `HETGbasic.rdb` for computer input and reproduced here in Table 9.1. The HETG radii given here are really a method to record the angle of the central ray through the shell's facets, "theta_shell" in Figure 9.2:

$$\tan\theta_s \;=\; \mathrm{HETGrad}_s \;/\; \mathrm{HETGrd} \qquad (9.1)$$

To-do:
Produce and include reference to 3-D facet location information.

name	value	error	unit
HETGrd	8633.69	0.1	mm
HETGrad1	521.66	0.1	mm
HETGrad3	419.90	0.1	mm
HETGrad4	370.66	0.1	mm
HETGrad6	275.44	0.1	mm
HETGvign1	0.937	0.01	none
HETGvign3	0.940	0.01	none
HETGvign4	0.931	0.01	none
HETGvign6	0.936	0.01	none

Table 9.1: Basic HETG Design Parameters, from `HETGbasic.rdb`.

9.3.2 Periods, Angles, and Spacing

Periods

Lab measurements were made on the flight gratings for HETG as well as on the TOGA gratings used in XRCF rehearsal. These laboratory measurements were corrected based on NIST-measured reference samples (Section 4.1.2) resulting in our best estimate "LR-NIST" periods.

The current CIP adopted periods (in Å) are the sub-assembly values because XRCF measurements are not accurate enough to require a change. In particular a spacing discrepancy still exists, Section 6.2. The period errors are all taken as the sub-assembly values, again because (with an HETG displacement assumption) XRCF measurements are in agreement and do not provide any smaller error bounds.

Angles

The mean dispersion angles have been measured at XRCF and the HETG opening angle should be the same for XRCF and flight. The flight clocking and grating angles have been modified slightly from the XRCF values by the as-installed +46 arc second HETG roll.

Spacing

The HEG/MEG period difference seen between sub-assembly (HeCd,HeNe) and XRCF-AL-K (assuming a spacing of 8788.04 mm) of about 500 ppm is assumed to be due to an inaccurate value for the HETG Rowland spacing at XRCF, Section 5.2.1. Thus, for now the HETG position at XRCF is set to be 8782.8 mm to have reasonable agreement between XRCF and sub-assembly periods (and hence calculated line energies). The cause for the (alleged) displacement has not been determined.

For flight spacing, Scott Texter reports that EK measures (mechanical means) the as-installed HETG to be 0.009 inches closer to the HRMA than designed, so expected flight spacing is 8633.69+0.009*25.4 = 8633.92 mm. The error on this is probably 0.2 mm or less (HRMA-grating spacing). However the HRMA-focus spacing may still have error of order 0.5 mm.

name	value	error	unit
HEGp	2000.81	0.05	Angstrom
MEGp	4001.41	0.10	Angstrom
HETGrsX	8782.8	0.50	mm
HETGrsF	8633.92	0.50	mm
HETGopenX	9.934	0.008	degrees
HETGopenF	9.934	0.008	degrees
HETGclockX	-0.225	0.05	degrees
HETGclockF	-0.215	0.05	degrees
HEGangleX	-5.19	0.05	degrees
MEGangleX	4.74	0.05	degrees
HEGangleF	-5.18	0.05	degrees
MEGangleF	4.75	0.05	degrees

Table 9.2: HETG Period, Angle, and Spacing Parameters, from `HETGperiod.rdb`.

9.3.3 Period and Roll Variation Parameters

A coarse characterization of the gratings LRF effect is with the period and roll variations, listed as dp/p and γ in the error budget of Table 2.2. These values are measured in the laboratory by the LR and Alignment setups. Confirmation of these laboratory values at XRCF with the XRCF LRF Core analysis has only begun, Section 6.3.

The MEG mis-aligned gratings have pointed out a mechanism whereby the alignment measurement differs from the actual grating bar orientations. It is likely that the same effect operating at a lower and randomized level will lead to an increase in the actual γ value over the alignment system determined one. A simple analysis of one XRCF data set suggests that γ may be between 1 or 2 arc minutes rms, hence a value of 1.5 arc minutes (with a large 0.5 arc minute error) is being adopted preliminarily.

As for the period variations, the LR predictions of 127 ppm and 106 ppm, Figures 4.3 and 4.4, are a lower limit to these variations. Again the limited XRCF analysis has not produced a precise value but suggests $dp/p < 300$ ppm. Unlike the alignment effect, there is currently no expectation that the dp/p measured by the LR is in error, so the proposed baseline values are the LR values increased by rss'ing them with 100 ppm to account for any mounting induced distortions.

name	value	error	unit
HEGdpop	146.	50.	ppm
MEGdpop	162.	50.	ppm
HEGroll	1.5	0.5	arc minutes
MEGroll	1.5	0.5	arc minutes

Table 9.3: Parameters Effecting the HETG LRF Core, from `HETGcore.rdb`.

9.3.4 Efficiency Products

Table 9.4 lists the available files that contain the current best estimates of the HETG diffraction efficiency, $G_s(E, m)$, for $m = -11, \ldots, +11$; note that error files are available as well. These files have equal plus and minus orders and include the shell vignetting ν_s factor. Samples of this data are plotted in Figures 9.3 and 9.4.

Shell	Data File	Error File
1	HETG_shell1_effic.rdb.gz	HETG_shell1_effic_err.rdb.gz
3	HETG_shell3_effic.rdb.gz	HETG_shell1_effic_err.rdb.gz
4	HETG_shell4_effic.rdb.gz	HETG_shell1_effic_err.rdb.gz
6	HETG_shell6_effic.rdb.gz	HETG_shell1_effic_err.rdb.gz
MEG	MEG_effic.rdb.gz	MEG_effic_err.rdb.gz
HEG	HEG_effic.rdb.gz	HEG_effic_err.rdb.gz
HETG	HETG_effic.rdb.gz	HETG_effic_err.rdb.gz

Table 9.4: CIP Efficiency Files for the HETG, available from
`http://space.mit.edu/HETG/cal_prods.html/#HETG_CIP`

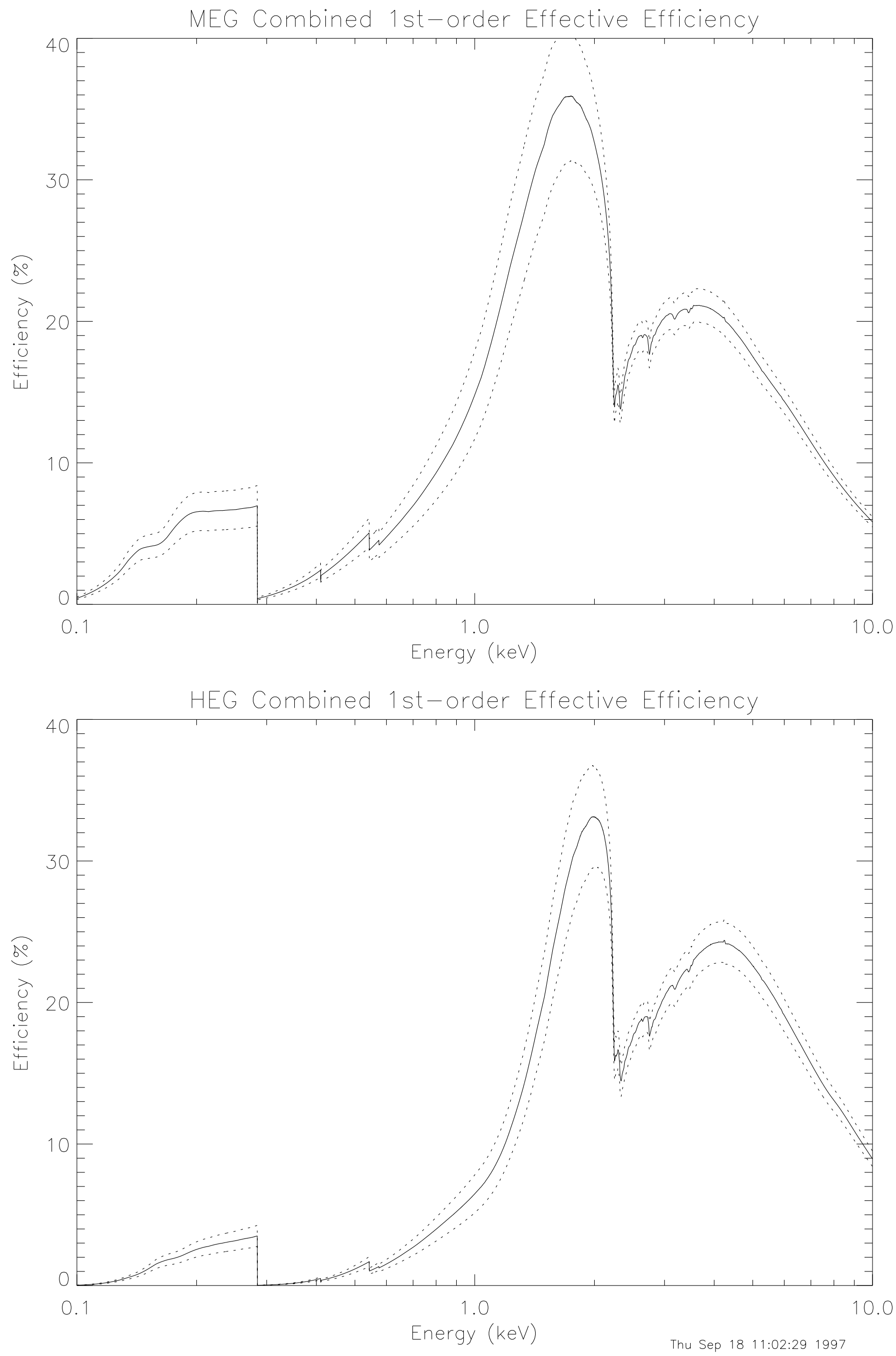

Figure 9.3: Effective Efficiency for First-order MEG and HEG. These efficiencies are the mirror weighted average of the shell-by-shell efficiencies for the appropriate pair of shells. Plus and minus orders have been combined. The dotted lines are the "2-sigma" errors of the shell efficiencies with additional error due to uncertainties in the relative area (weighting) of the HRMA shells.

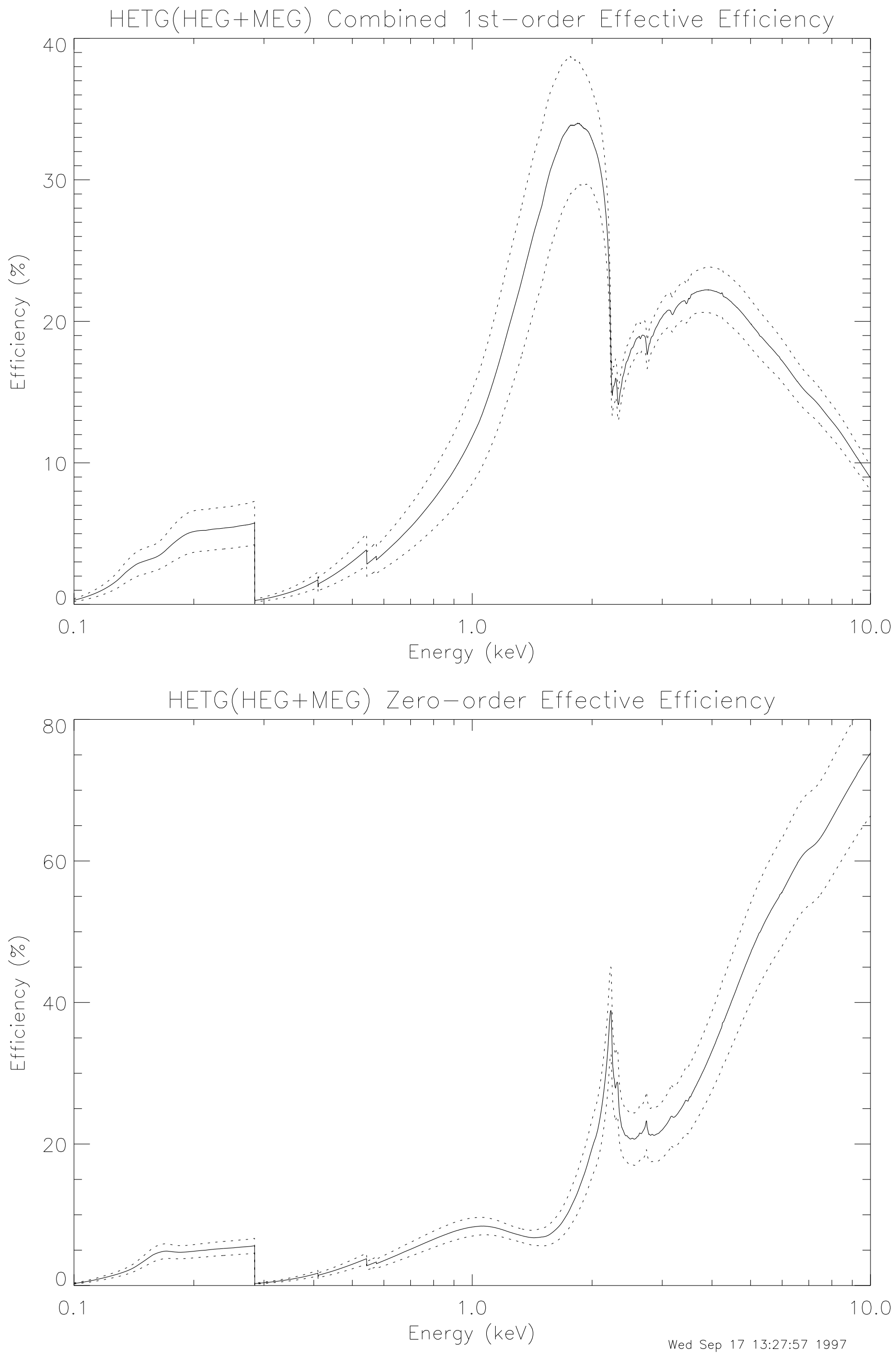

Figure 9.4: Effective Efficiency for HETG 1st and 0 orders. These efficiencies are the mirror weighted average of the shell-by-shell efficiencies. The first-order efficiency is for combined plus and minus orders for HEG and MEG. The dotted lines are the "2-sigma" errors of the shell efficiencies with additional error due to uncertainties in the relative area (weighting) of the HRMA shells.

9.3.5 MARX Parameters

The **MARX** ray-trace package, Section 2.3, provides a high fidelity model of the HETGS. To define the HETG in **MARX** there are parameters and data files to be specified. It is the HETG and ASC calibration groups domain, working with the **MARX** developers, to provide accurate values for these **MARX** inputs.

The **MARX** inputs can be divided into those directly related to the LRF and those that govern diffraction efficiency. These are presented in the following sections.

9.3.5.1 MARX HETG LRF Parameters

The LRF parameters bascially encode the Rowland design and some aspects of its real-life construction. The values presented in Table 9.5 are all taken directly from the corresponding values determined in the CIP Sections 9.3.1 through 9.3.3. Note that the MEG mis-aligned gratings and the HEG scatter are not currently included in **MARX** simulations.

Table 9.5: Flight HETG LRF parameters for use in **MARX**.

Parameter	Value	Unit
RowlandDiameter	8633.75	mm
hegTheta	-5.18	degrees
megTheta	4.75	degrees
HETG_Shell1_Theta	4.75	degrees
HETG_Shell3_Theta	4.75	degrees
HETG_Shell4_Theta	-5.18	degrees
HETG_Shell6_Theta	-5.18	degrees
hegdTheta	1.5	arc minutes rms
megdTheta	1.5	arc minutes rms
HETG_Shell1_dTheta	1.5	arc minutes rms
HETG_Shell3_dTheta	1.5	arc minutes rms
HETG_Shell4_dTheta	1.5	arc minutes rms
HETG_Shell6_dTheta	1.5	arc minutes rms
hegPeriod	0.200081	microns
megPeriod	0.400141	microns
HETG_Shell1_Period	0.400141	microns
HETG_Shell3_Period	0.400141	microns
HETG_Shell4_Period	0.200081	microns
HETG_Shell6_Period	0.200081	microns
hegdPoverP	146.e-6	rms
megdPoverP	162.e-6	rms
HETG_Shell1_dPoverP	162.e-6	rms
HETG_Shell3_dPoverP	162.e-6	rms
HETG_Shell4_dPoverP	146.e-6	rms
HETG_Shell6_dPoverP	146.e-6	rms

9.3.5.2 MARX Rectangular Efficiency Parameters

MARX offers two ways to specify a gratings diffraction efficiency. The old standby is a rectangular grating model in which a few parameters are used to specify a rectangular model and the diffraction efficiency $G_{\rm config}(E, m)$ is calculated from these parameters. The second method is to use a set of look up tables for the efficiency, described in the next section.

Although the HETG gratings are not rectangular and also vary in their properties, it is possible to select a set of rectangular parameters that comes close to approximating the effective efficiencies of Section 9.3.4. Figures 9.5–9.8 present comparisons of these rectangular efficiencies and the current best CIP values. The first-order effective efficiencies are modeled to better than 10% over the relevant ranges; orders $m = 0, 2, 3$ are largely within 20% . The rectangular parameters used in these plots are presented in Table 9.6.

Table 9.6: **MARX** Parameters for Rectangular approximation to HETG efficiency. These (non-physical) parameters provide a reasonable approximation to the HETG diffraction efficiency including higher-order contributions.

Parameter	Value	Unit
GratingOptConsts	“optical-constants.dat”	
UseGratingEffFiles	“‘no”	
HEG grating		
HEGVig	0.93	
hegGold	0.0444	microns
hegChromium	0.0111	microns
hegNickel	0.0	microns
hegPolyimide	0.978	microns
hegBarHeight	0.4896	microns
hegBarWidth	0.1177	microns
MEG grating		
MEGVig	0.93	
megGold	0.0228	microns
megChromium	0.0057	microns
megNickel	0.0	microns
megPolyimide	0.543	microns
megBarHeight	0.3780	microns
megBarWidth	0.2161	microns

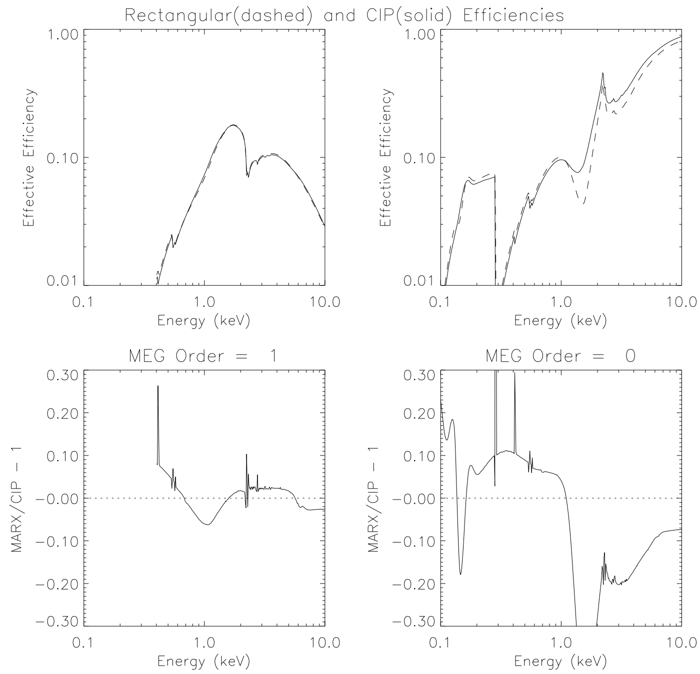

Figure 9.5: Comparing MEG Rectangular and CIP Efficiencies (orders 1, 0).

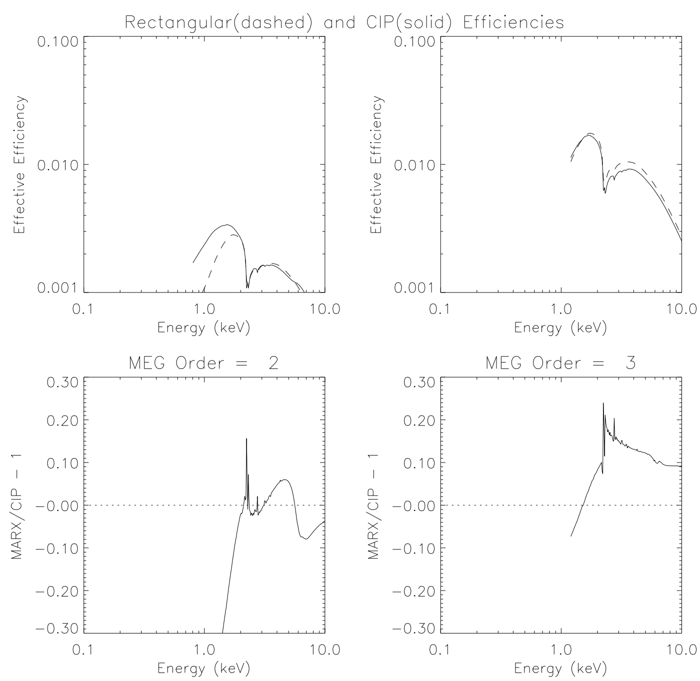

Figure 9.6: Comparing MEG Rectangular and CIP Efficiencies (orders 2, 3).

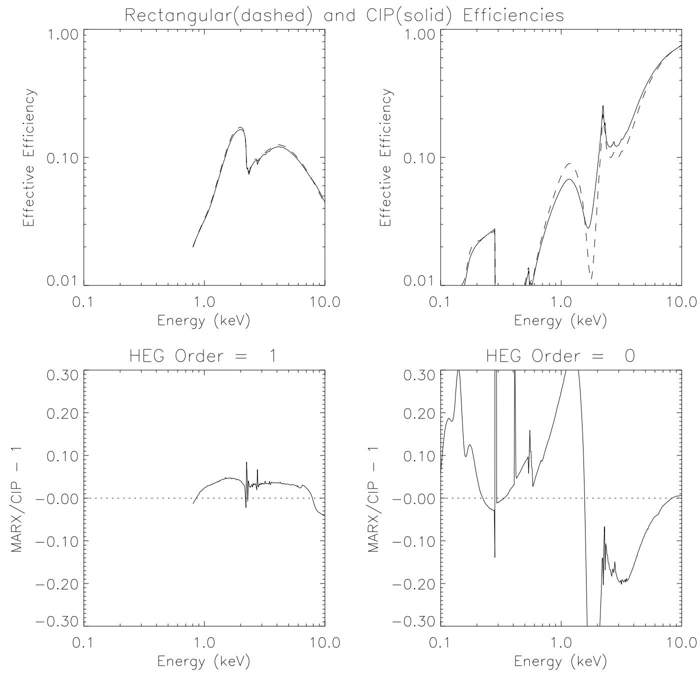

Figure 9.7: Comparing HEG Rectangular and CIP Efficiencies (orders 1, 0).

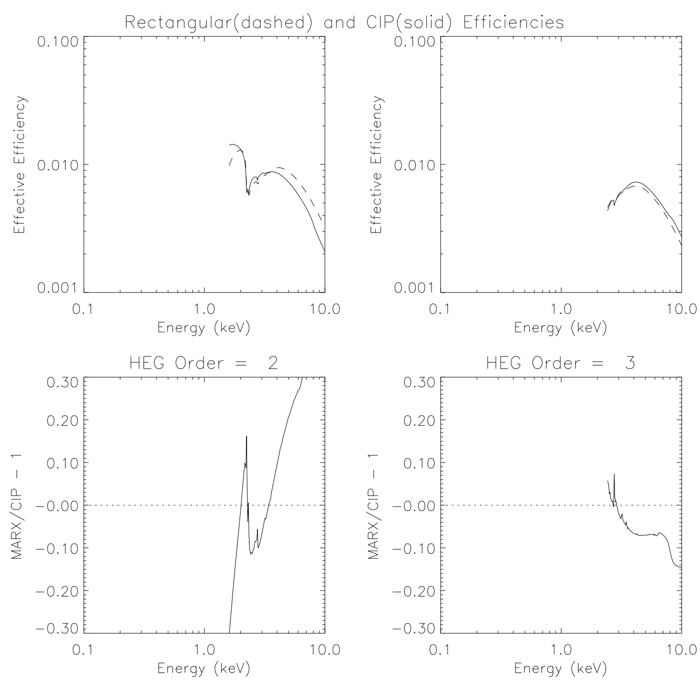

Figure 9.8: Comparing HEG Rectangular and CIP Efficiencies (orders 2, 3).

9.3.5.3 MARX Efficiency Files

MARX will soon allow the option of providing grating efficiecies as a set of lookup tables, one file for each shell. The efficiencies are tabulated on a fine energy grid and for a range of orders, currently $m = -11, \ldots, +11$. These tables of $G_s(E, m)$ include the shell vignetting factors (ν_s) and so the grating vignetting terms in **MARX** are set to 1.0. Table 9.7 presents the set of parameters that need to be set to implement the table lookup HETG efficiencies.

Table 9.7: **MARX** Parameters for Table-lookup HETG Efficiencies. These parameter selections allow efficiency tables encoding $G_s(E, m)$ to be read in and used by **MARX** for accurate simulations.

Parameter	Value	Unit
UseGratingEffFiles	"'yes"	
HETG_Shell1_File	"HETG_shell1_effic.dat"	
HETG_Shell3_File	"HETG_shell3_effic.dat"	
HETG_Shell4_File	"HETG_shell4_effic.dat"	
HETG_Shell6_File	"HETG_shell6_effic.dat"	
HETG_Shell1_Vig	1.0	
HETG_Shell3_Vig	1.0	
HETG_Shell4_Vig	1.0	
HETG_Shell6_Vig	1.0	

9.4 HETGS Calibration Interface Products

9.4.1 Resolving Power

Using the resolving power error budget described in Section 2.2, estimates of the flight HETGS resolving power have been made, Figure 2.2. The "optimistic" and "conservative" E/dE curves are available in rdb format in the files:

```
MEG_res_opt.rdb
HEG_res_opt.rdb
MEG_res_con.rdb
HEG_res_con.rdb
```

9.4.2 Effective Area

In order to compute the HETGS effective area, the HRMA effective area, $A_s(E)$, and the ACIS-S quantum efficiencies, $QE_{\mathrm{ACIS}}(E, \mathrm{grade\ set})$, are needed and should be available soon.

9.4.3 XSPEC Response Matrices

Please see `http://space.mit.edu/HETG/xspec/xspec.html` for a discussion of HETG and XSPEC.

Acronyms

	Sec.	
ACIS	1.1	AXAF CCD Imaging Spectrometer
ACIS-I		ACIS Imaging array
ACIS-S		ACIS Spectroscopic array
ACIS-2C	5.1.6	ACIS “2-chip” detector
ARD	9.1	Analysis Reference Data
ARM		Alignment Reference Mirror
ASC		AXAF Science Center
AXAF		Advanced X-Ray Astrophysics Facility
BESSY	3.2.4	Berlin Synchrotron Facility
BNDs	5.1.2	Beam Normalization Detectors
CCD		Charge Coupled Device
CEI	2.2	Contract End Item (specifications)
CIP	9.1	Calibration Interface Product
CMDB	5.3	Calibration Measurement Database
DCM	5.1.1	Double Crystal Spectrometer
EA	5.3.1	Effective Area
EE	6.2	Encircled Energy
FC	6.3	Focus Check
FCP	9.1	Fundamental Calibration Product
FITS		Flexible Image Transport System
FPC	5.1.5	Flow Proportional Counter
FWHM	1.3.3	Full Width at Half Maximum
HEG	1.2	High Energy Grating
HESS	1.2	HETG Element Support Structure
HETG	1.1	High Energy Transmission Grating
HETGS	1.3	High Energy Transmission Grating Spectrometer
HIREFS	5.1.1	High-Resolution Erect Field Spectrometer
HRMA	1.1	High Resolution Mirror Assembly
HRC	1.1	High Resolution Camera
HRC-I		HRC Imaging array
HRC-S		HRC Spectroscopic array
HSI	5.1.4.2	High Speed Imager
HXDS	5.1.4	HRMA X-Ray Detection System
LEG	1.1	Low Energy Grating
LETG	1.1	Low Energy Transmission Grating
LR	4.1	Laser Reflection setup at MIT
LRF	1.3.3	Line Response Function
MARX	2.3	Model of AXAF Response to X-rays
MC	7.8	Molecular Contamination

	Sec.	
MEG	1.2	Medium Energy Grating
MIT		Massachusetts Institute of Technology
MST		Mission Support Team at SAO
NSLS	3.2	National Synchrotron Light Source (Brookhaven)
PIGS	5.1.1	Penning Ionization Gas-discharge Source
PSF	1.3.3	Point Spread Function
PSPC	4.2	Position Sensitive Proportional Counter (in X-GEF)
rms		(square)root of the mean of the squares
rss		(square)root of sum of squares
SAO		Smithsonian Astrophysical Observatory
SF	6.3	Shutter Focus
SML	1.2	Space Microstructures Laboratory, at MIT
SPIE		Society of Photooptical Instrumentation Engineers
SSD	4.2	Solid State Detector, X-GEF
SSD	5.1.5	Solid State Detector, XRCF
TOGA	5	TMA Objective Grating Assembly
TMA	5	Technology Mirror Article
X-GEF	4.2	X-Ray Grating Evaluation Facility at MIT
XMM		X-Ray Multimirror Mission
XRCF	5	X-Ray Calibration Facility
XSPEC	7.8	X-Ray Spectral Fitting Package
XSS	5.1.1	X-Ray Source System

Mathematical Symbols

Symbol	Equation	Description
β	1.1	diffraction angle
m	1.1	diffraction order
λ	1.1	X-ray wavelength
p	1.1	grating period
HETGS response$(E, \ldots)$	1.2	
E	1.2	X-ray energy
$SEA(E, m, \ldots)$	1.2	system effective area
$PSF(E, m, \ldots)$	1.2	2-d normalized point spread function
s	1.3	shell (1,3,4,6) of HRMA or grating
$A_s(E, \ldots)$	1.3	HRMA effective area
$G_s(E, m)$	1.3	grating shell average efficiency
$QE(E, \ldots)$	1.3	detector quantum efficiency
ν_s	1.4	average grating vignetting on shell s
N_s	1.4	number of facets in shell s
f	1.4	grating facet identifier
$g_f(E, m)$	1.4	grating facet average efficiency
$G_{\mathrm{config}}(E, m)$	1.5	grating effective efficiency for config
config	1.5	config = set of shells: HEG, MEG, HETG
$\rho(y, z)$	1.6	2-D PSF, normalized distribution
y, z	1.6	detector coordinates
$l(y'),\ l(E)$	1.7	1-D LRF, normalized distribution
y', z'	1.7	grating dispersion coordinates
$R(E, m)$	1.8	resolving power
$dE,\ dy'$	1.8	FWHM of $l(E),\ l(y')$
$\Delta X_{\mathrm{Rowland}}$	2.1	detector offset to Rowland circle
X_{RS}	2.1	Rowland spacing
R_0	2.2	perpendicular distance of grating ring
σ_H	2.5	effective HRMA rms blur
dx	2.8	detector defocus
γ	2.11	grating rms roll variation
a	2.12	aspect blur rms diameter
F	2.12	HRMA focal length
R_{dither}	2.13	dither rate
t_D	2.13	detector quantization time
σ_D	2.14	detector rms blur

(to be continued...)

Bibliography

[1] S. Abdali, F.E. Christensen, H.W. Schnopper, T.H. Markert, D. Dewey, and C.S. Nelson, "High Resolution X-Ray Studies of an AXAF High Energy Transmission Grating", *Multilayer and Grazing Incidence X-Ray/EUV Optics II*, Proc. SPIE, Vol. 2011, pp. 2–11, July 1993.

[2] E.H. Anderson, A.M. Levine, and M.L. Schattenburg, "Transmission X-ray Diffraction Grating Alignment using a Photoelastic Modulator", *Applied Optics*, Vol. **27**, pp. 3522-3525 (1988).

[3] Beuermann, K.P., Brauninger, H., and Trumper, J., *Applied Optics*, Vol. **17**, no. 15., 2304 (1978).

[4] R.L. Blake, J.C. Davis, D.E. Graessle, T.H. Burbine, and E.M. Gullikson, "Optical Constants and Scattering Factors from Reflectivity Measurements: 50 eV to 5 keV", *Journal of X-ray Science and Technology*, in press.

[5] M. Born and E. Wolf, *Principles of Optics, Sixth Ed.*, pp. 401-414., Pergamon, New York, 1980.

[6] A.C. Brinkman, J. J. van Rooijen, J.A.M. Bleeker, J.H. Dijkstra, J. Heise, P.A.J. de Korte, R. Mewe, and F. Paerels, "Low energy X-ray transmission grating spectrometer for AXAF", in *X-ray Instrumentation in Astronomy, Proc. SPIE*, vol. 597, pp. 232-240, 1985.

[7] A.C. Brinkman, *et al., Astro. Lett. and Communications*, Vol. 26, p. 73, 1987.

[8] A.C. Brinkman, C.J.Th. Gunsing, J.S. Kaastra, H. Bräuninger, G. Hartner, P. Predehl, J.J. Drake, J.Z. Juda, M. Juda, D. Dewey, K.A. Flanagan, and H.L. Marshall, "Preliminary Test Results on Spectral Resolution of the Low Energy Transmission Grating Spectrometer on board of AXAF", , *these proceedings*,(1997).

[9] Canizares, C.R., Schattenburg, M.L., and Smith, H.I., "The High Energy Transmission grating Spectrometer for AXAF", in *X-ray Instrumentation in Astronomy, Proc. SPIE*, Vol. **597**, 253–260 (1985).

[10] C.R. Canizares, *et al., Astro. Lett. and Communications*, Vol. 26, p. 87, 1987.

[11] C.R. Canizares, "High Resolution X-Ray Spectroscopy of Thermal Plasmas" in Imaging X-Ray Astronomy, M. Elvis (ed.), Cambridge University Press, 1990.

[12] D.Dewey, D.N. Humpheries, G.Y. McLean and D.A. Moschella, "Laboratory Calibration of X-ray Transmission Diffraction Gratings", *EUX, X-Ray, and Gamma-Ray Instrumentation for Astronomy V*, Proc. SPIE, Vol. **2280**, 257–271 (1994).

[13] D. Dewey, H.L. Marshall, K.A. Flanagan, C. Baluta, C.R. Canizares, D.S. Davis, J.E. Davis, T.T. Fang, D.P. Huenemoerder, J.H. Kastner, N.S. Schulz, M.W. Wise, J.J. Drake, J.Z. Juda, M. Juda, A.C. Brinkman, T. Gunsing, J. Kaastra, G. Hartner and P. Predehl, "Towards the Callibration of the HETG Effective Area", *these proceedings*, (1997).

[14] R.J. Edgar, E.Y. Tsiang, A. Tennant, S. Vitek, and D. Swartz, "Spectral Fitting in AXAF Calibration Detectors", *Grazing Incidence and Multilayer X-Ray Optical Systems, Proc. SPIE*, Vol. **3113**, (1997).

[15] I.N. Evans, E.M. Kellogg, W.C. McDermott, M.P. Ordway, J.M. Rosenberg, and B.J. Wargelin, "High Speed Imager AXAF Calibration Microchannel Plate Detector", *Grazing Incidence and Multilayer X-Ray Optical Systems, Proc. SPIE*, Vol. **3113**, (1997).

[16] K.F. Fischbach, A.M. Levine, M.L. Schattenburg, D. Dewey, R.L. Renshaw, J. Dalcanton, R. Newman, and W. Fissell, "Performance of High Spatial Frequency X-Ray Transmission Gratings", *X-Ray Instrumentation in Astronomy II*, Proc. SPIE, Vol. 982, pp. 273–282, July 1988.

[17] K.A. Flanagan, D. Dewey, L. Bordzol, "Calibration and Characterization of HETG grating elements at the MIT X-ray Grating Evaluation Facility", *SPIE Proceedings* **2518**, 438–456 (1995).

[18] K.A. Flanagan, T.T. Fang, C. Baluta, J.E. Davis, D. Dewey, T.H. Markert, D.E. Graessle, J. Drake, J.E. Fitch, J.Z. Juda, J. Woo, S. Kraft, P. Bulicke, R. Fliegauf, F. Scholze, and G. Ulm, "Modeling the Diffraction Efficiencies of the AXAF High Energy Transmission Gratings: II", *EUX, X-Ray, and Gamma-Ray Instrumentation for Astronomy VII*, Proc. SPIE, Vol. **2808**, 650–676 (1996).

[19] G.W. Fraser, X-ray detectors in astronomy, Cambridge University Press, Cambridge, 1989.

[20] G.P. Garmire, *et al.*, "The AXAF CCD Imaging Spectrometer", in *X-ray Instrumentation in Astronomy, Proc. SPIE*, vol. 597, pp. 261-266, 1985.

[21] P. Gorenstein and M. Zombeck, *High Resolution X-ray Spectroscopy of Cosmic Plasmas*, Cambridge University Press, Cambridge, 1990.

[22] D. Graessle, A.M. Clark, J.J. Fitch, B. Harris, D.A. Schwartz, R.L. Blake, "Reflectance calibrations of AXAF Witness Mirrors Using Synchrtron Radiation, 2-12 keV", *SPIE Proceedings* **2805**, 18 (1996)

[23] B.L. Henke, E.M. Gullikson, and J.C. Davis, "X-ray Interactions: Photoabsorption, Scattering, Transmission, and Reflection at E = 50–30,000 eV, A = 1–92", *Atomic Data and Nuclear Data Tables*, Vol. 54, No. 2, July 1993.

[24] Kameritsch, P., "Calibration of Transmission Diffraction Gratings for the AXAF X-ray Satellite", thesis at the Ludwig Maximilians University, Munich, 1995.

[25] M. Keller, K. Shumate, Software Specification and Design : a Disciplined Approach for Real-Time Systems, John Wiley & Sons, Inc., New York, 1992.

[26] E. Kellogg, "Kα Line-to-continuum ratio for electron impact x-ray sources", internal memo to AXAF Calibration Task Team, October 5, 1992.

[27] E.M. Kellogg *et al.*, "Absolute calibration of the AXAF telescope effective area", *Grazing Incidence and Multilayer X-Ray Optical Systems, Proc. SPIE*, Vol. **3113**, (1997).

[28] C.J. Borkowski and M. Kopp, "Design and properties of position-sensitive proportional counters using resistance-capacitance position encoding", Rev. Sci. Instrum., Vol. 46, No. 8, August 1975.

[29] T.H. Markert, "Dispersive Spectroscopy on AXAF", in *High-Resolution X-ray Spectroscopy of Cosmic Plasmas, IAU Colloquium No. 115*, P. Gorenstein and M. Zombeck, eds., pp. 339-344, Cambridge University Press, Cambridge, 1990.

[30] T.H. Markert, C.R. Canizares, D. Dewey, M. McGuirk, C. Pak, and M.L. Schattenburg, "The High Energy Transmission Grating Spectrometer for AXAF", *EUX, X-Ray, and Gamma-Ray Instrumentation for Astronomy V*, Proc. SPIE, Vol. **2280**, 168–180 (1994).

[31] T.H. Markert, D. Dewey, J.E. Davis, K.A. Flanagan, D.E. Graessle, J.M. Bauer, C.S. Nelson, "Modeling the Diffraction Efficiencies of the AXAF High Energy Transmission Gratings", *SPIE Proceedings* **2518**, 424–437 (1995).

[32] H.L. Marshall, D. Dewey, K.A. Flanagan, C. Baluta, C.R. Canizares, D.S. Davis, J.E. Davis, T.T. Fang, D.P. Huenemoerder, J.H. Kastner, H.L. Marshall, N.S. Schulz, M.W. Wise, J.J. Drake, J.Z. Juda, M. Juda, A.C. Brinkman, C.J.Th. Gunsing, and J.S. Kaastra, G. Hartner and P. Predehl, "Towards the Calibration of the HETG LRF", *Grazing Incidence and Multilayer X-Ray Optical Systems, Proc. SPIE*, Vol. **3113**, (1997).

[33] S.S. Murray and J.H. Chappell, "The Advanced X-ray Astrophysics Facility High Resolution Camera", in *X-ray Instrumentation in Astronomy, Proc. SPIE*, vol. 597, pp. 274-281, 1985.

[34] S.S. Murray, *et al.*, *Astro. Lett. and Communications*, Vol. 26, p. 113, 1987.

[35] C.S. Nelson, *Synchrotron Studies of an X-ray Transmission Grating*, Bachelor's Thesis, MIT (1994)

[36] C.S. Nelson, T.H. Markert, Y.S. Song, M.L. Schattenburg, K.A. Flanagan, R.L. Blake, J. Bauer, E.M. Gullikson, "Efficiency Measurements and Modelling of AXAF High Energy Transmission Gratings", *EUX, X-Ray, and Gamma-Ray Instrumentation for Astronomy V*, Proc. SPIE, Vol. **2280**, 191–203 (1994).

[37] J.A. Nousek, G.P. Garmire, G.R. Ricker, S.A. Collins, and G.R. Reigler, *Astro. Lett. and Communications*, Vol. 26, p. 35, 1987.

[38] F.B.S. Paerels, J.V. Bixler, J.W. den Herder, C.J. Hailey, S.M. Kahn, and C.W. Mauche, "Modeling and Analysis of X-ray Emission Line Images Acquired with a Prototype Model of the XMM Reflection Grating Spectrometer", *X-Ray and Ultraviolet Spectroscopy and Polarimetry*, Proc. SPIE, Vol. **2283**, 107–118 (1994).

[39] C. Pak and M. McGuirk, "Computer Aided Design for the High Energy Transmission Grating (HETG) Spectrometer", paper 94-4566 presented at the *AIAA Space Programs and Technologies Conference*, Huntsville, AL (1994).

[40] P. Predehl, H. Bräuninger, A.C. Brinkman, D. Dewey, J.J. Drake, K.A. Flanagan, C.J.Th. Gunsing, G. Hartner, J.Z. Juda, M. Juda, J. Kaastra, H.L. Marshall, and D. Swartz, "X-Ray Calibration of the AXAF Low Energy Transmission Grating Spectrometer: Effective Area",*Grazing Incidence and Multilayer X-Ray Optical Systems, Proc. SPIE*, Vol. **3113**,(1997).

[41] M.L. Schattenburg, *et al.*, Optical Engineering,vol. 30, p. 1590, 1991.

[42] M.L. Schattenburg, R.J. Aucoin, R.C. Fleming, I. Plotnik, J. Porter, and H.I. Smith, "Fabrication of High Energy X-ray Transmission Gratings for AXAF", *EUX, X-Ray, and Gamma-Ray Instrumentation for Astronomy V*, Proc. SPIE, Vol. **2280**, 181–190 (1994).

[43] H.W. Schnopper, *et al.*, "Diffraction Grating Transmission Efficiencies for XUV and Soft X-rays", *Appl. Optics*, Vol. 16, p. 1088, 1977.

[44] F. Scholze, M. Krumrey, P. Müller, and D. Fuchs, "(PTB monochromator purity)", *Rev. Sci. Instrum.* **65**, 3229 (1994)

[45] G. Ulm, B. Wende, "(PTB Synchrotron)", *Rev. Sci. Instrum.* **66**, 2244-2247 (1995).

[46] B.J. Wargelin, E.M. Kellogg, W.C. McDermott, I.N. Evans, and S.A. Vitek, "AXAF Calibration: The HXDS Flow Proportional Counters", *Grazing Incidence and Multilayer X-Ray Optical Systems, Proc. SPIE*, Vol. **3113**, (1997).